

Fakultät für Physik und Astronomie

Ruprecht-Karls-Universität Heidelberg

Masterarbeit

Im Studiengang Physik

vorgelegt von

Ander Artola

geboren in Alicante, Spanien

2024

# **Signature of warm dark matter in the cosmological density fields extracted using Machine Learning**

Die Masterarbeit wurde von Ander Artola

ausgeführt am

Institut für Theoretische Physik

unter der Betreuung von

Dr. Sarah Bosman

Ich versichere, dass ich diese Master-Arbeit selbstständig verfasst und nur die angegebenen Quellen und Hilfsmittel verwendet habe.

Heidelberg, 20.09.2024

---

## Zusammenfassung

Die Natur der Dunklen Materie bleibt eines der faszinierendsten Rätsel der Physik. Während das Standardmodell der Kosmologie kalte Dunkle Materie (CDM) favorisiert, haben potenzielle Diskrepanzen auf kleinen Skalen das Interesse an alternativen Kandidaten wie Warmer Dunkler Materie (WDM) geweckt. Diese Arbeit stellt einen neuartigen Ansatz vor, um die Massen von WDM-Teilchen mithilfe des Lyman- $\alpha$ -Walds, einem wichtigen Instrument zur Untersuchung des intergalaktischen Mediums (IGM), das in den Spektren von Quasaren beobachtet wird, einzuschränken. Unter Verwendung hochauflösender kosmologischer Simulationen aus der Sherwood-Reihe simulieren wir den Lyman- $\alpha$ -Wald für verschiedene WDM-Szenarien. Wir stellen ein Deep-Learning-Framework vor, das neutrale Wasserstoffdichtefeld direkt aus dem Lyman- $\alpha$ -Fluss rekonstruiert und die komplexen Effekte von WDM auf das IGM erfasst. Diese rekonstruierten Dichtefelder bilden die Grundlage für ein Inferenzmodell, das es uns ermöglicht, die Massen von WDM-Teilchen auf eine bisher unerforschte Weise einzuschränken. Wir testen dieses Modell umfassend an simulierten Daten und wenden es anschließend auf reale Beobachtungen vom UltraViolet-Visual Echelle Spectrograph am Very Large Telescope und dem Gemini High-resolution Optical SpecTrograph am Gemini-Süd-Teleskop an. Unsere Ergebnisse reproduzieren die modernsten WDM-Beschränkungen, während sie deutlich weniger Beobachtungsdaten erfordern, was die Wirksamkeit des maschinellen Lernens in der modernen kosmologischen Forschung zeigt.

## Abstract

The nature of dark matter remains one of the most compelling mysteries in physics. While the standard cosmological model favours the Cold Dark Matter (CDM) paradigm, potential discrepancies at small scales have sparked interest in alternative candidates like Warm Dark Matter (WDM). This thesis presents a novel approach to constrain WDM particle masses using the Lyman- $\alpha$  forest, an important probe of the intergalactic medium (IGM) observed in the spectra of quasars. Leveraging high-resolution cosmological simulations from the Sherwood suite, we explore the effect of different WDM models on the Lyman- $\alpha$  forest. We introduce a deep-learning framework that reconstructs the neutral hydrogen density field directly from the Lyman- $\alpha$  flux, capturing the intricate effects of WDM on the IGM. These recovered density fields serve as the foundation for an inference pipeline, enabling us to constrain WDM particle masses in a previously

---

unexplored manner. We extensively test this pipeline on simulated data, then apply it to real observations from the UltraViolet-Visual Echelle Spectrograph at the Very Large Telescope and the Gemini High-resolution Optical SpecTrograph at the Gemini South telescope. Our findings are able to reproduce state-of-the-art WDM constraints while requiring significantly less observational data, demonstrating the efficacy of machine learning in modern cosmological research.

# Contents

<b>1</b>	<b>Introduction</b>	<b>1</b>
1.1	Cosmological preliminaries . . . . .	1
1.2	The intergalactic medium . . . . .	3
1.3	Dark matter . . . . .	8
1.4	Structure of this work . . . . .	12
<b>2</b>	<b>Simulating the Lyman-alpha forest</b>	<b>14</b>
2.1	The Sherwood simulation suite . . . . .	14
2.2	Obtaining mock Lyman-alpha skewers from cosmological simulations . .	18
2.3	Peculiar velocities and optical depth-weighted quantities . . . . .	21
2.4	Statistical analysis of the effect of dark matter in the flux and density fields	23
<b>3</b>	<b>Deep Learning the Lyman-alpha forest</b>	<b>28</b>
3.1	Introduction and motivation for the use of Deep Learning . . . . .	28
3.2	Fundamentals of (Bayesian) Neural Networks . . . . .	36
3.2.1	Dataset generation, data augmentation and overfitting . . . . .	37
3.2.2	Deep learning architecture . . . . .	40
3.2.3	Prediction uncertainty and Bayesian models . . . . .	42
3.2.4	Hyperparameter selection . . . . .	44
3.2.5	Loss function and training . . . . .	46
3.3	Workflow implementation: Recovering IGM conditions from the Lyman-alpha forest . . . . .	49
3.4	Recovered field statistics and uncertainties . . . . .	54
3.4.1	Noisy regions and masking . . . . .	56
3.4.2	Uncertainty in the recovered statistics . . . . .	57
3.5	Model interpretability and limitations . . . . .	63
3.5.1	Saliency analysis . . . . .	63
3.5.2	Covariate shift . . . . .	64
3.5.3	Extreme covariate shift and malicious data . . . . .	66

3.5.4	Model pruning . . . . .	66
<b>4</b>	<b>Constraining warm dark matter at the density level</b>	<b>69</b>
4.1	Inference pipeline: from Lyman-alpha skewers to WDM constraints . . . . .	69
4.2	Inference testing on simulated Sherwood spectra under realistic observational conditions . . . . .	71
4.2.1	Untrained DM models . . . . .	71
4.2.2	Realistic observational conditions . . . . .	73
4.3	Inference on alternative hydrodynamical codes . . . . .	75
4.3.1	The Nyx code . . . . .	76
4.3.2	Inference test on Nyx Lyman-alpha skewers . . . . .	79
4.4	WDM constraints from SQUAD DR1 observational data . . . . .	81
4.5	WDM constraints from GHOST observed spectrum . . . . .	83
4.6	Comparison of the inference pipeline against Information Maximising Neural Networks . . . . .	88
4.6.1	Information Maximising Neural Networks . . . . .	88
4.6.2	IMNN training and non-linear summaries . . . . .	89
4.6.3	Summarising a Gaussian signal . . . . .	90
4.6.4	IMNN inference results on WDM masses . . . . .	93
<b>5</b>	<b>Conclusions</b>	<b>96</b>
	<b>Bibliography</b>	<b>98</b>

# 1 Introduction

## 1.1 Cosmological preliminaries

The currently accepted cosmological model describes space-time as a 4-dimensional Lorentzian manifold equipped with the Robertson-Walker metric [1]

$$ds^2 = c^2 dt^2 - a(t)^2 \left( \frac{dr^2}{1 - kr^2} + r^2 d\Omega^2 \right), \quad (1.1)$$

with  $c$  the speed of light in vacuum,  $a$  the scale factor,  $k$  a curvature parameter and  $d\Omega$  the angular volume element in spherical coordinates. The scale factor is taken to be unity at present. At time  $t$ , a physical (proper) distance  $l_{\text{phy}}$  is then related to a comoving distance  $l_{\text{cov}}$  by

$$l_{\text{phy}} = a(t)l_{\text{cov}}. \quad (1.2)$$

The physical distance at time  $t$  between an observer at  $r = 0$  and a point at  $r$  is then

$$l_{\text{phy}} = a(t) \int_0^r \frac{dr}{\sqrt{1 - kr^2}} = a(t)\chi(r). \quad (1.3)$$

The Robertson-Walker metric implies that for a radial luminous signal emitted at time  $t_e$  and received at time  $t_0$ , we have

$$ds^2 = 0 \implies \frac{dt_0}{a(t_0)} = \frac{dt_e}{a(t_e)}. \quad (1.4)$$

As a consequence, the received frequency is redshifted according to

$$1 + z = \frac{\lambda_0}{\lambda_e} = \frac{\nu_e}{\nu_0} = \frac{a(t_0)}{a(t_e)}, \quad (1.5)$$

where  $z$  is the redshift.

The time-dependence of physical distances in Equation 1.2 implies that an object whose comoving distance  $\chi$  to an observer is constant recedes by following the Hubble

flow according to

$$v(t) = \dot{a}(t)\chi = \frac{\dot{a}}{a}a\chi = H(t)l_{\text{phy}}, \quad (1.6)$$

where  $H(t)$  is known as the Hubble factor. Equation 1.6 is known as Hubble's law. At present time,  $H(t_0) = H_0$  is referred to as Hubble's constant. For historical reasons, it is common to work with the reduced Hubble constant  $h = H_0[\text{km/s/Mpc}]/100$ . Note that, according to Equation 1.3, and using the Robertson-Walker metric for a radial light signal, we obtain

$$d\chi = \frac{cdt}{a} \implies \chi = \int_a^1 \frac{da}{a\dot{a}} = \int_0^z \frac{cdz}{H(z)}. \quad (1.7)$$

As a consequence, the proper line element satisfies

$$d\chi = \frac{cdz}{H(z)} = \frac{dl}{a(t)} \implies \frac{dl}{dz} = \frac{c}{(1+z)H(z)}, \quad (1.8)$$

which will be useful when integrating quantities along a line of sight. When working with such sightlines in spectroscopy, it is often advantageous to work with velocity units instead of redshifts (or proper distances). Differentiating Equation 1.6 and considering a slow varying Hubble factor around a mean redshift  $\bar{z}$ , we obtain the following useful expression:

$$dv = H(\bar{z})dl = H(\bar{z})\frac{cdz}{(1+\bar{z})H(\bar{z})} = \frac{cdz}{1+\bar{z}}. \quad (1.9)$$

The evolution of the scale factor (and hence of the redshift) with time is completely determined by the energy content of the universe through Einstein's field equation, which is known as Friedmann's equation in this context

$$H^2 = H_0^2 (\Omega_M(1+z)^3 + \Omega_R(1+z)^3 + \Omega_\Lambda + \Omega_K(1+z)^2) = H_0^2 E(z)^2, \quad (1.10)$$

where the density parameters  $\Omega$  are related to the physical densities of the components according to

$$\begin{aligned} \Omega_M &= \frac{8\pi G}{3H_0^2} \rho_{M0} \\ \Omega_R &= \frac{8\pi G}{3H_0^2} \rho_{R0} \\ \Omega_\Lambda &= \frac{8\pi G}{3H_0^2} \rho_\Lambda \\ \Omega_K &= -\frac{k}{H_0^2} \end{aligned} \quad (1.11)$$

In Equation 1.11,  $\rho_M$  denotes the matter density of the universe,  $\rho_R$  the radiation density, and  $\rho_\Lambda$  the dark energy component. In the following, the values used for the cosmological parameters are  $\Omega_M = 0.308$ ,  $\Omega_\Lambda = 0.692$ ,  $h = 0.678$ ,  $\Omega_b = 0.0482$ ,  $\sigma_8 = 0.829$ ,  $n = 0.961$  and  $\Omega_K \approx 0$ , as obtained from CMB measurements by the Planck Collaboration [2]. As we will discuss in Section 1.3, the current cosmological model  $\Lambda$ CDM includes a cold dark matter component that dominates over baryonic matter. With the previous cosmological parameters, the matter and cosmological constant are equal when

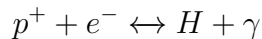
$$\Omega_M(1+z)^3 = \Omega_\Lambda \implies z \approx 0.3. \quad (1.12)$$

In consequence, at the redshift of interest for this work,  $z \sim 4 - 5$ , the universe is well-described as a matter-dominated universe.

## 1.2 The intergalactic medium

As the name suggests, the intergalactic medium (IGM) is the low-density part of the Universe's content that permeates the space between halos and galaxies [3]. The history of the IGM is closely related to the formation and evolution of galaxies, with multiple feedback mechanisms. For instance, IGM gas can aggregate and provide material to be captured by halos, while the radiation emitted by stars and quasars affects the state of the IGM. At sufficiently early times, all baryons were by definition part of the IGM, so the IGM represents the primordial material for galaxy formation. Since the IGM has very low densities, its properties are typically probed by the absorption of light coming from background sources, such as quasars. To give a rough overview of the properties of the IGM, its typical temperature is  $\sim 10^4$  K, with peculiar velocities of  $\sim 10 - 100$  km/s and neutral hydrogen column densities of  $\sim 10^{12-17}$  cm $^{-2}$ .

One of the most relevant processes in the IGM is ionisation. Consider the hydrogen recombination process:



The total ionisation process has two main contributions: collisional ionisation and photo-ionisation. Collisional ionisation tends to be non-dominant and is due to the collision of an energetic electron with a neutral hydrogen atom. Let  $\Gamma_c$  be the collisional rate, so that the number of collisional ionisation per unit volume per unit time is  $\Gamma_c n_e n_{HI}$ . Photo-ionization is the dominant process and arises from an energetic photon colliding with a neutral hydrogen atom. Let  $J$  be the flux of ionizing photons, then the number

of photo-ionizations per volume per time is  $\Gamma_i n_{HI}$  where

$$\Gamma_i = \int_{\nu_t}^{\infty} \frac{4\pi J(\nu)}{ch_P \nu} c \sigma(\nu) d\nu \quad (1.13)$$

and  $\nu_t$  is the threshold frequency for ionizing photons (so, the Rydberg energy). If  $\alpha$  is the recombination rate, the number of recombinations per time per volume is  $\alpha n_{p^+} n_{e^-}$ . The equilibrium equation is the

$$\alpha n_{p^+} n_{e^-} = \Gamma_i n_{HI} + \Gamma_c n_{e^-} n_{HI}. \quad (1.14)$$

And so, the neutral hydrogen number density at equilibrium must be:

$$n_{HI} = \frac{\alpha n_{p^+} n_{e^-}}{\Gamma_c n_{e^-} + \Gamma_i}. \quad (1.15)$$

Note that here  $n_{p^+}$  is the density of free protons. If the gas is highly ionized we can take  $n_{e^-} = n_{HI} + n_{p^+} \approx n_{p^+}$  and so, neglecting the collision part:

$$n_{HI} = \frac{\alpha n_{p^+}^2}{\Gamma_i}. \quad (1.16)$$

In a dynamic universe, the equilibrium holds provided that the reaction rates are sufficiently large compared to the expansion time-scale  $H^{-1}$ . Since photo-ionization dominates, this can be expressed as

$$H^{-1}(z) \ll \Gamma_i, \quad (1.17)$$

where  $\Gamma_i$  depends on the ionizing photon flux, and so depends on redshift.

Considering that the IGM is made out of fully ionized hydrogen and helium, we have that:

$$n_p = n_H + 2n_{He} \quad n_n = 2n_{He}. \quad (1.18)$$

The helium weight fraction is then defined as

$$Y = \frac{m_{He}}{m_{He} + m_H} \approx \frac{4n_{He}}{4n_{He} + n_H} = \frac{2n_n}{n_n + n_p} = \frac{2n_n/n_p}{1 + n_n/n_p} \approx 0.25. \quad (1.19)$$

The IGM also contains helium and a small fraction of metals, that contribute to its absorption properties.

We are generally interested in matter fluctuations of the IGM. Hence, we define the

following quantity of interest, called the *baryonic overdensity* field, as

$$\Delta = \frac{\rho}{\bar{\rho}}, \quad (1.20)$$

where  $\rho(\bar{\rho})$  is the (mean) baryonic density. Let us recover the hydrogen density  $n_H$  from the baryonic overdensity  $\Delta$ , the redshift  $z$  and the density parameter  $\Omega_b$ . First, suppose there is no overdensity so that  $\Delta = 1$  and the comoving density is homogeneous. Recall from the mean molecular weight section that

$$\mu_H = \frac{1}{1 - Y} = \frac{4}{3} = \frac{\rho_b}{m_p n_H} \quad (1.21)$$

and that

$$\rho_b = \frac{3H^2}{8\pi G} \Omega_b, \quad (1.22)$$

so that

$$n_H = \frac{9H^2\Omega_b}{32m_p\pi G}. \quad (1.23)$$

Now, in a matter-dominated universe (for the redshifts we are interested in), the Friedmann equation states  $H^2 = H_0^2(1 + z)^3$ . So, we obtain,

$$n_H = \frac{9}{32m_p\pi G} H_0^2 \Omega_b (1 + z)^3 \quad (1.24)$$

and substituting values,

$$n_H = 1.7 \cdot 10^{-7} (1 + z)^3 \text{ cm}^{-3}. \quad (1.25)$$

Now if, the hydrogen density is not homogeneous (that is,  $\Delta \neq 1$ ),  $n_H$  will be locally modulated by  $\Delta$ , so that

$$n_H = 1.7 \cdot 10^{-7} (1 + z)^3 \Delta \text{ cm}^{-3}. \quad (1.26)$$

Since cosmological simulations typically produce as output the baryonic overdensity  $\Delta$ , we can use Equation 1.26 to recover the corresponding hydrogen density.

The hydrogen Lyman- $\alpha$  absorption lines in the spectra of quasars allow us to probe the state of the IGM. In particular, the Lyman- $\alpha$  opacity can then be used to estimate the average neutral hydrogen fraction  $x_{\text{HI}}$ . The evolution of the observed Lyman- $\alpha$  optical depth indicates that the IGM is highly ionized at  $z \lesssim 5.5$ , [4], [5]. The two main sources of UV ionising photons are believed to be young galaxies and quasars.

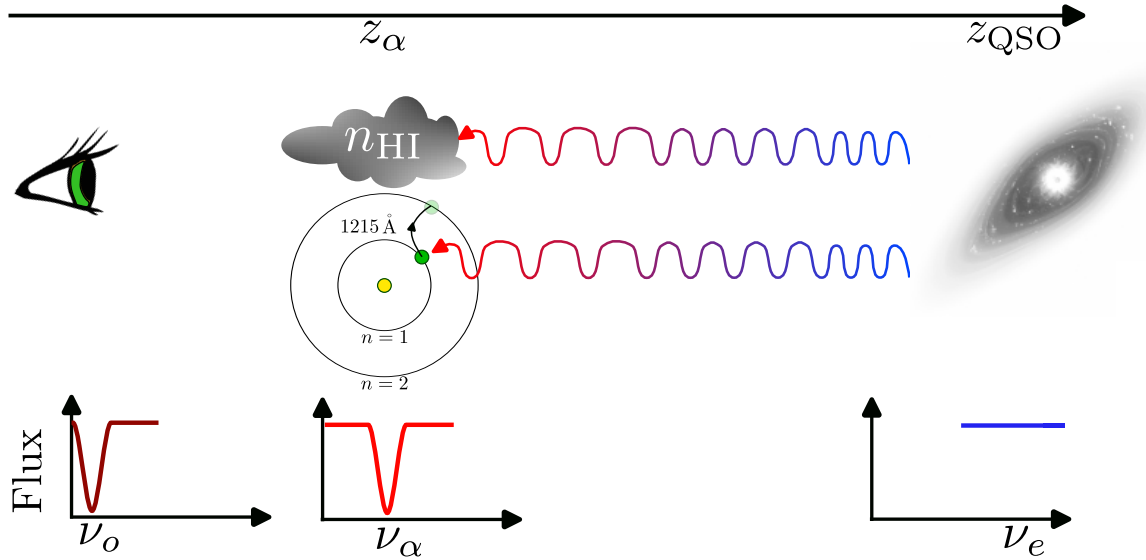


Figure 1.1: Illustration of the Lyman- $\alpha$  absorption by neutral hydrogen at  $z = z_\alpha$  in the line of sight of a QSO at  $z = z_{\text{QSO}}$ . In the observer's rest frame, the observed frequency is  $\nu_o$ . The associated frequency emitted by the QSO is  $\nu_e$ .

Let us now describe how an intergalactic cloud (with no peculiar velocity) along the line of sight of a quasar affects its spectrum, allowing for a powerful probing mechanism of the IGM gas properties. Consider the situation illustrated in Figure 1.1, where a QSO at redshift  $z_{\text{QSO}}$  emits photons, and consider the propagation of an emitted photon with rest-frame frequency  $\nu_e$ . Those photons are redshifted and are absorbed in  $z_\alpha$  by a neutral hydrogen absorber with local number density  $n(z_\alpha)$  producing an absorption feature in the flux at the rest-frame Lyman- $\alpha$  resonance  $\lambda_\alpha \approx 1215\text{\AA}$ . The unabsorbed photons are then redshifted and are detected by an observer at  $z = 0$  and a frequency  $\nu_o$ . The relationship between the frequencies mentioned above is then:

$$\nu_o = \frac{\nu_e}{1 + z_e} = \frac{\nu_\alpha}{1 + z_\alpha}. \quad (1.27)$$

We are interested in studying the effect of the Lyman- $\alpha$  absorbed at  $z_\alpha$ . The observed flux attenuation at the observed frequency  $\nu_0$  is then expressed as  $\exp(-\tau_\alpha)$ , with  $\tau_\alpha$  the Lyman- $\alpha$  opacity at the observed frequency, which depends on the absorber's density and the Lyman- $\alpha$  cross-section  $\sigma_\alpha(\nu)$ . Observe now that since the Lyman- $\alpha$  cross-section is strongly peaked at the resonance  $\nu_\alpha$ , but can have a non-zero width, a nearby neutral hydrogen cloud might absorb photons at a redshift different to  $z_\alpha$  that would have contributed to the observed flux at frequency  $\nu_o$ . With this consideration, we integrate over the line of sight to obtain the Lyman- $\alpha$  opacity at the observed frequency

$$\tau_\alpha(\nu_o) = \int_o^{z_{\text{QSO}}} n_{\text{HI}}(z) \sigma_\alpha[\nu_o(1+z)] dz. \quad (1.28)$$

If we now take  $\sigma_\alpha(\nu)$  to be a Dirac delta centered at the resonance  $\nu_\alpha$ , and we integrate Equation 1.28 by using Equation 1.8 we obtain

$$\tau_\alpha(\nu_o) \approx \frac{cn_{\text{HI}}(z_\alpha)\sigma_\alpha}{H_0\Omega_m^{1/2}(1+z)^{1/3}}, \quad (1.29)$$

where now  $\sigma_\alpha = 4.5 \times 10^{-18} \text{ cm}^2$  is to total Lyman- $\alpha$  cross-section. Equation 1.29 is known as the Gunn-Peterson approximation for the Lyman- $\alpha$  opacity of the IGM [6]. Equation 1.29 demonstrates that quasar spectra are a useful probe of the intergalactic neutral hydrogen density.

A more precise analysis of Equation 1.28 can be done if we do not approximate  $\sigma_\alpha$  as a Dirac delta. Instead, we can include the two main broadening effects in the absorption cross-section: the natural broadening and the thermal broadening. The natural broadening is a result of quantum processes and generates a Lorentzian profile, while the thermal one is due to the microscopic Doppler effect of thermal motion and generates a Gaussian profile. The resulting combination of both the Lorentzian and Gaussian profiles is known as a Voigt profile. It is a non-analytical function with a Gaussian-like shape but heavier tails:

$$V(x, y) = \frac{Y}{\pi} \int_{-\infty}^{\infty} \frac{e^{-t^2}}{(x-t)^2 + y^2} dt. \quad (1.30)$$

The Lyman- $\alpha$  absorption cross-section described by the Voigt profile is then

$$\sigma_\alpha(\nu) = \frac{cI_\alpha}{b\sqrt{\pi}} V\left(\frac{x(\nu - \nu_\alpha)}{b\nu_\alpha}, \alpha\right), \quad (1.31)$$

where  $b = \frac{\sqrt{2k_B T}}{m_p}$  is the Doppler parameter at temperature  $T$ ,  $\nu_\alpha \approx 2.47 \times 10^{15}$  Hz is the *Lyman -  $\alpha$*  frequency,  $I_\alpha \approx 4.45 \times 10^{-18} \text{ cm}^2$  is the total absorption cross-section [3] and  $\alpha$  is the recombination coefficient, which also depends on the temperature. The Lyman- $\alpha$  cross-section is then peaked at the resonant frequency, and broadened by the temperature and the recombination rate. Now, consider a sightline of gas absorbing Lyman- $\alpha$  photons. Peculiar bulk velocities  $v$  of the gas will add an additional Doppler

effect in the cross-section as

$$\sigma_\alpha(\nu) = \frac{cI_\alpha}{b\sqrt{\pi}} V \left( \frac{x(\nu - \nu_\alpha)}{b\nu_\alpha} + \frac{v}{b}, \alpha \right). \quad (1.32)$$

We can now integrate Equation 1.32 along the sightline to obtain the Lyman- $\alpha$  opacity  $\tau$  as

$$\tau = \int n(t) \sigma_\alpha(\nu_\alpha a(t_0)/a(t)) dt, \quad (1.33)$$

where  $n$  is the neutral hydrogen density and  $t_0$  the emisison time. Recalling that the comoving distance  $x$  is related to redshift and time as

$$dx = \frac{c}{H(z)} dz = c(1+z)dt, \quad (1.34)$$

we get that the Lyman- $\alpha$  optical depth  $\tau$  can be obtained from the neutral hydrogen gas properties along the sightline as follows:

$$\tau(z_0) = \frac{cI_\alpha}{\sqrt{\pi}} \int dx \frac{n_{\text{H}}[x, z(x)]}{b[x, z(x)][1+z(x)]} \times V \left\{ \frac{c[z(x) - z_0]}{b[x, z(x)](1+z_0)} + \frac{v[x, z(x)]}{b[x, z(x)]}, \alpha \right\} \quad (1.35)$$

where  $n_{\text{H}}$  is the neutral hydrogen density,  $b = \sqrt{\frac{2k_B T}{m_p}}$ ,  $v$  is the peculiar velocity along the sightline,  $m_p$  is the proton mass,  $k_B$  is Boltzmann's constant,  $\alpha$  is the recombination coefficient,  $c$  is the speed of light,  $I_\alpha$  is the total cross-section for Lyman- $\alpha$  absorption and  $V$  is the Voigt function [7]. Since the Lyman- $\alpha$  flux field

$$F = e^{-\tau}$$

depends on the properties of the absorbing gas, it contains information about the state of the IGM. The set of Lyman- $\alpha$  absorption features on the spectrum of a quasar is known as the Lyman- $\alpha$  forest. In Figure 1.2 we show the spectrum of the quasar 1422+23, taken with the Keck HIRES instrument, and featuring a Lyman- $\alpha$  forest.

### 1.3 Dark matter

Many aspects of the large-scale structure of the Universe can be understood by including a *cold dark matter* (CDM) component that represents  $\sim 26\%$  of the critical density [2]. In the standard cosmological model,  $\Lambda$ CDM, dark matter is an important ingredient for structure formation in the Early Universe. However, its precise nature remains an

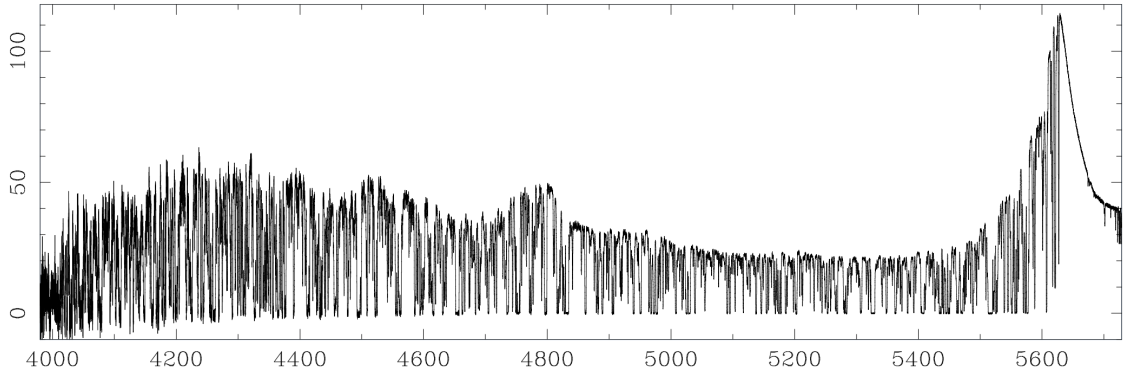


Figure 1.2: High resolution (FWHM  $\sim 6.6$  km/s) spectrum of the  $z = 3.62$  quasar 1422+23, taken with the Keck HIRES (signal-to-noise ratio  $\sim 150$  per resolution element, exposure time 25000 s). The horizontal axis is in units of observed wavelength in angstroms. Extracted from [8]

outstanding problem both in cosmology and particle physics. With more exotic DM candidates, such as primordial black holes, heavily constrained, it is likely that DM consists of some undiscovered elementary particle(s) produced early in the history of the universe [9]. There are multiple pieces of evidence supporting the CDM model, including the rotation curves of spiral galaxies and the kinematics of colliding clusters such as the Bullet cluster [10], [11].

According to the current paradigm [3], dark matter halos are the structures that host galaxies. They form through the gravitational collapse of non-linear perturbations in the primordial density field that serve as the first seeds for the formation of structures. Dark matter halos then grow by accreting material from their surrounding (such as the IGM). The properties of dark matter have then a direct influence on the properties of galaxies (formation, clustering, merging, etc.) and in the general distribution of matter in the Universe.

The evolution of the primordial fluctuations is not only determined by the gravitational clumping of matter but also by the effect of random particle motions, which leads to a damping of the density peaks and perturbations. The scale at which this happens is set by the free-streaming length defined as the comoving distance travelled by a particle before a time  $t$ :

$$\lambda_{\text{FS}} = \int_0^t \frac{v(t')}{a(t')} dt'. \quad (1.36)$$

$\Lambda$ CDM models dark matter as pressureless and only interacting through gravity. Moreover, CDM decouples from the primordial plasma when it is already non-relativistic. As

a consequence, CDM has no significant amount of free-streaming, and (thermal)pressure does not hinder its clustering, which enables the formation of large halos that can be as massive as  $10^{15} M_{\odot}$ .

On large scales, the predictions of  $\Lambda$ CDM have been amply tested and are in good agreement with observations [12], [13], [14]. In contrast, on scales smaller than  $\sim 10$  kpc, potential tensions between CDM predictions and observations might exist, including the “core-cusp” problem related to the DM density profile in halos, or the “too big to fail” problem linked to the number density of high-luminosity satellites in sub-halos [15], [16], [17]. Even if the inclusion of complex baryonic feedback processes can alleviate the aforementioned potential discrepancies, alternative models to CDM are worth exploring [18].

As a consequence of these possible tensions, there have been a multitude of DM candidates to CDM. Such variations have included self-interactions [19] and fuzzy DM which leads to wave-like features in the density fields [20]. Most alternative models retain the success of CDM on large scales while reproducing the desired features on smaller scales. Simulating how variations of CDM affect the evolution of structures in the Universe is highly non-trivial. Perhaps the simplest models that are viable to explore are warm(hot) dark matter WDM (HDM). Such candidates are usually classified according to their free-streaming scales. While for CDM particles  $\lambda_{\text{FS}}$  is negligible at the scales of cosmological structure formation, for HDM models, such as light neutrinos,  $\lambda_{\text{FS}}$  smooths out gravitational clustering even at galaxy cluster scales, leading to tight constraints on such models [21]. In between HDM and CDM, WDM offers an intermediate range of free-streaming scales that could potentially be compatible with the observed evolution of the Universe. In this work, we focus on thermal relic WDM models, which include potential particles such as gravitinos or sterile neutrinos that were coupled to the original plasma in the Early Universe [22]. For such models, WDM is a particle of mass in the scale of the KeV. A WDM particle with a mass of 1 KeV would have a free-streaming scale of  $\Lambda_{\text{FS}} \sim 0.3$  Mpc. In general, more massive particles are associated with smaller velocities and hence smaller  $\lambda_{\text{FS}}$ . The nature of WDM suppresses the total matter power spectrum on scales smaller than their free-streaming. That is, the less massive a WDM model is, the more the power spectrum is suppressed at small scales, and the more the density features of the density field are smoothed out. To illustrate this process, consider Figure 1.3, which shows a simulated density field as a function of redshift, and the WDM model mass. On the horizontal axis, the time evolution shows how gravity collapses dense regions into structures. On the vertical axis, the WDM free-streaming

length suppresses small-scale clustering.

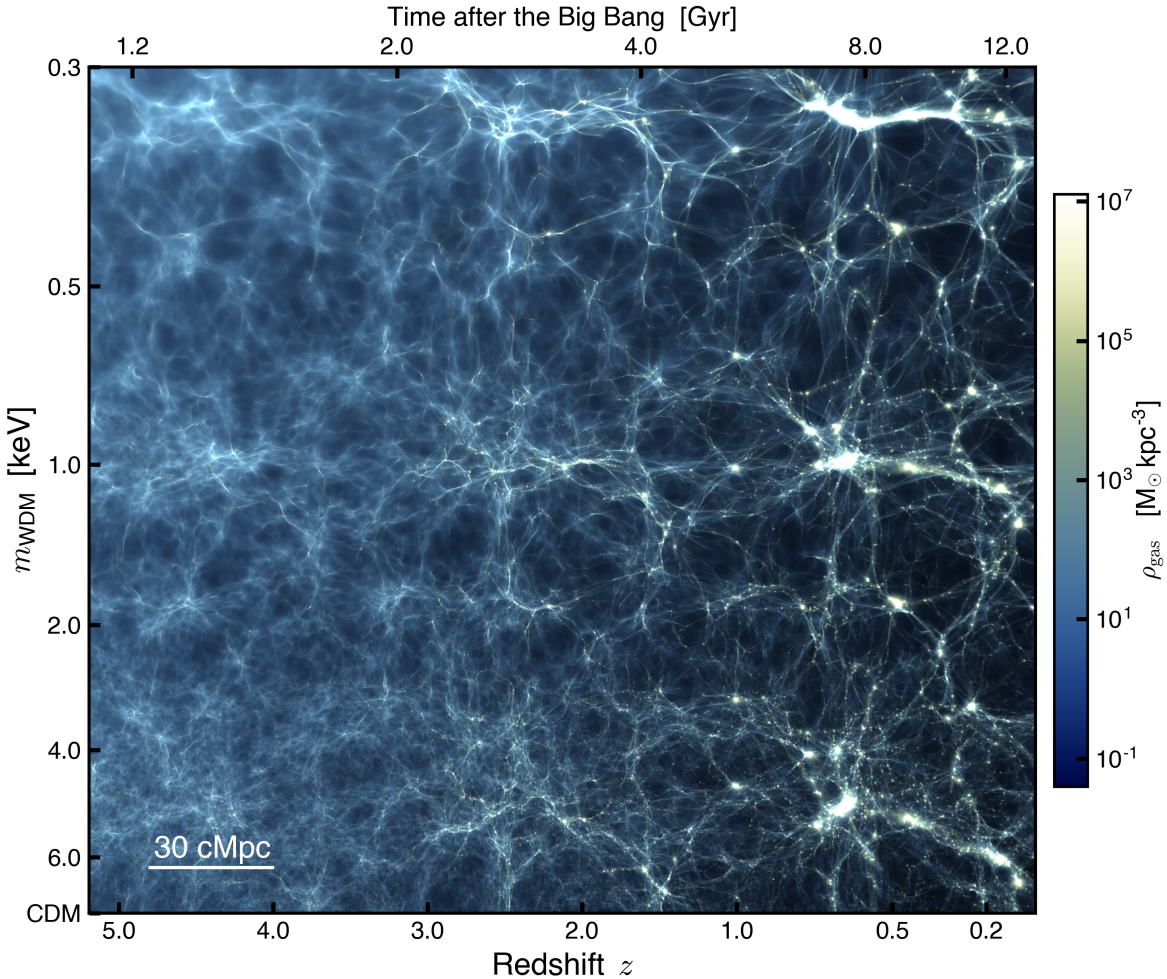


Figure 1.3: Baryonic density plot of the IGM as a function of redshift, and the WDM model mass. On the horizontal axis, the time evolution shows how gravity collapses dense regions into structures. On the vertical axis, the WDM free-streaming length suppresses small-scale clustering. Extracted from [23].

Constraining WDM in the cosmological context involves understanding and determining which WDM model masses are compatible with the universe we observe. Since the effect of WDM on structure formation is too complex, this process typically involves comparing simulations with observations: cosmological simulations are run for multiple WDM models, and the resulting properties are statistically compared to observations to rule out a certain range of masses. In Section 2 we discuss how such simulations work and how WDM models are included in them.

Observations that have been used to constrain DM models include gravitational lens-

ing [24] or the study of dwarf galaxies [25]. In this work, we focus on the Lyman- $\alpha$  forest that was introduced in Section 1.2. As we have discussed, the properties of the Lyman- $\alpha$  forest depend on the properties of the IGM, and in particular on its matter distribution, which is directly linked with the WDM particle mass. Many efforts have been made to constrain WDM by comparing the Lyman- $\alpha$  forest generated by WDM models to the observed one in quasar spectra [26], [23], [22].

## 1.4 Structure of this work

Building on previous efforts in the literature (most notably [27]), in this work we explore the possibility of reconstructing the neutral hydrogen density field directly from the Lyman- $\alpha$  forest and whether such information can be used to constrain WDM. This reconstruction step involves careful analysis and represents a challenge at the frontier of the current efforts by the community. While the current state-of-the-art techniques extract information from the Lyman- $\alpha$  forest by using summary statistics, recovering the non-observable physical fields of relevance would allow for the extraction of all the richness of information present in the forest. In particular, such techniques would allow for the mapping of the neutral hydrogen distribution in the Universe at the scales and redshifts where the forest is observable.

We begin in Section 2 by exploring how WDM models affect the Lyman- $\alpha$  forest and the underlying neutral hydrogen field. For that purpose, we introduce a set of cosmological simulations that will be at the core of this work, the **SHERWOOD** simulation suite. We discuss the main aspects of such simulated data, including the cosmological code used in them. We conclude Section 2 with a statistical analysis of the Lyman- $\alpha$  forest. Section 3 is devoted to introducing the deep learning machinery used to reconstruct the neutral hydrogen density field from the Lyman- $\alpha$  forest flux. We begin by motivating the use of machine learning techniques and describing the basic concepts and implementations related to such tools. Next, we discuss the motivation, architecture and implementation of the Bayesian neural network used in this regression task. We describe how we train the model using simulated data, evaluate its performance and robustness, and discuss some relevant questions about its internal dynamics. Armed with a machine learning pipeline that can reconstruct the neutral hydrogen density field from observed Lyman- $\alpha$  skewers, we are set to use this information in Section 4 to constrain WDM. We discuss and implement a statistical pipeline to convert the recovered neutral hydrogen density field into WDM constraints. We extensively test

this pipeline first on simulated data, from which we know the DM model used. Then, we turn our attention to real observational data and apply our technique to a set of quasar sightlines obtained from state-of-the-art spectrographs. We compare our results with the most up-to-date constraints in the literature, both in terms of tightness and efficiency in data usage.

## 2 Simulating the Lyman-alpha forest

In Section 1 we discussed how the Lyman- $\alpha$  forest is sensitive to multiple physical parameters, such as the low-gas temperatures, velocities, densities, etc. Each possible state of the IGM’s ionised low-density gas can lead to different absorption spectra and different forms of the forest. Hydrogen reionisation finishes at  $z < 5.3$  [28]. Hence, at low redshift, there is no neutral hydrogen to produce absorption features, and we have complete transmission of the Lyman- $\alpha$  flux without features, which means we cannot extract information about the IGM through this process. On the other end, at high redshifts,  $z > 6$ , the hydrogen is not sufficiently ionised and total absorption of the quasar continuum by neutral hydrogen generates long Gunn-Peterson troughs. The Lyman- $\alpha$  forest at  $2 < z < 5$  is then a powerful probe of the state of the IGM at scales and redshifts not accessible by any other observable [29]. As a consequence, simulations of the Lyman- $\alpha$  forest are typically carried out at said redshift range.

### 2.1 The Sherwood simulation suite

Lyman- $\alpha$  simulations are typically based on cosmological simulation codes. In this work, we will mainly focus on the **SHERWOOD** simulation suite<sup>1</sup> [30], which is based on the **GADGET-2** code developed by Volker Springel [31]. **GADGET-2** uses the Lagrangian formulation of fluid dynamics to trace the evolution of fluid particles.

**GADGET-2** traces non-interacting dark matter (as described by the collisionless Boltzmann equation) by sampling the phase space with a finite number of particles and solving their dynamics. The dynamics of such particles are subject to the Hamiltonian

$$H = \sum_i \frac{\mathbf{p}_i^2}{2m_i a(t)^2} + \frac{1}{2} \sum_{ij} \frac{m_i m_j \varphi(\mathbf{x}_i - \mathbf{x}_j)}{a(t)}, \quad (2.1)$$

---

<sup>1</sup><https://www.nottingham.ac.uk/astronomy/sherwood/>

where  $\mathbf{x}$  are the comoving positions,  $a$  the scale factor,  $\mathbf{p}$  the canonical momenta and  $m$  the particle masses.

On the other hand, the gas particles are traced using Smoothed Particle Hydrodynamics (SPH). SPH describes a fluid using a finite set of tracer particles that sample the local state of the fluid. Then, smooth quantities are obtained by using a smoothing kernel to interpolate between the tracer's properties. The equation of motion for the SPH particles is then

$$\frac{d\mathbf{v}_i}{dt} = - \sum_{j=1}^N m_j \left[ f_i \frac{P_i}{\rho_i^2} \nabla_i W_{ij}(h_i) + f_j \frac{P_j}{\rho_j^2} \nabla_i W_{ij}(h_j) \right], \quad (2.2)$$

with

$$f_i = \left[ 1 + \frac{h_i}{3\rho_i} \frac{\partial \rho_i}{\partial h_i} \right]^{-1}. \quad (2.3)$$

Here,  $W$  is the smoothing kernel,  $h_i$  are smoothing length parameters,  $P_i$  are the pressures associated with the particles and  $\rho_i$  are their densities. For more details see the original paper [31].

Gravity is the driving force for structure formation in the Universe, but its long-range nature makes it challenging to implement efficiently. GADGET-2 implements a gravitational algorithm that ensures sufficient spatial adaptability by using a hierarchical multipole expansion. By using a tree-like approach, we can compute the force applied to a particle in complexity  $\mathcal{O}(\log(N))$  instead of  $\mathcal{O}(N)$ , where  $N$  is the number of particles. The algorithm works by subdividing the space into octants, such that each leaf contains a single particle. The net force on a particle is then calculated by traversing the octree and replacing a distant cell with a single body, thus reducing the number of needed terms. This process is also called the *Barnes-Hut* algorithm, see Figure 2.1 for an illustration of it.

The dynamics of the system are then governed by the interaction potential

$$\nabla^2 \Phi(x) = 4\pi G(\rho - \bar{\rho}). \quad (2.4)$$

The SHERWOOD suite implements the effect of WDM by suppressing the initial power spectrum as described in [22]. In this approach, the effects of the warm dark matter free-streaming length on the matter distribution are described by a transfer function  $T(k)$

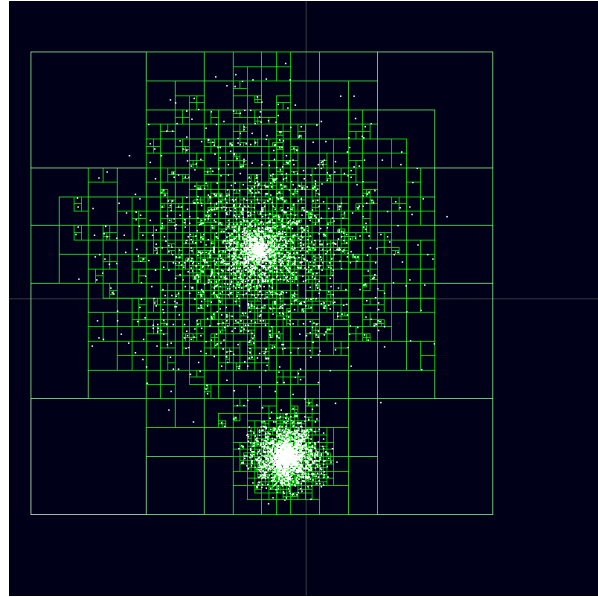


Figure 2.1: An octree generated using the Barnes-Hut algorithm for a set of particles (in white) in a 2D space.

$$T(k)^2 = \frac{P(k)_{\Lambda WDM}}{P(k)_{\Lambda CDM}}, \quad (2.5)$$

where  $P(k)$  is the matter power spectrum (see Section 2.4 for more details). For pure thermal WDM models, as the ones we consider in this work, the transfer function can be approximated by:

$$T(k) = [1 + (\alpha k)^{2\nu}]^{-5/\nu}, \quad (2.6)$$

where  $\nu \approx 1.12$  and  $\alpha$  is related to the WDM particle mass by

$$\alpha \propto \left( \frac{m_{WDM}}{1 \text{ KeV}} \right)^{-1.11}. \quad (2.7)$$

The initial conditions are then generated at  $z = 99$  using the matter power spectrum, see [30] for more details.

On top of the hydrodynamics and gravity, the Sherwood code implements a variety of relevant physical processes that contribute to the state of the IGM and the Lyman- $\alpha$  forest. The simulations calculate the photo-ionisation and photo-heating for the gas (assumed to be in ionisation equilibrium) by using a uniform ionising UV background as described in [32]. Instead of following the star formation process, dense and cold gas particles ( $\Delta > 1000$  and  $T < 10^5 \text{ K}$ ) are converted into collisionless particles. The runs

Table 2.1: List of the **SHERWOOD** runs used in the work. All box sizes are  $20\text{h}^{-1}$ . The table shows the mean temperature of the IGM,  $T_0$ , at redshift  $z = 4.4$ , the redshift of reionisation, and the set of WDM masses included. We work with the inverse WDM mass and consider 0 to correspond to the CDM reference run.

Run	$T_0[\text{K}] (z = 4.4)$	$z_{\text{rei}}^{\text{end}}$	WDM[KeV $^{-1}$ ]
L20-ref	10556	6.00	$\{0, \frac{1}{2}, \frac{1}{3}, \frac{1}{4}, \frac{1}{8}, \frac{1}{12}\}$
L20-ref-hot	12161	6.01	"
L20-ref-cold	9862	5.98	"

discussed here do not include AGN feedback, which has a small effect on the Lyman- $\alpha$  forest at high redshift.

In our work, we use a subset of the **SHERWOOD** suite described in [26]. All boxes are of size  $20\text{h}^{-1}\text{cMpc}$ , with  $2 \times 1024^3$  particles. In Table 2.1 we summarise the runs used in this work.

The reference run is L20-ref. We will refer to the dataset consisting of this run as **SHERWOOD** in what follows. We also use two runs with varied thermal parameters L20-ref-hot and L20-ref-cold. The dataset consisting of all 3 runs will be denoted as **SHERWOOD THERMAL** in this work.

We conclude this section by visually inspecting the **SHERWOOD** data, to give a broad intuition of how the IGM fields behave. In Figure 2.2 we show a 2D neutral hydrogen overdensity field generated using the **SHERWOOD** suite at  $z = 4.2$  for multiple WDM models. The simulation size is  $20\text{h}^{-1}\text{cMpc}$ . On the horizontal axis, we linearly interpolate the density field for the WDM models to show the effect of multiple DM candidates on the density field. In Figure 2.3 we show a 1D neutral hydrogen overdensity field at  $z = 4.4$  along a  $20\text{h}^{-1}\text{cMpc}$  Sherwood skewer for the CDM model run. Note how the density field is periodic since the Sherwood simulations implement periodic boundary conditions. Most of the gas is close to the mean density  $\Delta \sim 1$ , with local overdensities that can generate  $\Delta \sim 20$  corresponding to regions where there is a positive flow of gas.

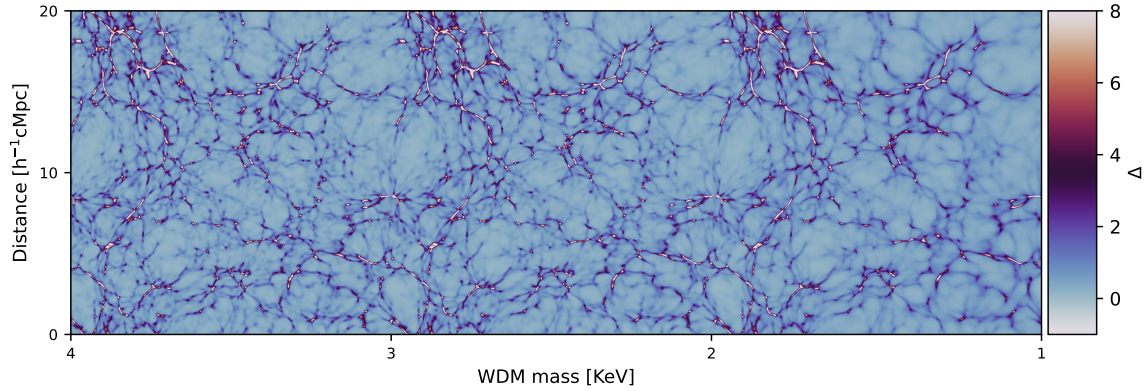


Figure 2.2: A 2D neutral hydrogen overdensity field generated using the **SHERWOOD** suite at  $z = 4.2$  for multiple WDM models. The simulation size is  $20h^{-1}\text{cMpc}$ . On the horizontal axis, we linearly interpolate the density field for the WDM models to show the effect of multiple DM candidates on the density field.

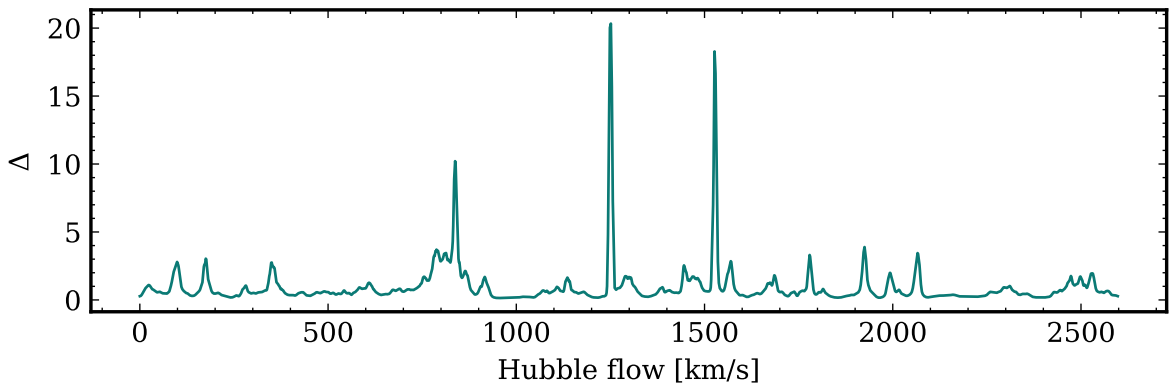


Figure 2.3: A 1D neutral hydrogen overdensity field at  $z = 4.4$  along a  $20h^{-1}\text{cMpc}$  Sherwood skewer for the CDM model run.

## 2.2 Obtaining mock Lyman-alpha skewers from cosmological simulations

The **SHERWOOD** simulation suite described in Section 2.1 generates as output the low-density IGM's overdensity, hydrogen neutral fraction, sightline velocity, temperature and the redshift of every pixel. For each run, those fields form a  $(5000, 2048)$  array for a total of 5000 sightlines per box. From such data, we can use Equation 1.35 to compute the simulated Lyman- $\alpha$  sightlines. We implement the code in Python and discretise the integral in Equation 1.35 to sum over all 2048 pixels in the skewer. We use the values for the recombination coefficient in [33].

In our code, we consider two different implementations for the Voigt profile, which is non-analytical. Firstly, we exploit the relationship with the Faddeeva function. The Faddeeva function is implemented in Scipy under `scipy.special.wofz` for optimized computation. Let us prove a relationship between the Faddeeva function and the Voigt function. Let  $z = x + iy$ . The Faddeeva function  $w(z)$  is defined as

$$w(z) = \frac{i}{\pi} \int_{-\infty}^{\infty} \frac{e^{-t^2}}{z - t} dt \quad (2.8)$$

and we have

$$\text{Re}(w(z = x + iy)) = V(x, y) \quad (2.9)$$

The proof is trivial:

$$\begin{aligned} \text{Re } i \int_{-\infty}^{\infty} \frac{e^{-t^2}}{z - t} dt &= \text{Re } i \int_{-\infty}^{\infty} \frac{e^{-t^2}(x - t - iy)}{(x - t)^2 + y^2} dt \\ &= y \int_{-\infty}^{\infty} \frac{e^{-t^2}}{(x - t)^2 + y^2} dt \end{aligned} \quad (2.10)$$

We consider a second implementation of the Voigt function by leveraging a power series expansion known as the Tepper-Garcia approximation [34]. The Tepper-Garcia approximation is

$$V(x, y) \approx e^{-x^2} \left( 1 - \frac{2y}{\sqrt{\pi}} K(x) \right), \quad (2.11)$$

with

$$K(x) = \frac{1}{2x^2} \left[ (4x^2 + 3)(x^2 + 1)e^{-x^2} - \frac{1}{x^2}(2x^2 + 3)\sinh x^2 \right]. \quad (2.12)$$

As can be seen from the Tepper-Garcia approximation, the Voigt function is a modified Gaussian function. Figure 2.4 shows a comparison between the Faddeeva and Tepper-Garcia implementations of the Voigt function for multiple values of the  $y$  parameter. Since in our problem, typical recombination coefficients are of order  $10^{-10}\text{cm}^3\text{s}^{-1}$ , both implementations are essentially equivalent.

An important aspect when simulating Lyman- $\alpha$  sightlines is boundary conditions. In fact, the simulation boxes in the `SHERWOOD` suite and other cosmological codes implement periodic boundary conditions. This means that a physical quantity  $Q$  satisfies

$$Q(0) = Q(L), \quad (2.13)$$

where  $L$  is the length of the simulation box. This condition also applies to the density

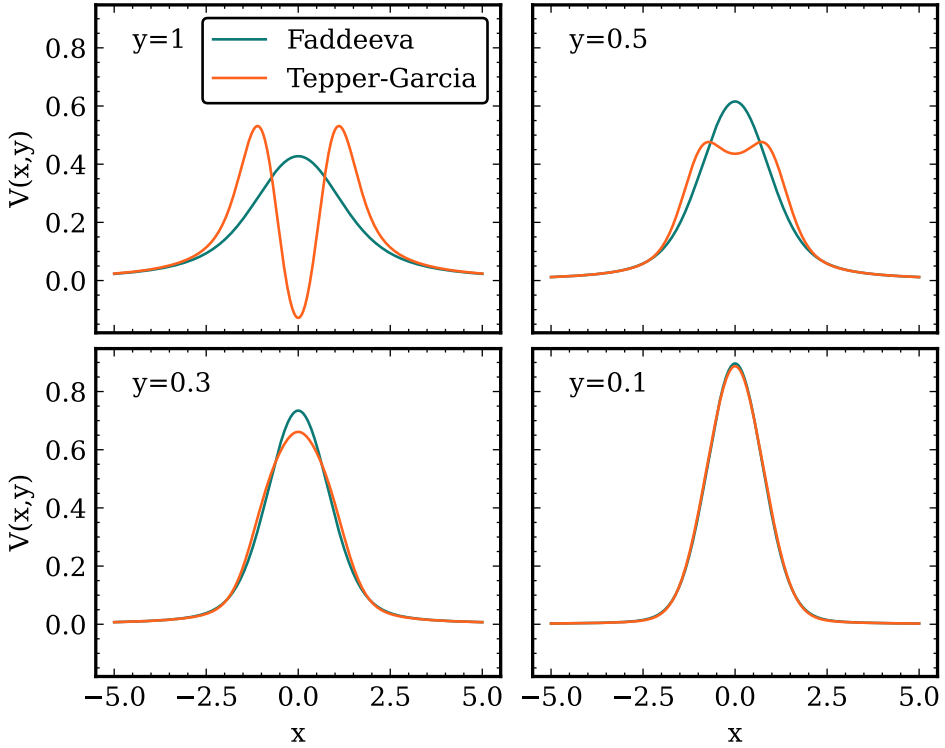


Figure 2.4: Comparison of the Voigt function  $V(x, y)$  that is included in Equation 1.35 implemented using the relation with the Faddeeva function in Equation 2.9 and the Tepper-Garcia approximation in Equation 2.11.

field, temperature field, etc. Periodic boundary conditions allow the implementation of relevant physical conditions, such as conserved quantities, in the simulation volume. As a consequence, we would like the optical depth fields generated using the **SHERWOOD** data to also implement periodic boundary conditions. This will be the case if every pixel in the sightline has the approximate same environment. To achieve this in a computationally efficient manner, observe that in Equation 1.35, for  $\alpha \rightarrow 0$ , the amplitude of the Voigt profile is set by  $b(T) \sim 10$  km/s for  $T \sim 10^4$ . Since the pixel scale is  $\sim 1$  km/s, the Voigt profiles only influence nearby pixels. As such, let us fix a pixel  $i$  on which we wish to calculate the optical depth. Then, we iterate over all pixels  $j$  and evaluate the condition  $|z[i] - z[j]| < L/2$ . If this condition is true, we use Equation 1.35 to compute the contribution. If the condition is false, then we use the pixel at  $z[j] \pm L/2$  that is closer to  $z[i]$ . This allows us to include (approximately) periodic boundary conditions with a complexity  $\mathcal{O}(N^2)$  where  $N$  is the number of pixels. For reference, see the optical depth field in Figure 2.5, where we have applied this procedure.

## 2.3 Peculiar velocities and optical depth-weighted quantities

Equation 1.35 relates properties of the low-density hydrogen in the IGM to the Lyman- $\alpha$  flux field. Each density pixel contributes to the optical depth at any fixed pixel by a quantity proportional to its density and to the absorption profile. However, note that the velocity contributes by shifting the centre of the absorption profile. As a consequence, the small-scale peculiar velocities of the absorbers due to structure formation wash out the correlation between the overdensity  $\Delta$  and  $\tau$  fields. A second undesirable effect of the velocity is that it can create potential degeneracies between the gas properties and the flux. In fact, the effect of the velocity field can be captured by considering a shifted density field generating the same flux field. These two problems mean that it is not feasible to recover the real  $\Delta$  from the flux. To better correlate the flux features with the density and temperature features and neglect the effects of peculiar velocities, it is common in the literature to work with optical depth-weighted quantities [35]. Such quantities allow for better identification of the gas associated with a certain absorption profile. Optical depth quantities are highly correlated to real quantities and act as a proxy for the latter [36].

We define the optical depth-weighted overdensity field,  $\Delta_\tau$ , as

$$\Delta_{\tau,i} = \sum_j \tau_{ij} \Delta_j / \tau_i, \quad (2.14)$$

where  $\tau_{ij}$  is the contribution to optical depth at pixel  $i$  by pixel  $j$ . Equation 2.14 can also be used to compute the optical depth-weighted temperature. Figure 2.5 shows a  $20h^{-1}\text{cMpc}$  SHERWOOD CDM skewer at  $z = 4.4$  with 2048 pixels. We show the hydrogen overdensity  $\Delta$ , temperature  $T$  and velocity along the sightline  $V$ , Lyman- $\alpha$  optical depth and flux computed according to Equation 1.35. We also show the optical depth-weighted overdensity and temperature, computed according to Equation 2.14. Note how optical depth-weighted fields smooth out fluctuations in the small scales since Equation 2.14 is essentially a weighted convolution. The main effect of optical depth-weighted fields is that they are highly correlated to the flux field, with a limited shifting effect due to local velocities. For instance, consider the optical depth peak at  $\sim 880$  km/s, which is associated with a real  $\Delta$  peak at  $\sim 840$  km/s due to peculiar velocity effects. However, the  $\Delta_\tau$  peak closely follows to optical depth peak.

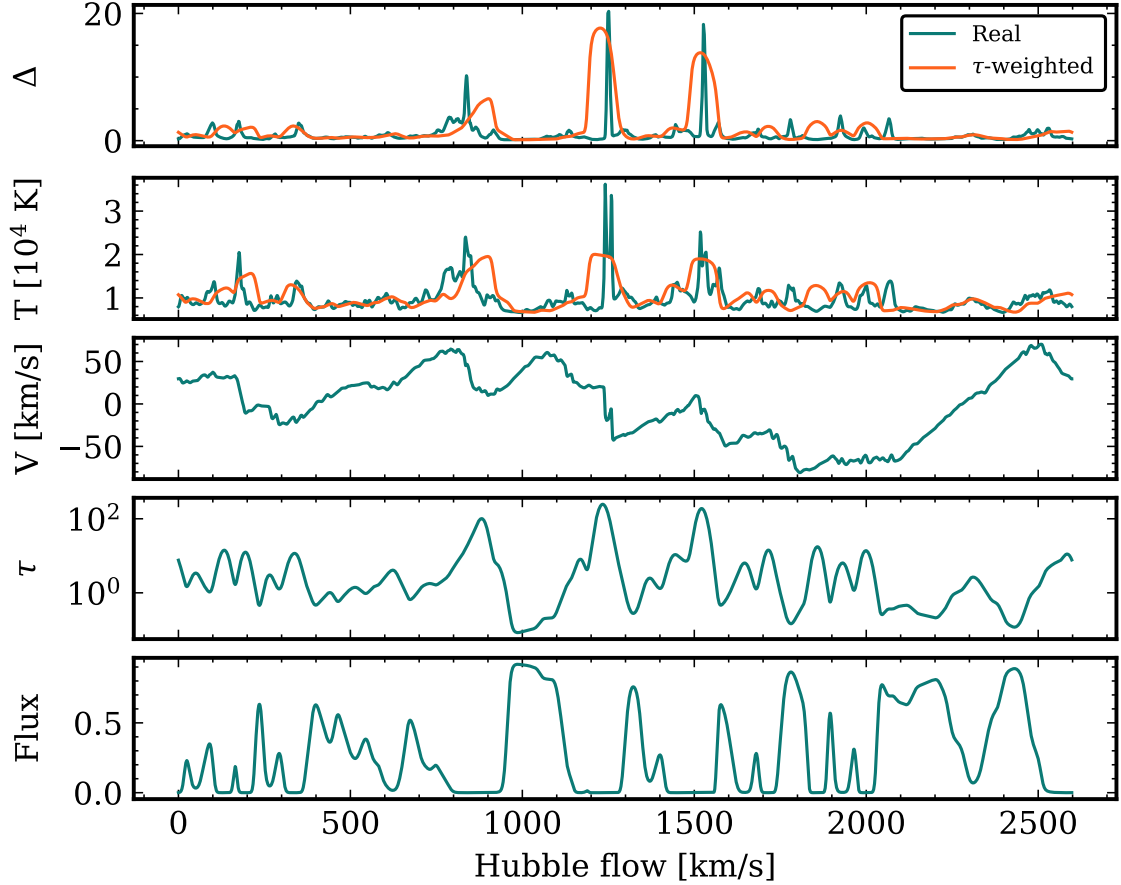


Figure 2.5: A  $20\text{h}^{-1}\text{cMpc}$  SHERWOOD CDM skewer at  $z = 4.4$  with 2048 pixels. We show the hydrogen overdensity  $\Delta$ , temperature  $T$  and velocity along the sightline  $V$ , Lyman- $\alpha$  optical depth and flux computed according to 1.35. We also show the optical depth-weighted overdensity and temperature, computed according to 2.14

## 2.4 Statistical analysis of the effect of dark matter in the flux and density fields

In Section 2.1 we have presented the `SHERWOOD THERMAL` simulation suite, which includes runs with the same initial seed but different thermal parameters and WDM particle masses. Naturally, changing such parameters modifies the IGM and Lyman- $\alpha$  forest properties. In this section, we explore how the density field and the Lyman- $\alpha$  forest are modified by such parameters within the `SHERWOOD` suite. In Figure 2.6 we show an example of this process. The figure shows the  $\Delta$  overdensity and flux for 3 different WDM models in the `SHERWOOD` suite at  $z = 4.4$ . Note how the CDM skewers show more fluctuations and pronounced features than the WDM models.

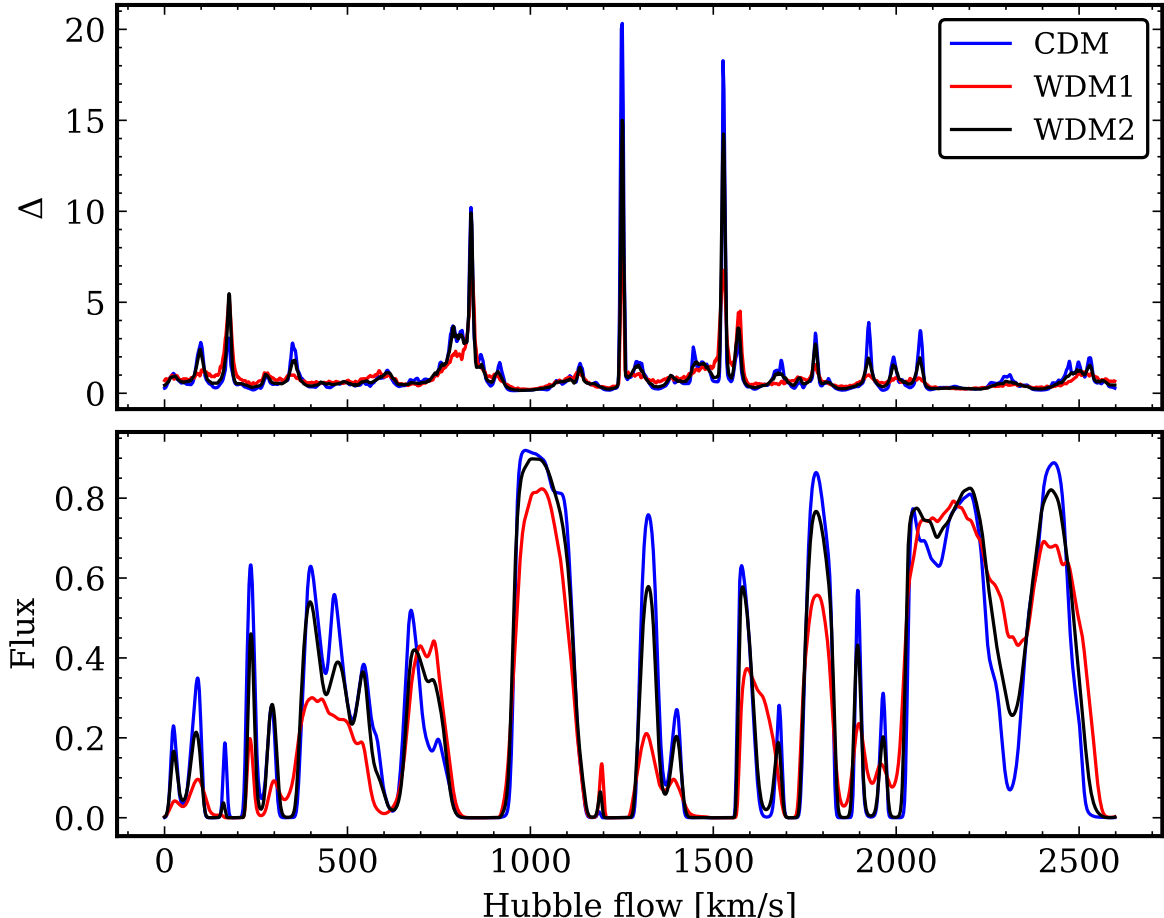


Figure 2.6: The  $\Delta$  overdensity and flux for 3 different WDM models in the `SHERWOOD` suite at  $z = 4.4$ . Note how the CDM skewers show more fluctuations and pronounced features than the WDM models.

To quantify this in a more robust and precise way, we leverage two summary statistics, the Probability Distribution Function (PDF) and the Power Spectrum (PS), that aggregate multiple skewers to produce quantities that only depend on the statistical properties of the fields, and not on the specific simulation seed for the sightline.

For a given set of sightlines, the PDF of a field is the histogram of values for such field on the array obtained concatenating the skewers. We use Numpy’s `numpy.histogram` to compute it and Rice’s rule to obtain the number of bins. According to this rule, for  $N$  observed values, the number of bins in the histogram should be  $\sim 2N^{1/3}$  [37]. For data with 2048 pixels, we use 21 bins. Since in this section we are only interested in quantifying the statistics for every model, we refer to Section 3.4 for a discussion of the uncertainty estimation in field statistics.

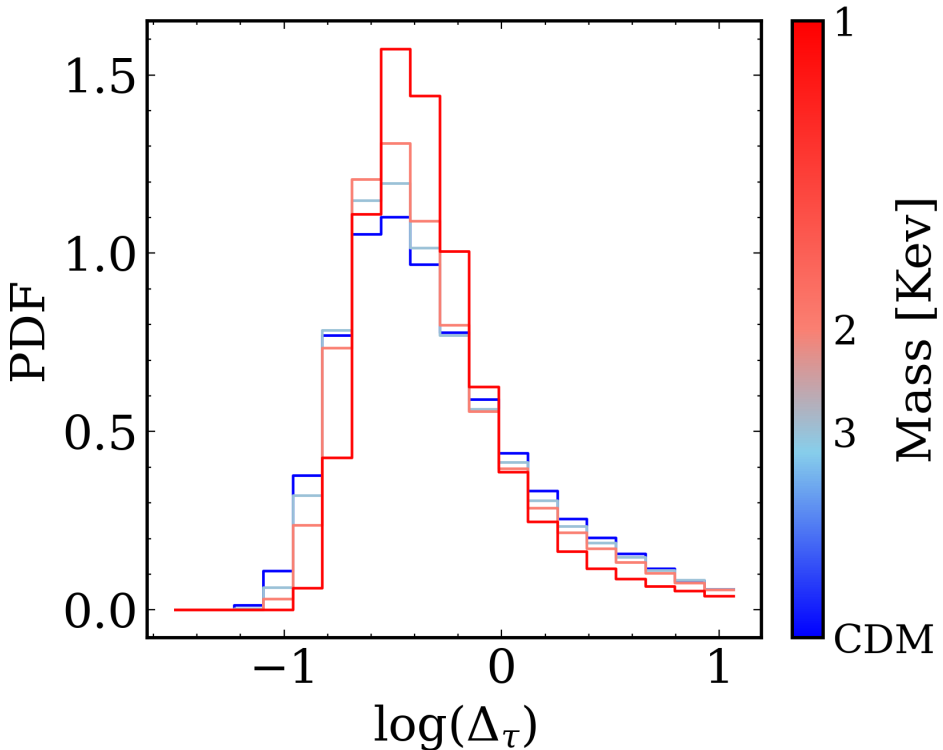


Figure 2.7: The  $\Delta_\tau$  probability distribution function (PDF) at  $z = 4.4$  for different WDM models in the **SHERWOOD** suite.

In Figure 2.7 we show the  $\Delta_\tau$  PDF at  $z = 4.4$  for different WDM particle masses in the **SHERWOOD** suite. Note how low mass models tend to have a more localised distribution near the mean, which reflects the observation from Figure 2.6 that such models have smoother fields. In contrast, the CDM model has a greater variance, reflecting the fact that more pronounced features occur, which leads to more extreme values for the fields.

The PDF quantifies how often a certain value occurs, but not the correlations in the field. To study the oscillations in the fields it is common in the literature to use the Power Spectrum (PS) [38, 39]. The PS is defined in Fourier space of the relevant field, up to a normalisation factor. Here, we focus on the Lyman- $\alpha$  flux field,  $F$ , since it has been measured from multiple quasar samples. Since we are only interested in how  $F$  oscillates, we consider the flux contrast

$$\delta F = \frac{F}{\bar{F}} - 1, \quad (2.15)$$

where  $\bar{F}$  is the mean value of the field. The power spectrum  $P_k$  is defined as the modulus of the normalised Fourier transform of  $\delta F$ :

$$P_k = \left| \mathcal{F} \left( \frac{1}{N} F \right) \right|^2, \quad (2.16)$$

where  $N$  is the number of pixels on a sightline (2048 for **SHERWOOD**) and  $\mathcal{F}$  denotes the (Fast) Fourier Transform operator. Note that, by the Wiener-Khinchin theorem, the power spectrum is just the Fourier transform of the autocorrelation function of the  $\delta F$ . We compute the PS using Numpy’s `numpy.fft` class. The wavenumber  $k$  is binned in log space, with a spacing of  $\Delta \log(k) = 0.1$  in the same manner as [40]. To compare the PS from the **SHERWOOD** data to real observations, we normalise the flux field to match the mean observed flux in [41]. We do this by introducing a factor  $a$  in the optical depth such that  $F = e^{-a\tau}$  matches the mean observed flux at every redshift. Figure 2.8 shows the Lyman- $\alpha$  flux power spectrum for different WDM models in the **SHERWOOD** simulation suite, compared to the observed PS by [40]. We begin by observing that WDM models have the effect of suppressing structure only in the small scales (high  $k$  values). At large scales, all WDM models have a similar power spectrum. Lower masses suppress the PS more than WDM models close to CDM. In Figure 2.8, we observe a systematic bias where the Sherwood CDM power spectrum underestimates the observed power spectrum in [40]. In the original Sherwood publication [30], a continuous bias correction factor is applied to the flux in order to forward model the skewers, in addition to matching the observed effective optical depth. This bias correction, which has not been incorporated in this work, could be the origin of the differences observed in the figure. In the rest of the work, we will use the PDF statistic when constraining WDM, so that this PS bias will not be a concern.

Since both the thermal state of the IGM and the WDM particle mass affect the Lyman- $\alpha$  forest, we could ask whether those two effects are degenerate. In fact, a

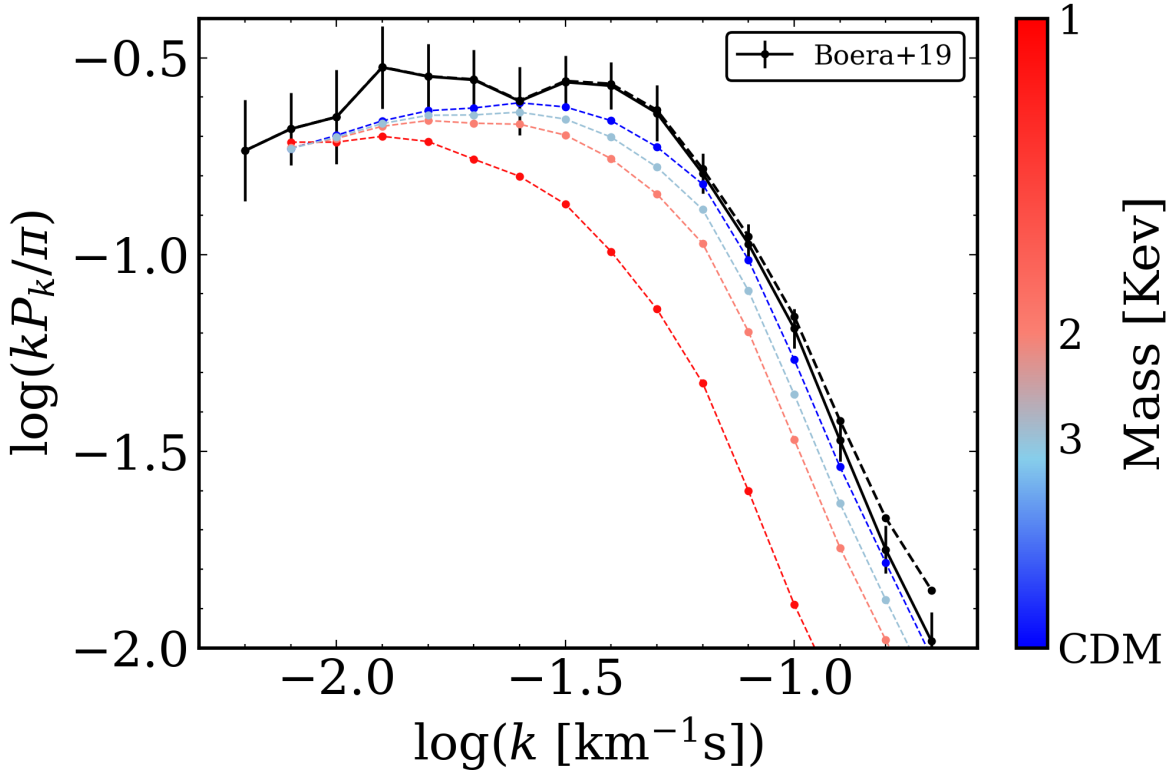


Figure 2.8: The Lyman- $\alpha$  flux power spectrum for different WDM models at  $z = 4.2$  in the `SHERWOOD` simulation suite. For reference, we also plot the observed PS by [40].

hotter IGM means that the Voigt absorption profiles are wider, which smoothes out the forest at small scales, similar to the effect how low WDM masses. If those two effects are completely degenerate, a smoother Lyman- $\alpha$  forest would not allow discriminating between a hotter IGM and a smaller WDM particle mass. In Figure 2.9 we show a comparison at  $z = 4.4$  of the effect of WDM models and thermal models within the `SHERWOOD THERMAL` suite on the Lyman- $\alpha$  flux power spectrum. Note that both effects are not completely degenerate. WDM models only suppress the power spectrum at small scales, while hotter models modify the power spectrum in the whole wavenumber range. As a consequence, the Lyman- $\alpha$  forest breaks the degeneracy between thermal and WDM models.

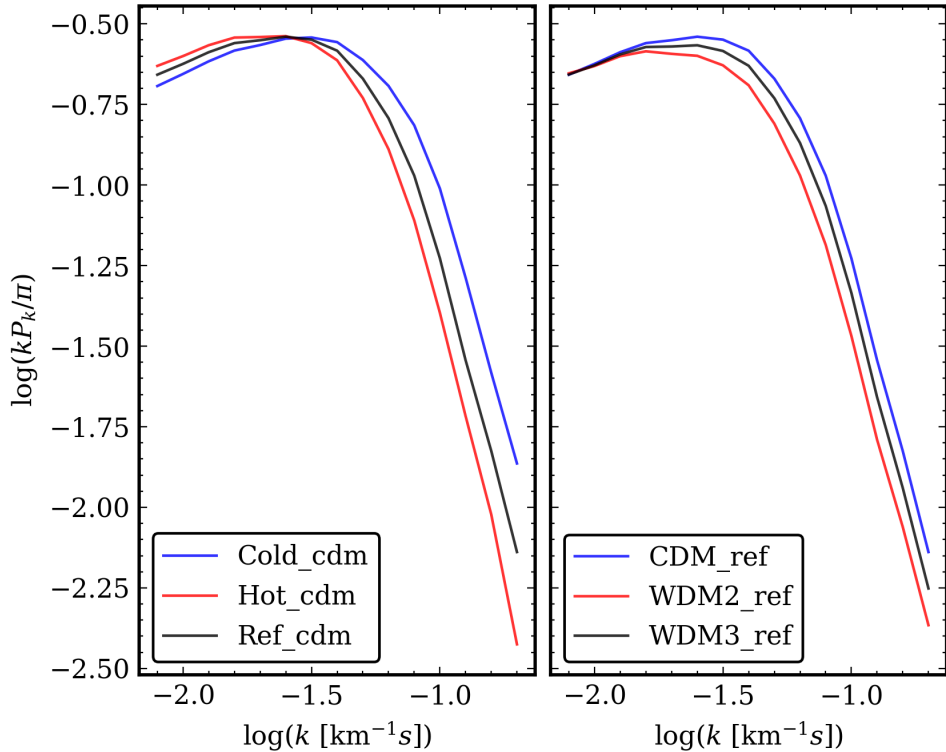


Figure 2.9: A comparison at  $z = 4.4$  of the effect of WDM models and thermal models within the **SHERWOOD** suite on the Lyman- $\alpha$  flux power spectrum. Note that both effects are not completely degenerate. WDM models only suppress the power spectrum at small scales, while hotter models modify the power spectrum in the whole wavenumber range.

# 3 Deep Learning the Lyman-alpha forest

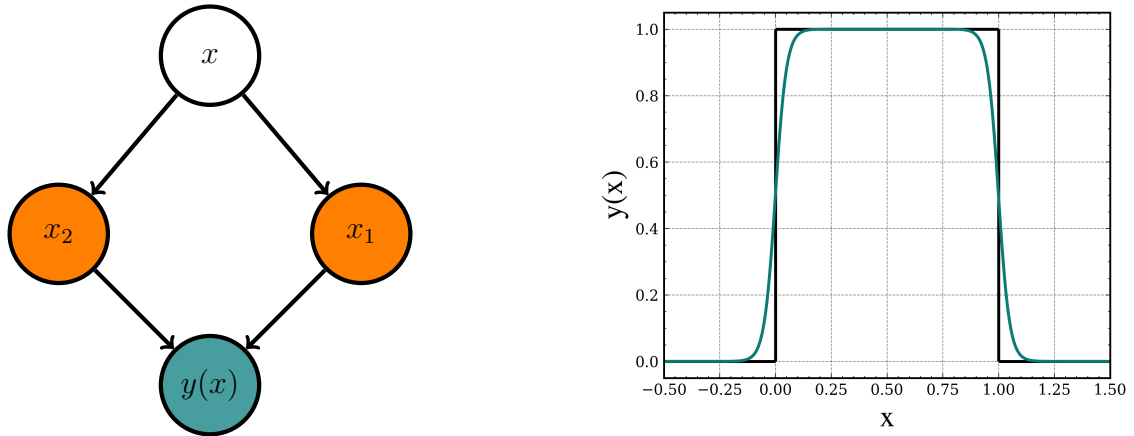
## 3.1 Introduction and motivation for the use of Deep Learning

In this section, we introduce a deep-learning machinery that can reconstruct the neutral hydrogen density field from an observed Lyman- $\alpha$  forest. We begin by giving a broad introduction to machine learning and neural networks and then focus on their application to our cosmological problem.

Fundamentally, a neural network is a directed and acyclic computational graph [42]. It represents a set of operations that transform input data input into an output. In the simplest case of a fully connected network, the nodes of this graph are represented by neurons. Neurons are organized on successive layers, making the information flow from one layer to the following one. In the most basic scenario, the neurons in a given layer are linearly connected to the neurons in the previous layer. Each neuron then adds a bias to the result of the computation and applies a non-linear function to the result, which determines the activation state of the neuron. Consider the graph shown in Figure 3.1a, where the input neuron has a value  $x$  and the output neuron has a value  $y(x)$ . The intermediate layers have values

$$\begin{cases} x_1 = \sigma(\alpha_1 x + \beta_1) \\ x_2 = \sigma(\alpha_2 x + \beta_2) \end{cases}, \quad (3.1)$$

where  $\alpha_i$  are the linear weights,  $\beta_i$  the biases, and  $\sigma$  is a non-linear activation function. Typical choices include tanh or ReLU (Rectifier Linear Unit) given by  $\text{ReLU}(x) = \max(0, x)$ . Graphs such as the one shown in Figure 3.1a are known as *fully connected layers*. Much more complex architectures have of course been investigated. Depending on the specific problem and dataset, we can incorporate a priori knowledge of the



(a) Graph for a simple MLP with a hidden layer (in orange) and an output neuron (in cyan).

(b) Unit impulse (in black) and the output of the MLP shown in cyan approximating the impulse.

Figure 3.1: A simple multilayer perceptron (MLP) with a single hidden layer and a tanh activation function can approximate a unit pulse function. From left to right and top to bottom, the three biases are  $\{0, 20, 0\}$  and the four weights are  $\{20, -20, 1/2, 1/2\}$ .

problem in the design of the network. For instance, in Computer Vision, the use of *convolutional layers* especially targeted at identifying key features in images has proven to be extremely successful [43]. In the analysis of time series, Long Short-Term Memory (LSTM) neurons allow the network to “remember” information from previous inputs [44].

From the theoretical standpoint, neural networks are universal approximations (for sufficiently well-behaved functions), which makes them especially appealing in the modelling of complex systems. A concrete result is as follows [45]:

**Theorem 1** (Universal approximation theorem). *If  $f: \mathbb{R}^n \rightarrow \mathbb{R}^m$  is a Lebesgue  $p$ -integrable function and  $\varepsilon > 0$ , then there exists a fully connected ReLU network  $F: \mathbb{R}^n \rightarrow \mathbb{R}^m$  such that*

$$\int_{\mathbb{R}^n} \|f(x) - F(x)\|^p dx < \varepsilon.$$

Theorem 1 can be expanded to include tight bounds on the depth or width of the network, which then depend on  $n$  and  $m$ . Note that all the complexity of a fully connected neural network is generated by the non-linear activation function. With a linear activation function, a fully connected network would be an affine transformation, which cannot approximate arbitrary non-linear functions.

This theoretical result can be easily visualized by understanding how a simple fully

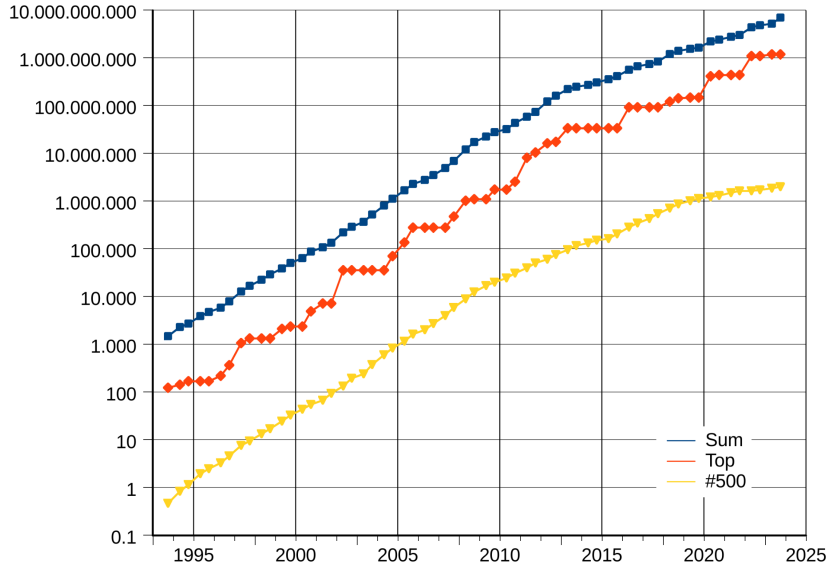


Figure 3.2: Evolution of the largest supercomputers in the TOP500 list in recent years (x-axis). The y-axis shows the peak performance in GFLOPS for the first-ranked computer (red), the last-ranked computer (yellow), and the cumulative power for the top 500 computers (blue). Source: Wikipedia.

connected network (a multilayer perceptron, MLP) can approximate a unit impulse function. It is then enough to recall that a linear combination of step functions can approximate any integrable function. In Figure 3.1a we show an MLP consisting of an input neuron, an output neuron and a hidden layer with two neurons with a tanh activation function. From left to right and top to bottom, we set the three biases as  $\{0, 20, 0\}$  and the four weights as  $\{20, -20, 1/2, 1/2\}$ . The resulting MLP then produces the approximation shown in figure 3.1b of the unit impulse over  $[0, 1]$ . By expanding the number of neurons in the hidden layer we could approximate impulse functions of arbitrary width and height and centered at every arbitrary value. The high degree of expressivity of neural networks makes them particularly suited to parametrically approximate complex non-linear relationships between variables that would otherwise be intractable.

Theorem 1 establishes a theoretical aspect of neural networks supporting their utility, but it does not provide a method (nor does it guarantee the existence of any) to find networks that approximate a particular function of interest. The process of fitting a statistical model (such as a neural network) to a dataset of interest is known as *supervised learning*, and constitutes one of the main aspects of this work, as we will explain in the rest of this section. In recent years, some factors have allowed the rapid expansion

of machine learning, marking a new era in the use of large parametric networks for real-world problems:

- **Hardware development.** The rapid (quasi-exponential) growth in computer power in recent years, as exemplified by Moore’s law [46], means that extremely deep and complex models can now be trained and effectively used. As a reference, the language models LLAMA by Meta can have over 65 billion parameters [47]. To handle this amount of data, High-Performance Computing (HPC) infrastructures (such as supercomputers) are needed. Figure 3.2 shows the rapid evolution of the top supercomputers in the world, as ranked by the TOP500 list<sup>1</sup>. In 1993, the FUJITSU NUMERICAL WIND TUNNEL in Japan topped the list with 124 GFLOPS. In 2023, the list is topped by FRONTIER in the United States, with over 1000 PFLOPS, which corresponds to an 8000-fold improvement. Progress in hardware technology has also been remarkable. For instance, Graphics Processing Units (GPU) are now common when training machine learning models. As a last example, in May 2017, Google introduced an architecture known as Tensor Processing Unit (TPU) specially designed to accelerate neural network operations [48]. HPC also enables the generation of synthetic datasets from simulations, that can then be used as training datasets. We will leverage this idea in the rest of this work.
- **Computationally-efficient algorithms.** Together with hardware development, we have seen a rapid evolution of computational and mathematical algorithms in the field of statistical learning that has enabled the efficient utilisation of HPC resources. The epitome of such an algorithm might be *backpropagation* [49] which is the most common algorithm used in the training phase to update the weights when deploying a neural network. Together with backpropagation, a growing set of optimisers for deep learning problems has been developed. A popular choice is ADAM, which was originally published in 2017 [50].
- **Availability of large datasets.** The advent of next-generation instruments and data-collection systems provides the scientific community with increasingly large datasets. Prominent examples in the field of astronomy include Gaia [51], whose third data release (DR3) includes 10 TB of data for 1.46 billion sources<sup>2</sup>, or the

---

<sup>1</sup><https://top500.org>

<sup>2</sup><https://www.cosmos.esa.int/web/gaia/dr3>

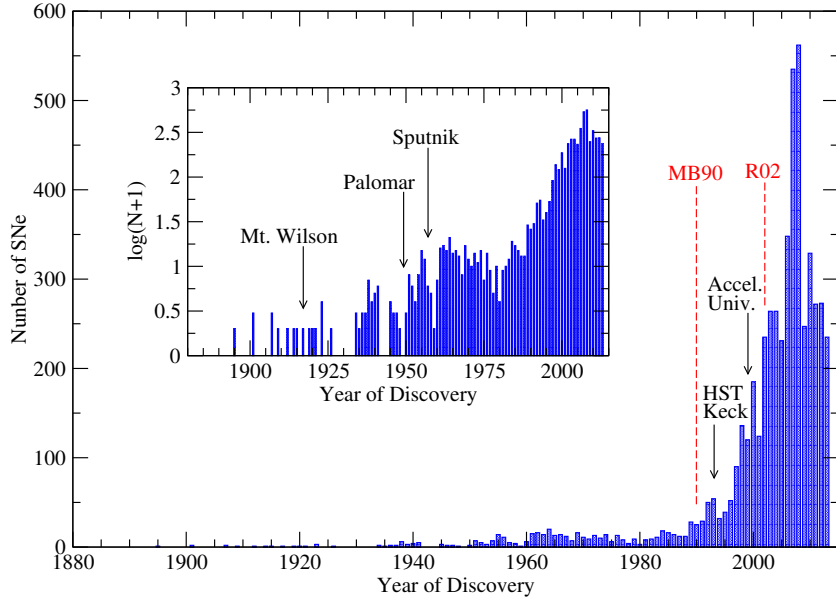


Figure 3.3: Histogram showing the number of SNe discovered each year as given by the Asiago Supernova Catalogue.

Euclid telescope, expected to deliver 850 GB of compressed data per day<sup>3</sup>. At last, in Figure 3.3 we show the evolution in the number of SNe discoveries per year. The figure has been obtained from [52].

Let us demonstrate the relevance, pertinence, and range of applicability of machine learning methods in astronomy and cosmology by examining recent endeavours documented in the literature. While not exhaustive, this examination provides a broad overview of previous efforts in the field and illustrates some recent successes of machine learning-oriented approaches in data-driven problems.

The abundance of data from surveys covering large regions of the sky aimed at targeting QSOs makes supervised statistical techniques a particularly attractive data analysis technique. For reference, the main quasar sample in the data release number 16 for the Extended Baryon Oscillation Spectroscopic Survey (eBOSS) contains 434820 targets with redshifts in the range  $0.8 < z < 2.2$  [53]. The prediction of the intrinsic Lyman- $\alpha$  emission line from high redshift QSOs is a non-trivial problem that has important implications in the study of IGM damping wings and the reionization of the later [54]. Reconstruction techniques often rely on the correlation of the Lyman- $\alpha$  peak with other observable lines and information redward of the Lyman- $\alpha$  line. Machine learning approaches are then suitable to connect the unattenuated information redward

<sup>3</sup><https://sci.esa.int/web/euclid/-/46661-mission-operations>

of the Lyman- $\alpha$  peak with its intrinsic profile. In *Blind QSO reconstruction challenge: Exploring methods to reconstruct the Ly $\alpha$  emission line of QSOs* [55], the authors perform an in-depth comparison of different state-of-the-art techniques based on statistical learning. The authors blindly evaluate their performance on two QSO samples randomly extracted from X-Shooter and BOSS with  $3.5 < z < 4.5$ , in such a way that selecting samples already used in the training data set was avoided. The various techniques range from principal component analysis (PCA) approaches, such as [56], to deep learning networks [57]. The authors conclude that the better-performing pipelines consistently rely on machine-learning approaches. The authors caution against overreliance on machine learning techniques due to their potential lack of statistical uncertainty, which is one of the main aspects that we will develop in this work.

Parameter inference on WDM using deep learning has already been tentatively explored in the recent literature. The paper *Inferring Warm Dark Matter Masses with Deep Learning* [58], which is especially relevant for this work, demonstrates that neural networks can be used to recover WDM parameters from observed field density images. The authors present a suite of 1500 cosmological N-body simulations with varied WDM mass in the range of 2.5 to 30 KeV. Field density images of size  $25h^{-1}\text{Mpc}$ , with varied image resolution, simulation resolution and redshift (in the range  $0 \leq z \leq 5$ ) are extracted from the simulation runs. The images are augmented with usual standard techniques (such as image rotation) and then incorporated into training datasets. The authors use a Convolutional Neural Network (CNN) trained to directly predict WDM masses based on an input density field image. Their fiducial convolutional network trained with the set of the highest resolution images is able to accurately recover WDM masses with an accuracy of  $\pm 1$  KeV for models up to 10 KeV. After this threshold value, the network is no longer able to recover the true mass as predicts an approximately constant mass, see Figure 3.4. Note that in the architecture presented by the authors, the network is also trained to predict an uncertainty estimate. Another interesting insight offered by this paper refers to the capacity of neural networks to make use of the full information contained in a field distribution (in this case, the density field). By training a network on a full-density field image the models learns the relevant properties of the field that can lead to an accurate parameter prediction. The authors train another model only on summary statistics, in particular, on the density power spectrum, and compare its performance with their fiducial model trained on the full images. The model trained only on the power spectra shows a significantly degraded performance, with higher uncertainties and accurate prediction only up to 5.5 KeV. This illustrates

Figure 3.4: Figure extracted from [58]. The left panel shows a sample image density field used in the training data by the authors, with varied image resolution. The right panel shows a sample of predicted WDM masses versus the true WDM mass of the simulation for their fiducial neural network, which can accurately recover the WDM model within a 1 KeV accuracy of up to 10 KeV.

how deep learning techniques can help to harvest the full information present in a field (or generally, in a complex input tensor).

Another recent use of deep learning to analyse IGM data can be found in the paper  *$\text{Ly}\alpha\text{NNA}$ : A Deep Learning Field-level Inference Machine for the Lyman- $\alpha$  Forest* [59], where authors harvest the field level potential of residual convolutional networks to perform inference on the thermal parameters of the IGM, namely  $T_0$ , the temperature at mean density, and  $\gamma$ , the slope of the temperature-density relation. Their model is trained on simulation boxes with a side length of 120 Mpc from which  $10^5$  sightlines are extracted and processed to produce mock Lyman- $\alpha$  spectra. The simulation boxes are run with different thermal parameters, by sampling 121  $(T_0, \gamma)$  combinations in

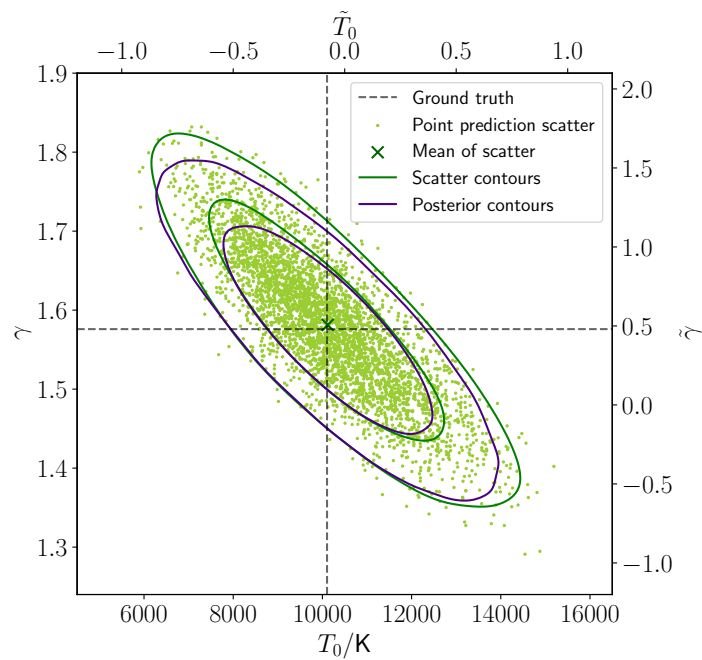


Figure 3.5: Figure extracted from [59] showing the performance of the neural network recovering thermal parameters on a set of unseen skewers. The true parameter values, shown as dashed lines, are recovered by the average of the point predictions, shown as the dark green cross.

## 3.2 Fundamentals of (Bayesian) Neural Networks

A very general regression problem in statistical learning [60] arises when we observe a quantity  $Y$  that is assumed to depend on an independent variable  $X$  through a relation of the form

$$Y = f(X) + \mathcal{N}(0, \sigma), \quad (3.2)$$

where  $f$  is a function defining the relation  $Y = Y(X)$  and  $\mathcal{N}(0, \sigma)$  is an error term modeling a zero-mean Gaussian noise. The problem then consists of estimating  $f$  given a sample of observations  $\{X_i, Y_i\}_i$  to obtain a functional form  $\hat{f}$  that can then be evaluated to obtain predictions. Following the examples in Section 3.1,  $X$  might be the flux spectra redward of the Lyman- $\alpha$  peak, and  $Y$  might then be the intrinsic shape of the Lyman- $\alpha$  peak in the quasar spectra. The noise then is produced by different sources, for instance, associated with the instrumental devices. We could then use the obtained  $\hat{f}$  to predict the intrinsic Lyman- $\alpha$  peak of a QSO,  $\hat{f}(X)$ , when we only have information about the spectrum redward of it,  $X$ . As it is expected, the quality of our prediction depends on how accurate is the approximation  $\hat{f}$  with respect to  $f$ , but also on how noisy our data is. In fact, we see that, if the true quantity associated with  $X$  is  $Y$ :

$$(Y - \hat{f}(X))^2 = (f(x) + \mathcal{N}(0, \sigma) - \hat{f}(X))^2.$$

Taking expected values and noting that the only stochastic component here is the noise, we obtain

$$\mathbb{E}[(Y - \hat{f}(X))^2] = (f(X) - \hat{f}(X))^2 + \sigma^2. \quad (3.3)$$

In Equation 3.3, the first term of the right-hand side represents the error produced by approximating  $f$  by  $\hat{f}$ , while the second term is a theoretical limit imposed by the noise properties.

Parametric methods represent a powerful statistical learning tool to approximate the target relation  $f$  between variables. Methods such as linear regression, which approximates  $Y = f(X)$  using a linear functional form on the parameter values, offer limited flexibility in terms of approximating complex relations but allow for a high degree of interpretability of the model. On the other end of the spectrum, deep learning models offer a large degree of expressivity (see Section 3.1), but interpretation of individual parameters is often not possible. Increasing the number of parameters can also cause the model to learn from spurious structures in the finite data sample, or learn from possible

noise correlations. This process, known as *over-fitting*, can significantly impact the predictive performance of the model when predicting on unseen data. Multiple techniques have been explored to mitigate over-fitting [61], we will adopt some of them in this work and explain them in the following sections.

In this section, we will discuss the basic workflow involving a deep learning model in a general and abstract scenario. We will restrict ourselves to the topics that are relevant to this work, and later explain in detail how we implement this workflow for our problem. The general workflow when working with a deep learning statistical model under supervised learning includes the following phases:

1. Collecting data and processing it to generate a training dataset. This requires specific domain expertise to assess the quality and representability of the data.
2. Designing a deep learning architecture, i.e., a computational graph that depends on a set of parameters and generates target outputs from the input data.
3. Using the available data to train the model. This is done by optimising the model parameters by minimising a selected loss function.
4. Assessing the performance of the network using a previously unseen dataset.
5. Using the model on real unseen data to make predictions.

### 3.2.1 Dataset generation, data augmentation and overfitting

In a general real-world setting, only a finite dataset is available to us, for instance, obtained from observational procedures. That is, we have a set of pairs  $\mathcal{D} = \{X_i, Y_i\}_{i=1}^{i=N}$  of  $N$  observations from an input-output pair, distributed according to some distribution  $F(X, Y)$ :

$$(X_i, Y_i) \sim F, i = 1, \dots, N. \quad (3.4)$$

Of course, in general, we don't have access to the distribution of this population (i.e., the function  $f$  describing the data relation  $Y = f(X)$ ), otherwise, we would already have a perfectly accurate model, and we would not invoke any statistical learning tool. The challenge is then to use our sample  $\mathcal{D}$  to infer properties of the population. Since we don't have access to the generating function  $f$ , we cannot assess the general performance of the model on arbitrary input data. For this purpose, the training dataset  $\mathcal{D}$  is typically split into two disjoint subsets  $\mathcal{D} = \mathcal{D}_T \sqcup \mathcal{D}_V$ , where  $\mathcal{D}_T$  represents the subset of the data used for training, and  $\mathcal{D}_V$  represents the subset of the data used to validate the

model and assess its performance. The central idea behind this split is to be able to validate the model on data that has not been used in the training process, allowing for an estimation of the model’s generalisation to the population given by:

$$\varepsilon = \mathbb{E}_F[\mathcal{L}(Y, \hat{f}(X|\mathcal{D}_T))], \quad (3.5)$$

where  $\mathcal{L}$  is a loss function. The exact form in which  $\mathcal{D}$  is split needs to be chosen a priori to have a representative sample of the population. A common easy-to-implement strategy is to randomly select the samples in  $\mathcal{D}$  that will be part of  $\mathcal{D}_V$  and distribute them according to a ratio, that is commonly taken to be in the range 60 – 80%, meaning that a larger percentage of  $\mathcal{D}$  is dedicated to training. In this case, an unbiased estimator of  $\varepsilon$  is

$$\hat{\varepsilon} = \frac{1}{|\mathcal{D}_V|} \sum_{i=1}^{|\mathcal{D}_V|} \mathcal{L}(Y_i, \hat{f}(X_i)), \quad (3.6)$$

where the sum runs over the validation dataset. More complex strategies that take into account the topology of the data exist and allow for an optimal training-validation split [62]. The validation subset can also be sequentially cycled through all the available samples in a series of methods called *cross-validation* [63]. Cross-validation uses all available data in a validation stage by retraining a model on different disjoint splits of the data. This allows for a more precise evaluation of the model.

If the training subset  $\mathcal{D}_T$  is not representative of the population, then the global error in Equation 3.5 will be large, and the model will not be able to learn the general properties of the data. This can cause the model to overfit and learn from spurious correlation in the data and noise, and can be encouraged by having an excessive number of free parameters. Overfitting is not an intrinsic characteristic of deep-learning models, and can also be seen for instance in simple polynomial regression when the number of “independent” points exceeds the order of the fitting polynomial. Figure 3.6 illustrates the simple example of polynomial regression overfitting the training dataset as the order of the polynomial increases. Note how, by construction, the fit becomes increasingly accurate on the training data, but loses generalisation power on unseen points.

The training data  $\mathcal{D}_T$  can be artificially extended using *data augmentation* techniques [64] to generate new training points from existing points. Data augmentation aims at presenting the model with data that maintains the intrinsic properties of the original data but varies other features that should not affect the prediction. This approach

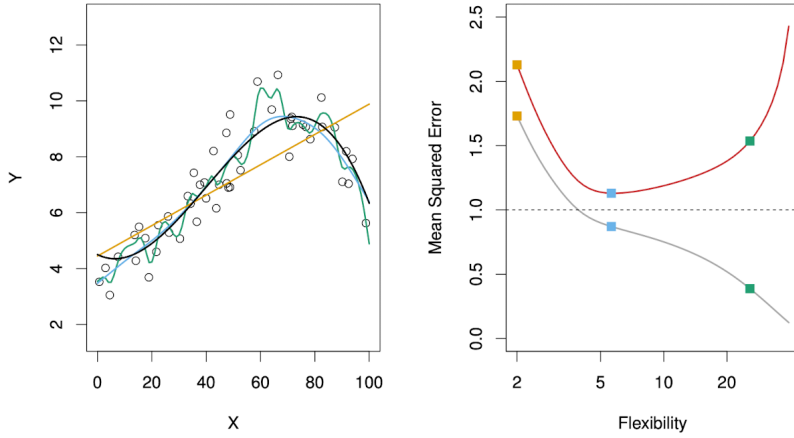


Figure 3.6: The left panel shows the data points (with added noise) generated from a function  $f$  in black. Three generative polynomial models are fitted to the data: linear regression in orange, and two smoothing splines in green and blue. The right panel shows the fitting error as a function of the polynomial degree, i.e., the flexibility of the model. The grey curve shows the error on the training dataset, which is monotonically decreasing. The red curve shows the error on the validation dataset, which initially decreases but then grows as the model overfits the training data. Figure extracted from [60].

can be understood to be inspired by symmetry considerations<sup>4</sup> and is particularly useful in computer vision tasks. Some common data augmentation techniques for image processing include:

- Basic geometric transformations such as rotation, translation or flipping an image (or field) are efficiently implemented. Cropping can also be easily implemented but changes the dimensionality of the data.
- Basic colour space manipulation in coloured images, including isolating a single colour channel, or modifying the brightness of an image.
- Noise injection during training is particularly useful in making neural networks robust against noisy and corrupted data. Note that this can be relevant if the data we are expecting to use the trained model on is noisy (for example instrumental data from a spectrograph). The noise can be randomly drawn from independent distributions, or drawn from a noise model if we have additional insights on how to model it.

<sup>4</sup>A strawberry is a strawberry regardless of its orientation

- Convolutional operations with kernels, such as the Gaussian kernel, apply a limited spatial resolution (blurring), or the Sobel kernel related to edge detection.

### 3.2.2 Deep learning architecture

The network architecture defines the parametrization of the function that approximates the true underlying relation between input and output data points. In this section, we briefly explore some basic building blocks used when constructing a deep learning network. A neural network (NN)  $\phi$  is a computational graph with an input tensor  $X$  and an output tensor  $Y$  and parametrized by a set of values  $\omega$  that define a functional model

$$Y = \phi(X|\omega) \equiv \phi_\omega(X). \quad (3.7)$$

For simple linear topologies, NN can be specified given a set of connected *layers* that carry out the elementary operations. These layers can be grouped in *blocks* to form subnetworks inside a NN. Three of the simplest layer architectures are *feedforward* layers (also known as *dense* layers), convolutional layers, and residual layers. Since they will be of use in our machine-learning workflow, we will discuss their exact structure.

- In the simplest feedforward network, such as the one illustrated in Figure 3.1a, all layers are linearly connected with an additional activation function, leading to a model of the form

$$\begin{aligned} X &= \mathbf{l}_0, \\ \mathbf{l}_i &= \sigma_i(\mathbf{W}_i \mathbf{l}_{i-1} + \mathbf{b}_i) \quad \forall i \in [1, N], \\ Y &= \mathbf{l}_N, \end{aligned} \quad (3.8)$$

where  $\mathbf{l}_i$  are the layers,  $\mathbf{W}_i$  the weights,  $\mathbf{b}_i$  the biases,  $\sigma_i$  the activation functions and  $N$  the number of layers.

- Convolutional layers are especially useful in signal processing and computer vision problems. They incorporate multiple convolution operations on the input array. The parameters of the layers define the exact way the convolution is performed. Consider for illustration purposes the case of an input 2D array of size  $(N, N)$ . The convolutional layer is internally parametrized by a kernel  $\omega$  of shape  $(m, m)$

such that the input  $X$  to the layer is transformed as

$$Y_{i,j} = \sum_{a=0}^{m-1} \sum_{b=0}^{m-1} \omega_{ab} X_{i+a, j+b}. \quad (3.9)$$

The output size will be  $(N-m+1, N-m+1)$ . Lastly, a user-specified non-linearity is applied. The implementation of convolutional layers in machine learning APIs is usually done by specifying a kernel size and a set of auxiliary parameters. For instance, a single layer can have multiple independent kernels, can apply padding to the input array before convolving, etc.

- Residual layers implement a skipping connection within another layer, typically a convolutional one. A skipping connection adds the input tensor to the output tensor:

$$Y = T(X) + X, \quad (3.10)$$

where  $T$  is the other neural layer. A relevant property, both from the theoretical and practical viewpoints, is that the derivative of the output tensor  $Y$  with respect to  $X$  always includes an identity term that tends to prevent it from being zero. This allows the information to flow easily in deep architectures, speeding up training and limiting overfitting [65].

- Batch-normalisation layers [66] address the training difficulty encountered when the input tensors vary significantly from one sample to another. These differences cause different network weights to be adjusted simultaneously in opposite directions, which ultimately impairs training. Batch-normalisation layers simply aim at the normalisation of each tensor input feature when we feed a batch of samples to a network. A batch-normalisation layer has 2 internal parameters  $\gamma, \beta$  for each input feature, that are applied as a linear transformation after normalisation. If we consider an input feature  $x$  (that is, a component of  $X$ ), and a batch of samples

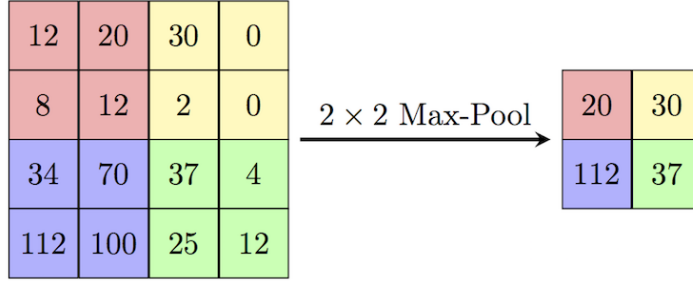


Figure 3.7: Max pooling operation with kernel size (2, 2).

$\{x_1, \dots, x_m\}$ , then a batch-normalisation layer is implemented as:

$$\begin{aligned}\mu &= \frac{1}{m} \sum_{i=1}^m x_i \\ \sigma^2 &= \frac{1}{m} \sum_{i=1}^m (x_i - \mu)^2 \\ \hat{x}_i &= \frac{x_i - \mu}{\sqrt{\sigma^2}} \\ \mathbf{BN}_{\gamma, \beta}(x_i) &\equiv \gamma \hat{x}_i + \beta\end{aligned}\tag{3.11}$$

- Max pooling layers (Figure 3.7) are usually added after convolutional layers to downsample, add translational invariance and hence make the network more robust against the presence of features in different spatial positions. Similar to a convolution, max pooling is done by sliding a kernel window onto the input array, but now we select the maximum value within the window.

### 3.2.3 Prediction uncertainty and Bayesian models

In classical supervised deep learning, a neural network with weights  $\theta$  is trained on some dataset  $\mathcal{D}$  to produce a minimal cost estimator  $\hat{\theta}$  for a predefined loss function. From the statistical point of view, this is a point estimate for each one of the network parameters. Point-estimate networks might lack explainability and generalise in overconfident ways to unseen data, and there is no obvious mechanism for such models to express their ignorance in such cases.

This is an analogous situation to classical parameter inference in statistics. From this perspective, the *frequentist* approach to parameter estimation can be compared to point-estimate networks. However, *Bayesian* statistics [67] has flourished in the last

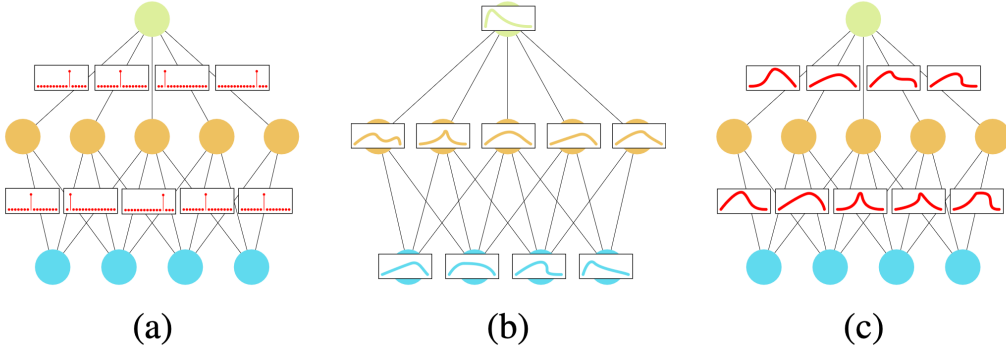


Figure 3.8: Illustration for a non-stochastic neural network a), a network with stochastic activations b), and a network with stochastic weights in c). Source: [68].

decades and is becoming the dominant statistical framework for data analysis inference problems. In the Bayesian paradigm, parameters are treated as random variables to reflect our ignorance about their “true” values. Our prior beliefs about the parameters  $\theta$  are then updated in the presence of new data  $\mathcal{D}$  using Bayes’ theorem:

$$P(H|D) \propto P(D|H)P(H), \quad (3.12)$$

where  $H$  is a certain hypothesis about  $\theta$ ,  $P(D|H)$  is known as the *likelihood* and encodes the relation between the data generation and the parameters, and  $P(H)$  reflects our prior beliefs. Bayesian frameworks have two main advantages. Firstly, they allow us to make our assumptions explicit by setting up the prior  $P(H)$ . This allows us to clarify, discuss and criticize prior knowledge in a clear way. Secondly, they provide a natural approach to quantify uncertainties in the inference parameters.

Bayesian neural networks are models that incorporate stochastic elements and that are trained using Bayesian inference techniques [68]. This is generally implemented either by considering stochastic weights in the network or by considering stochastic activations, see Figure 3.8.

A Bayesian neural network is defined by a prior distribution over the weights (when they are set to be stochastic), a functional model that forwards the inputs and generates the outputs, and a likelihood model that defines the predictive power of the network  $p(y|x, \theta)$ . The model weights are updated in the presence of data  $\mathcal{D}$  according to Bayes’ formula

$$p(\theta|\mathcal{D}) \propto p(\mathcal{D}_y|\mathcal{D}_x, \theta)p(\theta) \quad (3.13)$$

When the model has seen the data, we can use the posterior distribution on the parameters to generate data or make a prediction:

$$p(y|x, \mathcal{D}) = \int_{\theta} p(y|x, \theta)p(\theta|\mathcal{D}). \quad (3.14)$$

Note that Equation 3.14 weights the predictions by each possible parametrization of the network using the posterior distribution on the weights. In that sense, Bayesian networks can be understood as training an ensemble of networks and then averaging their predictions. Note that ensembles are also a popular technique with classical neural networks [69]. In fact, since the training of a classical network has also stochastic components (the initial weights, shuffling of the data, ...), it is common to train multiple networks with different initialization seeds and weight their predictions, which tends to outperform even the best-performing network.

Let us illustrate how a committee of networks can outperform even a top-performer network. Suppose we train 3 independent networks  $A, B, C$  for a classification task with two classes, and that they all have the same error probability  $p$ . In an exercise of pure democracy<sup>5</sup>, consider a classifier  $D$  who picks the class with the majority of votes. Since  $D$  is wrong if and only if at most one of the classifiers is wrong, the probability of error for  $D$  is (considering  $p \rightarrow 0$ )

$$p^3 - 3(1-p)^2 = \mathcal{O}(p^2),$$

and hence  $D$  outperforms  $A, B$  and  $C$ .

### 3.2.4 Hyperparameter selection

The performance and convergence properties of a deep learning model are highly sensitive to its precise architecture, and hence, to the *hyperparameters* that control the latter: number of layers, the exact type of layers (convolutional, dense,...) and other auxiliary parameters that influence the training process. The optimal set of hyperparameters is the one that produces the best-performing model on unseen data. There are three main difficulties when choosing hyperparameters. Firstly, it is not obvious a priori how modifying a certain parameter will affect the performance of a model. For example, if we add an extra layer to a network, will that improve expressivity and performance or will it lead to overfitting? This is a consequence of the low interpretability of deep learning

---

<sup>5</sup>“I love democracy. I love the Republic”, Senator Palpatine.

models. Secondly, evaluating the performance of a model requires training it, which is computationally expensive. Finally, there are potentially an infinite number of possible architectures to explore.

Many Python APIs implementing routines to find optimal hyperparameters exist. They include state-of-the-art algorithms for exploring the hyperparameter space, selecting which parameters to explore, and early-stopping the evaluation of unpromising trials. In this work, we use `OPTUNA` [70], which is a Python optimisation API, to select the appropriate set of hyperparameters for our deep learning models. `OPTUNA` implements a wide variety of searching algorithms to explore the hyperparameter space. Among those strategies, we can choose a naive grid search, where the user defines a grid over the hyperparameter space, and all possible combinations are tested and ranked in a sequential order. `OPTUNA` can also implement a random search, which randomly selects the next trial over a grid. However, `OPTUNA` also implements more complex searching algorithms. The default search strategy is the *Tree-structured Parzen Estimator* (TPE) approach. TPE is designed to maximise the expected improvement when selecting a new sample. If we have already explored a set of points  $x$ , the expected improvement (EI) for a new trial  $y^*$  is defined as

$$\text{EI}_{y^*}(x) = \int_{-\infty}^{y^*} (y^* - y)p(y|x)dy = \int_{-\infty}^{y^*} (y^* - y)p(x|y)\frac{p(y)}{p(x)}dy , \quad (3.15)$$

where we are assuming a one-dimensional problem for clarity, and  $p(y|x)$  represents the probability of choosing a trial  $y$  having observed  $x$ , as obtained from the searching algorithm. TPE optimises equation (3.15) by using the following routine [71]:

1. We initiate a set  $\mathcal{D}$  of explored trials with  $N_i$  parameters and compute their performance.
2.  $\mathcal{D}$  is split as  $\mathcal{D} = \mathcal{D}^l \cup \mathcal{D}^g$  in the top  $\gamma$  performers (a common value is  $\gamma = 0.2$ )  $\mathcal{D}^l$  and the lower performers  $\mathcal{D}^g$ .
3. We fit a two Gaussian mixture distributions to  $\mathcal{D}^l$ ,  $l(x)$  and to  $\mathcal{D}^g$ ,  $g(x)$ . This is a Kernel Density Estimation (KDE) for the distribution of both sets. See Figure 3.9 for an illustration of this step.
4. The new trial parameters are selected and added to  $\mathcal{D}$  to maximise  $l(x)/g(x)$ . In practice, this can be done by generating  $N_s$  samples from  $l(x)$  and then maximising  $l(x)/g(x)$  over those samples.

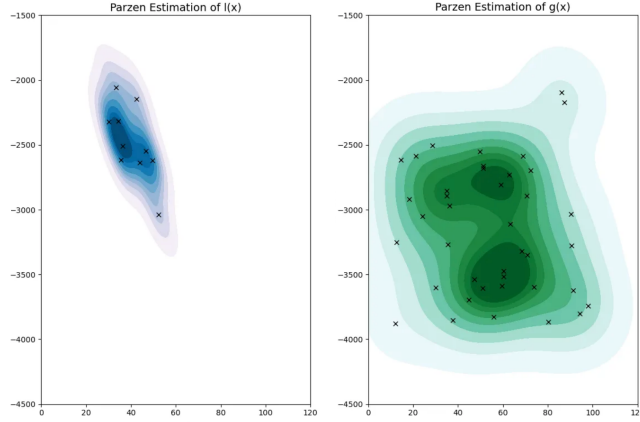


Figure 3.9: Example KDE estimation for the distribution  $l(x)$  and  $g(x)$  used in the TPE algorithm.

We can easily show that the TPE routine maximizes the expected improvement Equation 3.15. Firstly, note that  $\gamma = p(y < y^*)$  and that  $p(x) = \int p(x|y)p(y)dy = \gamma l(x) + (1 - \gamma)g(x)$ . Furthermore, if  $y < y^*$ , we have that  $p(y|x) = l(x)$ , and hence,

$$\int_{-\infty}^{y^*} (y^* - y)p(x|y)p(y)dy = \ell(x) \int_{-\infty}^{y^*} (y^* - y)p(y)dy = \gamma y^* \ell(x) - \ell(x) \int_{-\infty}^{y^*} p(y)dy. \quad (3.16)$$

We conclude that

$$EI_{y^*}(x) \propto \left( \gamma + \frac{g(x)}{\ell(x)}(1 - \gamma) \right)^{-1}, \quad (3.17)$$

and so we need to maximise  $l(x)/g(x)$ , as previously discussed.

### 3.2.5 Loss function and training

In this section, we further detail the training process of a deep learning model, and describe the algorithms that will be used to train our model. As we have already discussed in Section 3.2.1, the goal of our model is to minimise the generalisation error:

$$\varepsilon = \mathbb{E}_F[\mathcal{L}(Y, \hat{f}(X|\mathcal{D}_T))]. \quad (3.18)$$

The loss function  $\mathcal{L}$  should be chosen to encourage the model to produce realistic outputs. For regression, where the goal is to estimate an output tensor  $Y$  from an input  $X$ , typical choices include the usual Euclidean norm or the absolute difference:

$$\mathcal{L}(Y, \hat{Y}) = \sum_i |\hat{Y}_i - Y_i|^p, p = 1, 2, \quad (3.19)$$

where  $\hat{Y}$  is the model prediction. This choice of loss function is minimised when the model correctly predicts the target tensor. An important piece of information to note is that Equation 3.5 is generally unknown, since we don't have access to all the possible realizations of the data, but only to a limited training dataset. As a consequence, we typically minimise the loss function computed on small samples of the training data, called *batches*, by averaging the loss over all samples in the batch. Observe that then, computing the average loss over a large batch will yield a closer approximation to the true loss function. The training process then uses these estimations of the loss to update the network parameters,  $\theta$ , using techniques that involve the computation of the loss gradient. This process is normally repeated multiple times over the training dataset. Each time the model sees the whole dataset is known as an *epoch*. A training loop with  $N_e$  epochs and batches of size  $B_s$ , with  $N_b$  batches, can then be written as:

---

**Algorithm 1** Classical deep learning training loop

```

while epoch <  $N_e$  do
    while batch <  $N_b$  do
        Loss  $\leftarrow \frac{1}{B_s} \sum_i \mathcal{L}(\hat{Y}_i, Y_i)$ 
        Compute  $\nabla_{\theta}(\text{Loss})$ 
        Update  $\theta \leftarrow \theta(\nabla_{\theta}(\text{Loss}))$ 
        epoch  $\leftarrow$  epoch+1
        batch  $\leftarrow$  batch+1
    end while
end while

```

---

In Algorithm 1 there are two main steps we have not specified. Firstly, the computation of  $\nabla_{\theta}(\text{Loss})$ . This is trivial from the mathematical viewpoint, but it is not trivial to implement<sup>6</sup>. Most APIs implement a *backpropagation* algorithm for this step that we will not discuss here<sup>7</sup>. The second key aspect of a training loop is using the gradient  $\nabla_{\theta}(\text{Loss})$  to update  $\theta$ . This step in Algorithm 1 was represented by  $\theta \leftarrow \theta(\nabla_{\theta}(\text{Loss}))$ . The precise way of using the calculated loss gradients to update the weights defines the *optimiser*<sup>8</sup>. A naive way to optimise the loss at each iteration is to use the most straightforward implementation of *gradient descent*, where the parameters are updated

---

<sup>6</sup>Note that this is purely a computer science problem.

<sup>7</sup><https://www.tensorflow.org/guide/autodiff>

<sup>8</sup>Note that this is purely a mathematical problem in optimisation.

using

$$\theta \leftarrow \theta - \alpha \nabla_{\theta}(\mathcal{L}), \quad (3.20)$$

where  $\alpha$  is a constant known as the *learning rate*. In general, optimising the loss function  $\mathcal{L}$  corresponds to optimising a complex (perhaps non-convex) function on a highly multidimensional space, with millions or billions of parameters. As a consequence, naive gradient descent might not be the best-performing optimiser. Additionally, recall that the loss  $\mathcal{L}$  calculated for every batch is just an approximation of the global loss in Equation 3.5. The batch size determines how accurate the computed gradient is. Calculating the loss over all possible data points would yield the exact gradient. On the opposite extreme, calculating the gradient on a single data point would generate a biased gradient, and lead to a noisy gradient descent. The loss function can also have a complex structure. In the literature, a multitude of optimisers that improve and generalise the naive gradient descent exist. In this work, we use *Adam* [50]. Adam is a first-order momentum-based optimiser. Adam uses a recursive update of the first and second moment of the gradient to update the learnable parameters. The Adam algorithm reads as follows:

---

**Algorithm 2** Adam optimiser

---

**Require:**  $\alpha$ : Learning rate  
**Require:**  $\beta_1, \beta_2$ : Moment decay rates  
**Require:**  $f(\theta)$ : Target function  
**Require:**  $\theta_0$ : Initial parameters  
**Require:**  $\varepsilon$ : Numerical tolerance constant

$m_0 \leftarrow 0$ : Initialize first moment  
 $v_0 \leftarrow 0$ : Initialize second moment  
 $t \leftarrow 0$ : Initialize time

**while**  $\theta_t$  not converged **do**

- $t \leftarrow t + 1$
- $g_t \leftarrow \nabla_{\theta} f(\theta_{t_1})$ : Get gradient
- $m_t \leftarrow \beta_1 m_{t-1} + (1 - \beta_1) g_t$ : Update first moment
- $v_t \leftarrow \beta_2 v_{t-1} + (1 - \beta_2) g_t^2$ : Update second moment
- $m_t \leftarrow m_t / (1 - \beta_1^t)$ : Correct first moment bias
- $v_t \leftarrow v_t / (1 - \beta_2^t)$ : Correct second moment bias
- $\theta_t \leftarrow \theta_{t-1} - \alpha m_t / (\sqrt{v_t} + \varepsilon)$ : Update parameters

**end while**

---

Adam differs in two key features with respect to the naive gradient descent. Firstly, it includes two decay constants  $\beta_1$  and  $\beta_2$  used to include information about the past state of the optimisation into the next current step. Since typical values are  $\beta \sim 0.9$ ,

recent gradient values contribute more to the current step update than older ones, but the inclusion of a momentum term allows the optimisation to potentially escape local minima. Secondly, Adam includes a term  $v_t$  to account for the second moment in the gradient estimation. The running averages in Adam can potentially help to navigate noise functions by smoothing the local gradient.

Most current deep learning implementations are deployed or trained using HPC infrastructure. This becomes a necessity when training on large datasets. A quickly deployable way of parallelised training, which requires minimal code modification is known as *Synchronous Distributed Training*. Synchronous Distributed Learning aims to harvest the computational power of multiple machines (GPUs,...) in the training stage by having different workers perform parallel calculations in a single batch. This can be done, for instance, by splitting the batch and sending each part to a different worker. In this work, we use the TensorFlow implementation `tf.distribute.MirroredStrategy`. This training strategy mirrors the model and its parameters in every worker (for instance, in every GPU), slices the training batch and distributes them across all workers. Each worker then calculates the loss and gradient in the corresponding batch slices. The gradient is then aggregated before updating the parameters and moving on to the next batch.

### 3.3 Workflow implementation: Recovering IGM conditions from the Lyman-alpha forest

This section describes the deep learning implementation used in this work and builds on the ideas that have already been introduced regarding machine learning. The code used is largely based on [27] with some modifications and is available at <https://github.com/nicenustian/bh2igm> and based on TensorFlow and TensorFlow Probability.

The ultimate aim is to use a Bayesian neural network to recover the IGM gas density from an input Lyman- $\alpha$  skewer. Note that this is essentially equivalent to invert Equation 1.35, which describes the Lyman- $\alpha$  opacity as a function of the IGM gas conditions. As we have already discussed in Section 2.3, we will work in the optical depth-weighted space. This avoids two main potential difficulties in the analysis. Firstly, by working in this new space, the network will not have to learn the relation between peculiar velocities and the Lyman- $\alpha$  opacity, which simplifies both the architecture design and learning phase. Secondly, it breaks the degeneracy introduced by peculiar velocities, since a shift in the physical space can produce the same opacity as a shift in the velocity space.

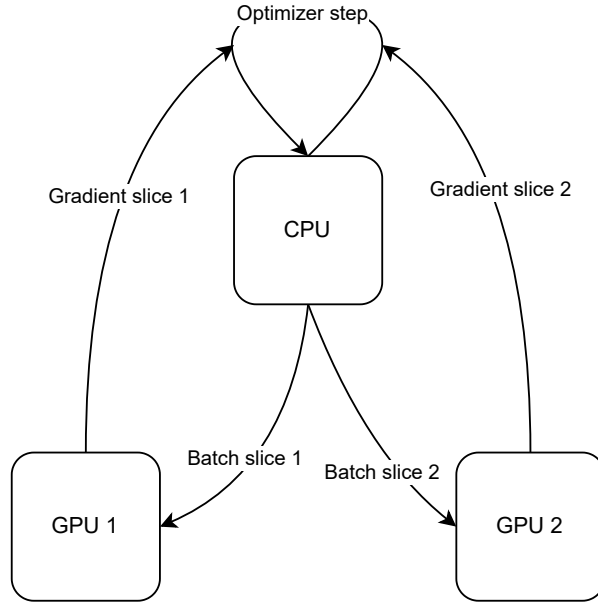


Figure 3.10: Distributed mirrored learning strategy with two workers (GPUs) and a CPU aggregating the gradient and updating the model parameters.

We specify the architecture design by the hyper-parameter list found in Table 3.1. The global architecture that describes the number and size of the layers is specified by two hyper-parameters. Firstly, the parameter “Layers per block” is an integer list whose size is the number of blocks in the network and whose elements are the number of layers in each block. Secondly, the parameter “Filters per block” is also an integer list that specifies the number of convolutional filters of the layers for each block. If the architecture is a simple MLP, this parameter does not have any effect. The layers are chosen among a simple densely connected layer (MLP), and convolutional layer (ConvNet) or a residual layer (ResNet). Every feedforward pass through a convolutional or densely connected layer is followed by a batch normalisation layer and by an activation function, see Section 3.2.2. We use the PReLU activation function, which is a generalisation of the ReLU activation with a learnable weight  $\alpha$  such that:

$$\text{PReLU}(x; \alpha) = \begin{cases} \alpha x & , x < 0 \\ x & , x \geq 0 \end{cases} \quad (3.21)$$

We append the same final block to all three potential architectures, which consists of a

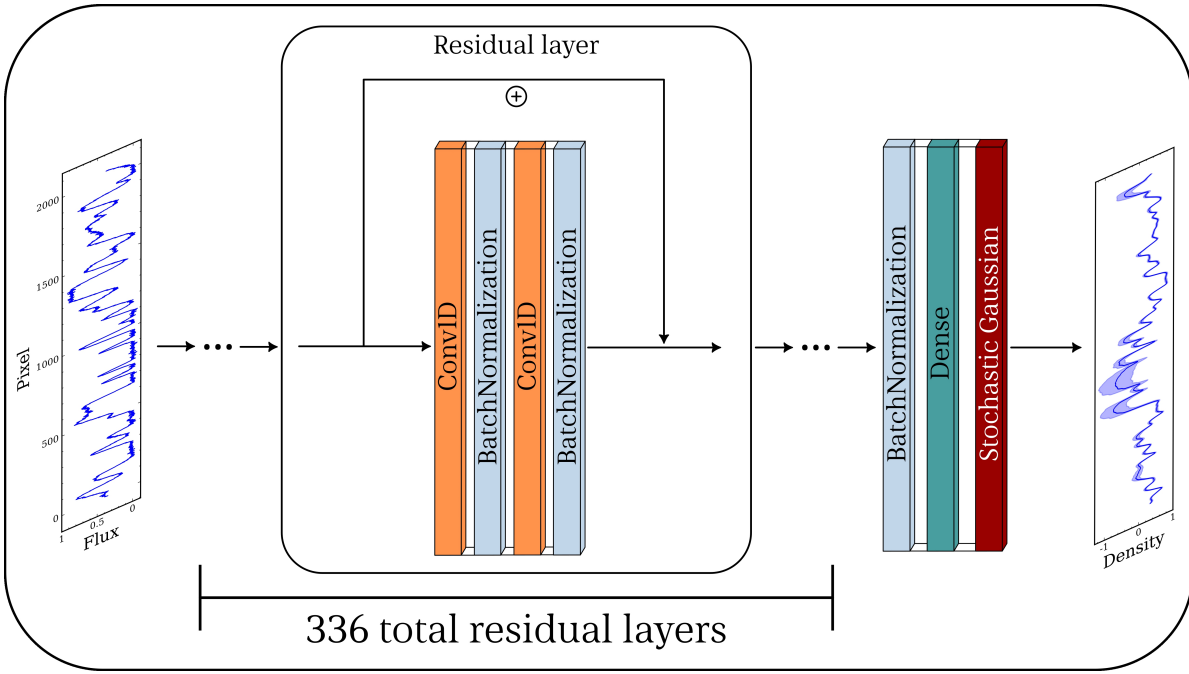


Figure 3.11: Fiducial architecture for our Bayesian neural network trained at  $z = 4.4$  on the Sherwood simulation suite. The fiducial parameters can be found in Table 3.1.

flattening layer transforming the tensor being manipulated to a one-dimensional vector, a dense layer and finally a Gaussian probabilistic layer. This final block includes the stochastic components of the neural network (hence the name Bayesian). For each target output density pixel, the Gaussian layer outputs a full Gaussian probability distribution parametrised by the expected density and the standard deviation. This standard deviation will later be used as the estimation for the epistemic uncertainty in the network prediction. We illustrate the fiducial architecture in Figure 3.11.

We optimise the network hyper-parameters using OPTUNA as discussed in section 3.2.4. Table 3.1 shows the optimised hyper-parameters and the range considered during the grid search. Note that these values can potentially depend on the nature of the training dataset, and hence may vary with redshift. In Table 3.1 we present the fiducial architecture at  $z = 4.4$ . This optimisation process is automatically carried out whenever the redshift is varied.

For each redshift, we train a different network using the Sherwood simulation suite presented in Section 2. Recall that we consider two training datasets, **SHERWOOD** and **SHERWOOD THERMAL**, where the latter includes variations in the thermal parameters and reionisation history. See [26] for more details. The inclusion of thermal parameters

Hyper-parameter	Min.	Max.	Best value
Layers per block (int)	1	4	[1, 2, 4 ,4]
$\log_2(\text{Filters per block})$ (int)	1	5	[4, 5, 5, 5]
Number of blocks (int)	1	4	4
$\log_2(\text{Batch size})$ (int)	3	8	3
Learning rate ( $\log_s$ , float)	$10^{-4}$	0.1	0.004937
Network (MLP, ConvNet, ResNet)	...	...	ResNet

Table 3.1: Hyper-parameter grid search for the fiducial model at  $z = 4.4$ . “ $\log_s$ ” indicates the parameter is sampled in the log domain. “Int” and “float” mean they are sampled as integers or floats, respectively.

will lead to a more robust network when used on unseen real data, but its performance will naturally be lower than the network trained on a single thermal history. We use **SHERWOOD** for an initial model testing and **SHERWOOD THERMAL** for our final analysis of real data. 80 % of the data is used for training, and the rest is used for validation purposes. For reference, the training dataset **SHERWOOD** with 7 different WDM models has a total size of  $\sim 3.5$  GB. We use the Raven<sup>9</sup> HPC cluster at the Max Planck Computing and Data Facility to train our networks. With 4 Nvidia A100 GPUs, a typical training time is  $\sim 1$  hour, depending on the model’s exact architecture and number of parameters.

The network’s input consists of a Lyman- $\alpha$  flux skewer, and the network’s output consists of the mean density and standard deviation at each pixel. The labelled training data consists of individual Lyman- $\alpha$  flux skewers with their associated density optical depth-weighted density field,  $(F, \log(\Delta_\tau))$ . For each labelled training pair, the loss function is taken to be the negative log-likelihood (NLL) for the normal distribution that the network parametrises:

$$-\log \mathcal{L} = \frac{1}{N} \sum_i \left( (Y_i - Y_{i,\text{pred.}})^2 / \sigma_{i,\text{pred.}}^2 + \log\left(\frac{1}{\sigma_{i,\text{pred.}}^2}\right) \right), \quad (3.22)$$

where the sum runs over all skewer pixels,  $Y_i$  is the real density at pixel  $i$ ,  $Y_{i,\text{pred.}}$  is the predicted expected density and  $\sigma_{i,\text{pred.}}^2$  the predicted standard deviation.

The input skewers are processed as follows. Firstly, the input flux is rebinned into a target number of pixels to match the real data that will be used. Downsampling is done by taking the average flux over nearby pixels, while upsampling is done by appending to every pixel a copy of itself. The flux is then convolved using a Gaussian kernel to simulate a given instrumental resolution. In most of our analyses, the resolution is

<sup>9</sup><https://www.mpcdf.mpg.de/services/supercomputing/raven>

taken to be 6 km/s, in accordance with state-of-the-art spectrographs, such as UVES [72]. During training, the training data is stacked and randomly shuffled to ensure a correct mixing and representativity of the models. Lastly, we process the re-scaled input optical depth to match the observed mean flux at the considered redshift [41]. The training data is augmented on the fly in two ways. We first roll the input spectra by applying translations, which helps the network learn dynamical features, independently of their positions. We also add random uncorrelated Gaussian noise to simulate a finite signal-to-noise ratio (SNR). The default SNR per pixel used for testing purposes is 50. When applying our methods to real data, the network is retrained using a noise model for each target object.

We use the Adam optimiser with fixed moment decay rates as implemented in the TensorFlow API and a learning rate set by the Optuna grid search. The training is evaluated using two main metrics: the loss function NLL, and the mean absolute error, MAE, defined as the Euclidean norm in Equation 3.19 with  $p = 1$ . To prevent over-fitting, the network parameters are only updated if the NLL loss improves on the validation split of the data. A policy to halve the learning rate if there is no loss improvement in the test set for 10 epochs is also included. This is the most straightforward implementation of an adaptive learning rate. Figure 3.12 shows the evolution of the NLL and the MAE on the validation split during training for our fiducial architecture at  $z = 4.4$  and the **SHERWOOD** suite. It is interesting to note that while the MAE is always positive by definition, the negative values of the NLL are consistent with its definition. Figure 3.12 demonstrates that, for our problem, the network training converges in  $\sim 100 - 150$  epochs. Recall that we always work with  $\log(\Delta_\tau)$ , which also serves as a regularisation step with respect to the density.

In Figure 3.13 we show an example  $20\text{h}^{-1}\text{cMpc}$  Lyman- $\alpha$  validation skewer from the **SHERWOOD** dataset. The top panel shows the input flux to the network. The bottom panel shows the true  $\Delta_\tau$  density fields, the (mean) recovered densities and the  $1\sigma$  envelope predicted by the Bayesian network. Note that, in the spectral regions with large features and variations in the flux, the predicted mean density closely follows the true field. In those regions, there is enough physical information for the network to accurately recover  $\Delta_\tau$ . In contrast, in the saturated regions with low flux, the noise dominates, and the network predicts larger uncertainties (observe, for instance, the saturated region in Figure 3.13 around  $8\text{h}^{-1}\text{cMpc}$ ). This should be regarded as a strength of Bayesian networks since they are able to accurately detect and make explicit situations where the predictions should not be trusted. To minimise the mean error in regions where

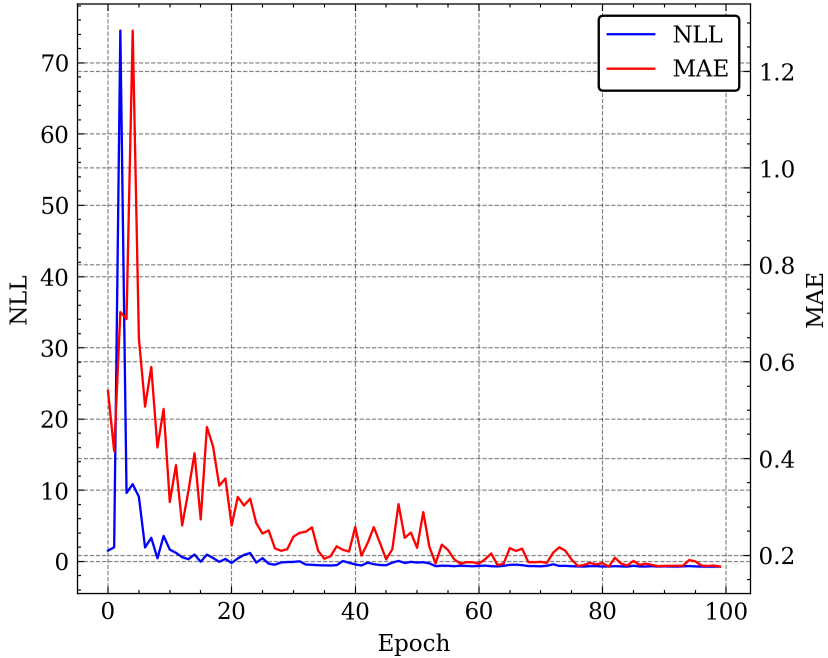


Figure 3.12: Learning curve for our fiducial architecture at  $z = 4.4$  on the **SHERWOOD** dataset. The figure shows the NLL and the MAE on the validation split as a function of the epoch.

the network cannot make accurate predictions, note how there is a bias towards quasi-constant mean prediction. This is visible around  $8\text{h}^{-1}\text{cMpc}$ , where the true density has a steeply increasing profile, and the prediction has an almost constant u-shaped profile.

On the **SHERWOOD** validation split, the network reaches a  $1\sigma$  accuracy of 79%, meaning that 79% of the pixels are correctly predicted within  $1\sigma$ . Note that this is a larger accuracy than expected from purely normally distributed densities.

### 3.4 Recovered field statistics and uncertainties

Once we have the machinery to recover the IGM density from a Lyman- $\alpha$  skewer, we would like to use this density field information to do statistical inference on the physical parameters of interest. In this work, since the WDM mass directly affects the matter distribution of the Universe (see Figure 1.3) we would like to infer the WDM masses from the recovered  $\Delta_\tau$  field. Now, note that the exact  $\Delta_\tau$  field of a skewer, such as the one shown in Figure 3.13, not only depends on a set of physical parameters (WDM mass, temperature,...) but also on the initial conditions or equivalently, the random seed in the simulation. As a consequence, we will not compare densities on a sightline-

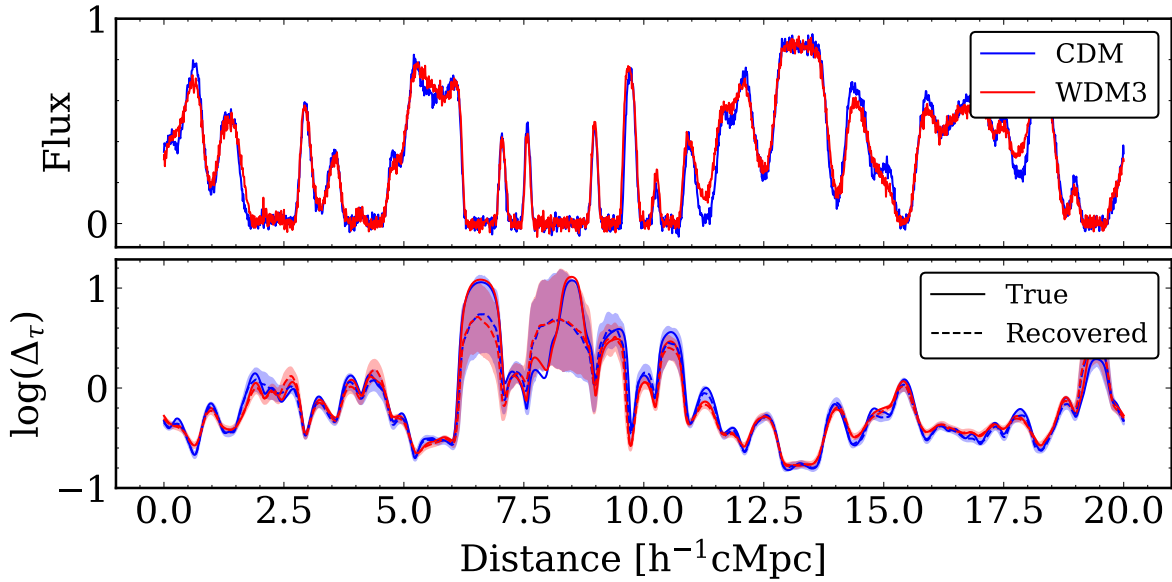


Figure 3.13: An example  $20\text{h}^{-1}\text{cMpc}$  Lyman- $\alpha$  validation skewer for the CDM and WDM3 Sherwood models. The top panel shows the input flux to the network. The bottom panel shows the true  $\Delta_\tau$  density fields, the (mean) recovered densities and the  $1\sigma$  envelope predicted by the Bayesian network.

by-sightline basis, but rather compute and compare aggregated statistics of the fields over multiple realizations that capture global statistical properties, and not simulation-specific characteristics. Statistics that have been amply tested in the literature are the Power Spectrum (PS), the Probability Distribution Function (PDF), the curvature, or the autocorrelation function (see [73] and [74] for more details). In this work, we will focus on the  $\Delta_\tau$  PDF. In section 4.6.4 we will address the optimality of this choice.

We will carefully describe the statistical inference pipeline in Section 4.1 . The main idea will be to fit the density PDF obtained from the Bayesian neural network using observed skewers to the PDFs from each WDM model in the **SHERWOOD** dataset. An important consideration for a successful pipeline will be to compare *apples to apples*, i.e., to compare statistics that have been obtained through the same process to reduce any potential bias. For that reason, we will always work with the ML-recovered density by our fiducial neural network, and compare the *observed* statistics to the *model* statistics from each WDM run. The model statistics are computed over the whole simulation box using all 5000 skewers from each run. The observed statistics are typically computed over a much smaller number of observed sightlines. In this section, we analyse the statistics recovered from the predicted  $\Delta_\tau$  field by the Bayesian network, including how to calculate their uncertainties, which will be crucial for the rest of the inference process.

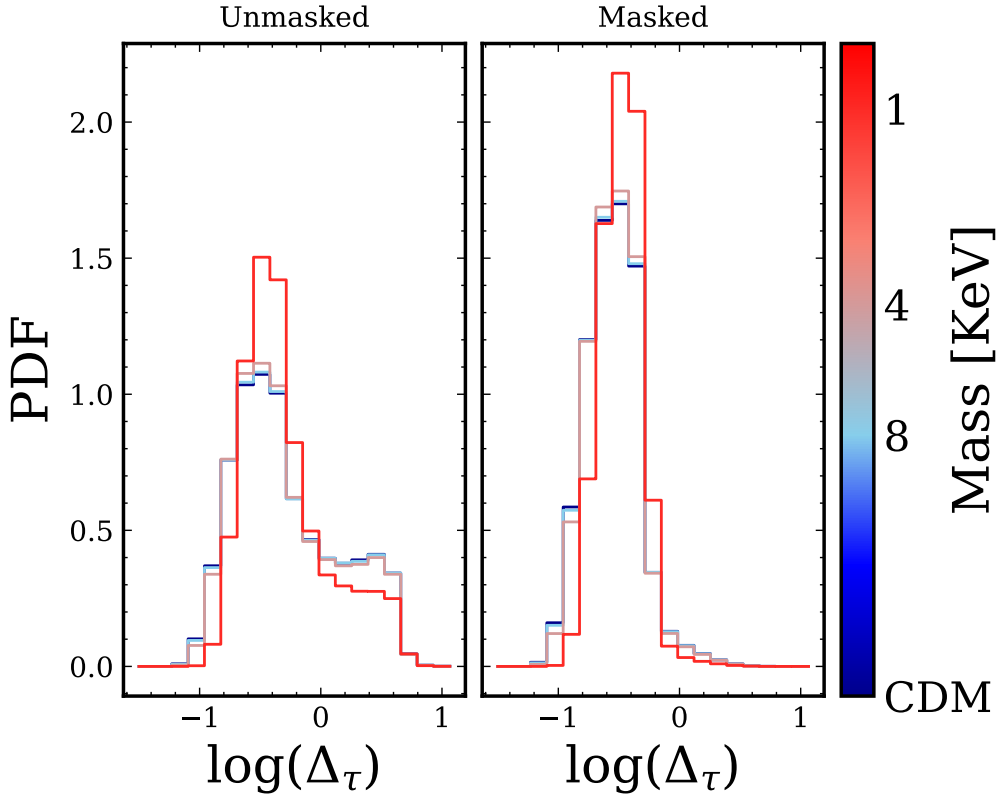


Figure 3.14: Model  $\Delta_\tau$  PDFs for the **SHERWOOD** runs computed using the recovered density by our neural network. We explicitly highlight the effect of masking the saturated regions that have a flux  $\leq 3\frac{1}{\text{SNR}}$ .

### 3.4.1 Noisy regions and masking

Recall Figure 3.13 as the central example in this regression problem. The flux-saturated regions where the flux is close to zero and dominated by noise have no physical information to recover the density. Potentially, any density higher than the truth could also produce a saturated profile. The model correctly detects these regions and produces larger uncertainties, but the mean predictions have no physical information and should not be considered in any posterior analysis. Hence, we will mask these regions when comparing the model and observed  $\Delta_\tau$  PDFs. This has the effect of modifying the shape of the PDF by removing part of the high-density tail. We show in Figure 3.14 the model  $\Delta_\tau$  PDFs for the **SHERWOOD** runs computed using the recovered density by our neural network and explicitly highlight the effect of masking the saturated regions that have a flux  $\leq 3\frac{1}{\text{SNR}}$ . As can be noted, the artefact that occurs at high densities ( $\log(\Delta_\tau) \sim 0.5$ ) disappears when masking. It can be interpreted as a bias introduced in the saturated regions.

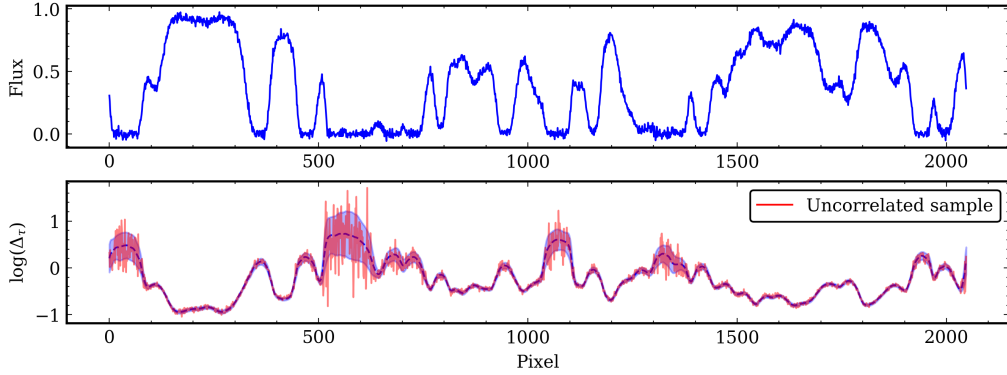


Figure 3.15: An example SHERWOOD CDM skewer, together with the reconstructed  $\Delta_\tau$  in blue. The red field shows a resampling without including covariance between the pixels, which generates random noise.

### 3.4.2 Uncertainty in the recovered statistics

When estimating uncertainties for the recovered PDF, there are two main sources to consider.

#### Sampling from reconstructed density fields

Firstly, the Bayesian ML predictions have a certain uncertainty associated with them, which transfers to the density PDF as an additional scatter. We include such uncertainties by considering the predicted density field  $\Delta_\tau$  and resampling 1000 times the posterior distribution produced by the network. We do this process for every observed skewer, compute the 1000 PDFs for each sample, and then the standard deviation between the 1000 statistics. The resampling process requires careful consideration. If we resample for each Gaussian distribution  $\mathcal{N}(\mu_i, \sigma_i)$  independently at each pixel  $i$ , the resamples are essentially Gaussian noise, as can be seen in Figure 3.15.

To generate adequate resamples, we must include the correlation between pixels and sample from the joint distribution. We estimate such correlation matrices on the prediction residuals in the SHERWOOD suite, defined as:

$$r_i = \frac{\Delta_{\tau,i} - \mu_i}{\sigma_i} \quad (3.23)$$

To generate a smooth correlation matrix for the residuals, we also augment the data by applying 1000 translations to each spectrum. We compute such correlation matrix for the reference SHERWOOD CDM skewers, as shown in Figure 3.16, and will refer to it as  $\Sigma$ . Note that the nearby pixels are correlated for a distance of  $\lesssim 50$ , as the quasi-diagonal

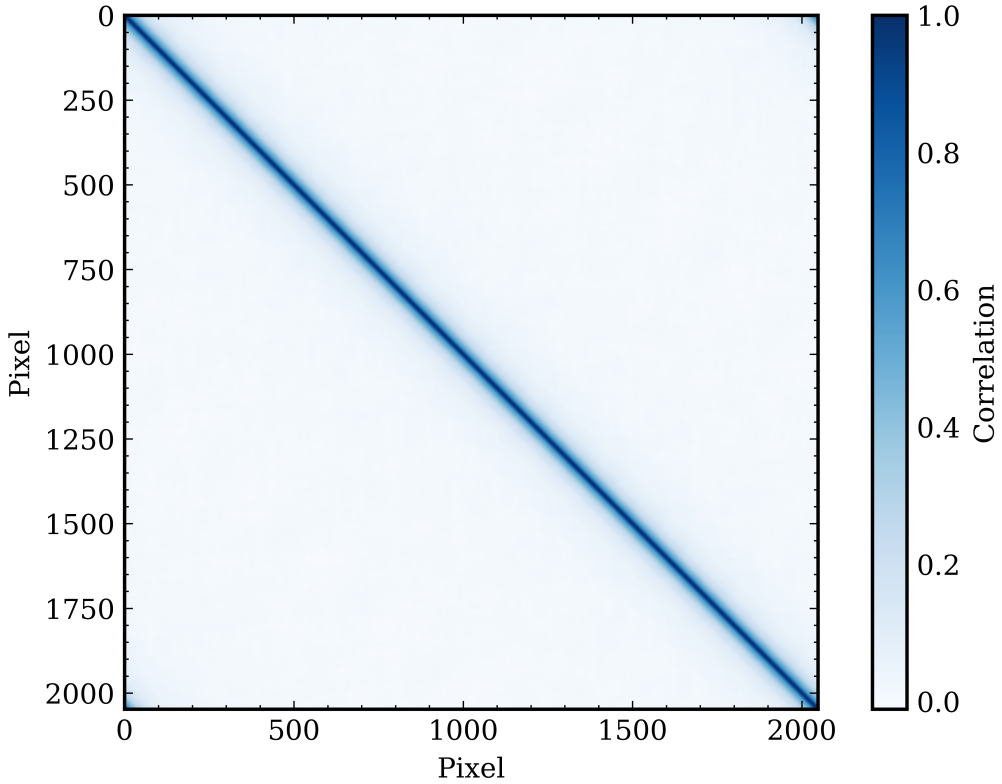


Figure 3.16: The  $\Delta_\tau$  correlation matrix  $\Sigma$  for the prediction SHERWOOD CDM residuals as defined in Equation 3.23 at  $z = 4.4$  for the fiducial trained neural network. Each reconstructed density field has been augmented by applying 1000 translations to generate a smooth matrix.

structure of the matrix suggests. We have computed similar matrices for the rest of the SHERWOOD models, finding very similar results. As a consequence, we use the reference CDM correlation matrix for this resampling step in what follows.

To resample from a reconstructed  $\Delta_\tau$  skewer by our neural network, we draw a sample from the multivariate normal  $\mathcal{N}(0, \Sigma)$ . The reconstructed sample for the density field is then taken to be  $\mu + \sigma\mathcal{N}(0, \Sigma)$ , where  $\mu$  is the vector of mean predictions, and  $\sigma$  the vector of standard deviation predictions. Figure 3.17 shows a series of 100 draws from the same recovered density skewer as Figure 3.15.

### Intrinsic scatter in the recovered PDF

Secondly, we estimate a second contribution to the total uncertainty in the recovered PDF by considering the fact that we have only observed a finite set of skewers, and hence we don't have access to the full  $\Delta_\tau$  field. To estimate this intrinsic scatter, we

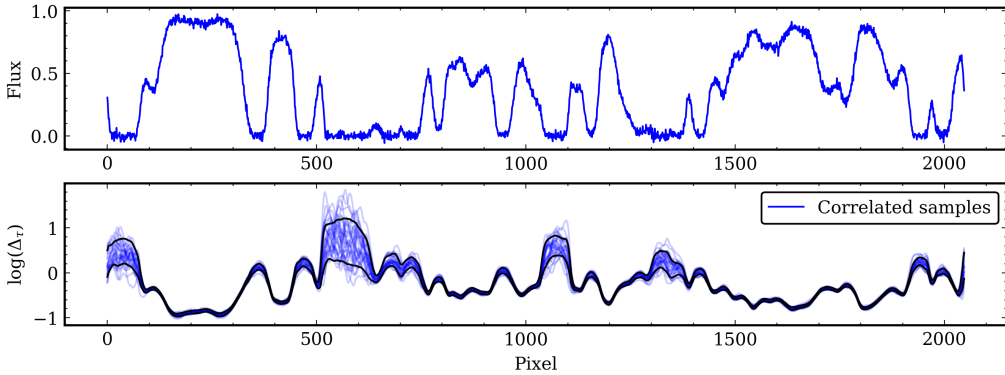


Figure 3.17: A set of 100 draws including the correlation between nearby pixels for a SHERWOOD CDM skewer. As opposed to Figure 3.15, the samples are continuous and no longer show noisy behaviour.

use *bootstrapping* [75]. Bootstrapping approximates the true distribution of the PDF statistic by generating artificial samples from the observed data. Suppose we observed  $N$  sightlines, reconstruct their  $\Delta_\tau$  field and then compute the PDF. To estimate how this PDF depends on the exact observed skewers, we draw  $N$  sightline from the set of observed ones, potentially including repetitions. This might result in repeated sightlines. We then compute the PDF for this new sample. We repeat this process 1000 times and then compute the scatter in the PDF across all 1000 samples.

Bootstrapping approximates the true distribution as  $N \rightarrow \infty$ . It is then reasonable to ask whether this method is accurate when we are only observing a low number of sightlines. To answer this, we note that the  $\Delta_\tau$  PDF is a function of the density value of each of the pixels, which can be considered a random variable depending on the observations. As a consequence, the PDF is itself a random variable and has a probability distribution. We would like to estimate this probability distribution and verify whether bootstrapping provides a reasonable estimate.

To estimate the distribution of the PDF, let us assume that we observe a total of  $N$  pixels, which we will consider as independent for now. Suppose that the  $\Delta_\tau$  distribution for each density pixel is  $f$ . We want to estimate the probability distribution  $p(\lambda|f(x), N)$  that a bin of the PDF has a value  $\lambda$ , conditional on observing  $N$  pixels and a true probability for a density  $x$  of  $f(x)$ . Let us denote by  $X_i$  the  $N$  pixel values that are considered random variables to be observed and start by noting that, by definition,

$$\text{PDF}(x) \propto \sum_{i=1}^N \mathbb{1}_{\{X_i=x\}} \quad (3.24)$$

$$\implies P(\text{PDF}(x) = \lambda) = P(\{\text{Number of } X_i \text{ equal to } x\} = N\lambda) \quad (3.25)$$

$$= \binom{N}{N\lambda} f(x)^{N\lambda} (1 - f(x))^{N-N\lambda} \quad (3.26)$$

We have shown that the probability distribution of the PDF statistic is:

$$p(\lambda|f(x), N) \propto \frac{\Gamma(N+1)}{\Gamma(N\lambda+1)\Gamma(N-N\lambda+1)} f(x)^{N\lambda} (1-f(x))^{N(1-\lambda)} \quad (3.27)$$

Interestingly, and in agreement with bootstrapping, the distribution in Equation 3.27 has a mean that converges to  $f(x)$  as  $N \rightarrow \infty$  and a variance that converges to 0 as  $N \rightarrow \infty$ . To compare how this exact distribution differs from the uncertainties estimated using bootstrapping, we show in Figure 3.18 the uncertainties on the  $\Delta_\tau$  PDF estimated using bootstrapping with 1000 samples and using the standard deviation in Equation 3.27. We show the results for 6 CDM skewers with 2048 pixels each. Both uncertainties are comparable, with bootstrapping slightly underestimating the standard deviation of Equation 3.27. However, bootstrapping includes the correlation between nearby bins, which has not been taken into account when deriving Equation 3.27. For those two reasons, we will consider the bootstrapping uncertainties in what follows when estimating the intrinsic scatter of the recovered PDF.

Finally, the total uncertainties on the observed  $\Delta_\tau$  PDF are obtained by adding in quadrature the machine learning uncertainties and the intrinsic scatter using bootstrapping.

To illustrate the process of recovering the PDF statistic including all the uncertainties mentioned above, we select 60 **SHERWOOD** CDM skewers at  $z = 4.4$  from the validation set as our “observed” data. In Figure 3.19 we compare the  $\Delta_\tau$  PDF computed over the full simulation box (that is, using all skewers) to the PDF computed using the 60 observed skewers. Keep in mind that we always used the  $\Delta_\tau$  fields reconstructed by the fiducial neural network and mask the flux-saturated regions. We find that 60 skewers from the same dataset are sufficient to accurately recover the PDF statistic.

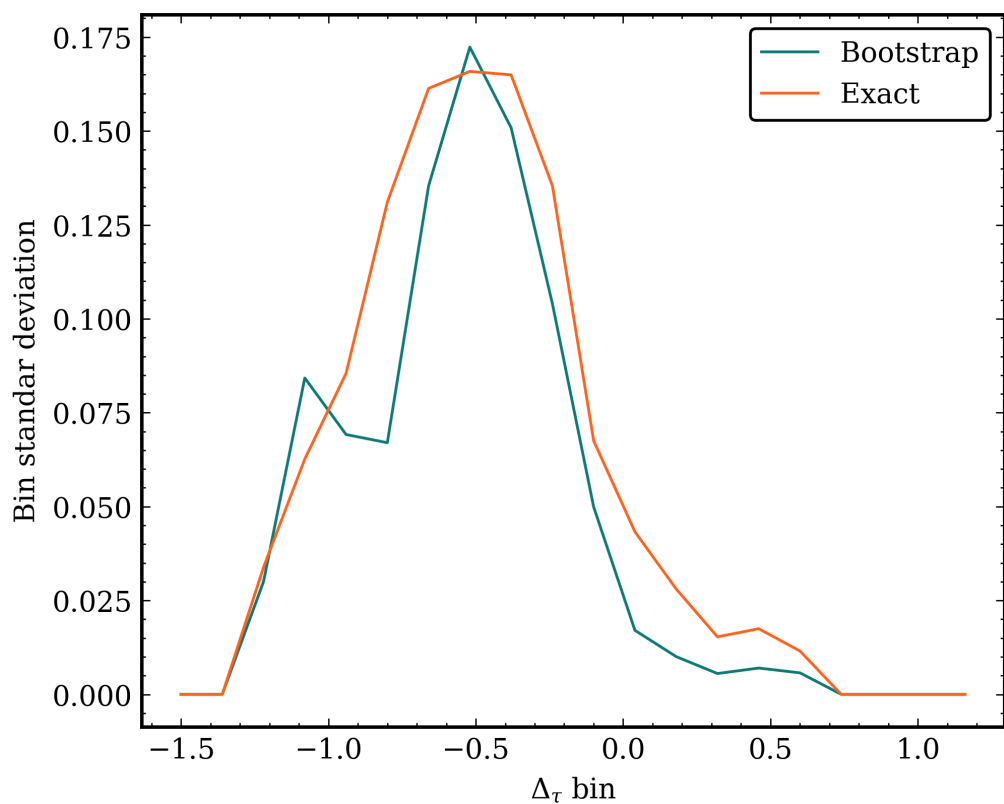


Figure 3.18

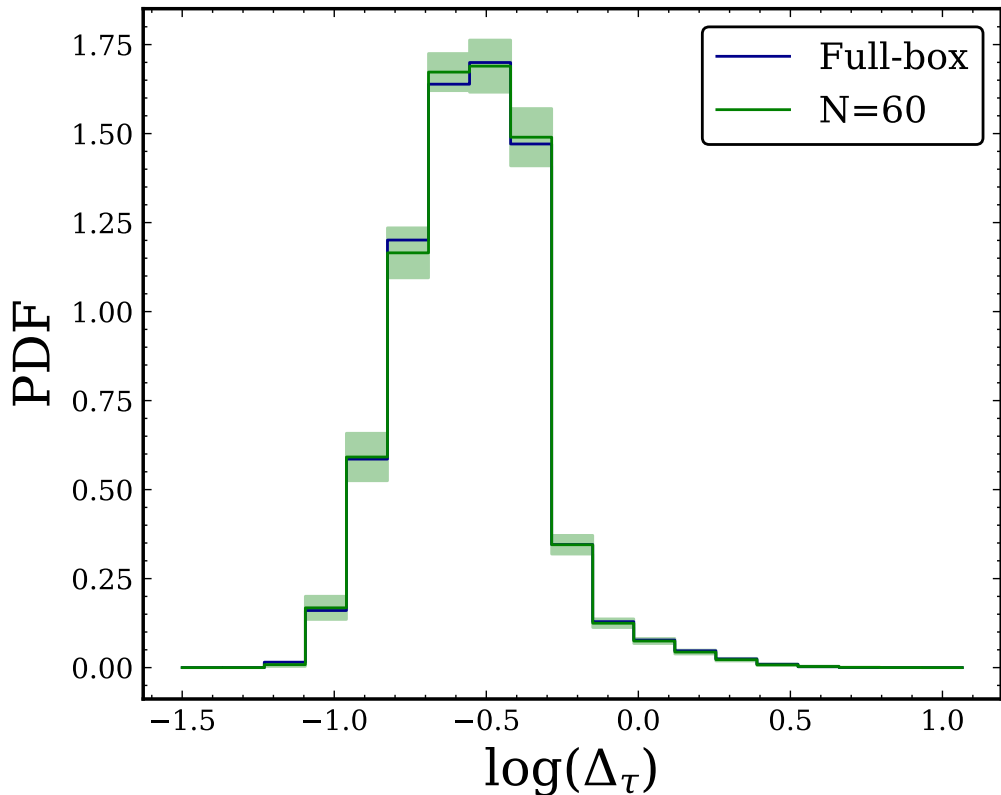


Figure 3.19:  $\Delta_\tau$  PDF computed over the full simulation box (that is, using all skewers) compared to the PDF computed using the 60 observed skewers in the SHERWOOD CDM run at  $z = 4.4$ . We have used the  $\Delta_\tau$  fields reconstructed by the fiducial neural network and masked the flux-saturated regions. We find that 60 skewers from the same dataset are sufficient to accurately recover the PDF statistic.

## 3.5 Model interpretability and limitations

Deep learning models tend to have, by definition, numerous parameters. As a consequence, giving an interpretation for individual model parameters is far from being a trivial task. On top of a large number of parameters, the nonlinearities and the potentially biased and incomplete datasets can lead to complex training behaviours. In that regard, deep learning models have classically been regarded as “black-box” models. They are often more accurate than simpler statistical models but lack explainability. Great efforts have been recently made in understanding the learning dynamics of neural networks [76], [77], [78]. Due to the complexity of this interpretation task, here we choose to only give a qualitative analysis of some aspects that can help gain intuition on how the network operates internally.

### 3.5.1 Saliency analysis

Although many open-source libraries, such as *Captum*<sup>10</sup>, implement popular methods for deep learning model visualization and interpretation, in this work, we use TensorFlow’s built-in differentiation capabilities. In particular, we use Automatic Differentiation to compute the *saliency* score of the model, defined as the gradient of the model output with respect to the model input. As a consequence, for every target density pixel, the saliency score measures which flux pixel variation contributes the most to a change in density. Saliency is a simple score that gives us insights into how the model uses flux to reconstruct densities. Additionally, note that calculating such gradients does not require any numerical finite difference approximation, since TensorFlow’s `GradientTape` class can build an exact computational graph with all the operations performed on the input flux. Saliency maps are a popular technique in applied science to explore deep learning models. In fact, in many physics research articles, it tends to be the only tool used for this purpose. This highlights the need to develop more robust and easily deployable frameworks for deep learning models.

The saliency at density pixel  $i$  and input flux pixel  $j$  is simply

$$\text{Saliency}(i, j) = \frac{\partial \mu_i}{\partial f_j}. \quad (3.28)$$

Figure 3.20 shows the saliency profile averaged over all output density pixels. This gives a global average metric on the relevant flux pixels to predict the density at a certain

---

<sup>10</sup><https://github.com/pytorch/captum>

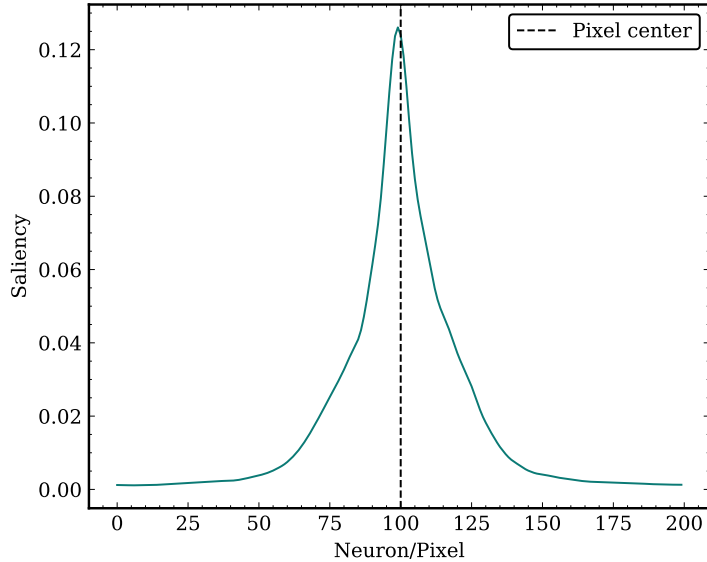


Figure 3.20: Saliency of the CDM and WDM3 Sherwood network at  $8\text{h}^{-1}\text{cMpc}$  Lyman- $\alpha$  flux.

pixel. The typical saliency “length”, that is, the typical number of pixels from the pixel centre that are useful to predict its density is  $\sim 30$ . Since at redshift  $z = 4.4$  our pixel scale on the **SHERWOOD** data is 1.3 km/s, we obtain that in velocity space a window of  $\sim 40$  km/s is needed to recover the density at a pixel. This particular dynamic is coherent with the underlying physical process, which is a strong robustness sign of our machine learning model. In fact, for the typical IGM gas in the **SHERWOOD** suite, the Lyman- $\alpha$  absorption cross-section profile has a typical scatter of (see Equation 1.35)  $b(T) \sim 20$  km/s.

### 3.5.2 Covariate shift

As we have already mentioned when discussing Figure 3.13, saturated regions lead to larger uncertainties in the network’s predictions, reflecting the fact that noise dominates over the physical signal. Observe again the saturated region around  $7\text{h}^{-1}\text{cMpc}$  and  $8\text{h}^{-1}\text{cMpc}$  in Figure 3.13. Both of these regions have completely different density profiles, but the network predicts the same U-shape profile with a similar peak density. This peak density is slightly above the mean density in the simulation box and is similar for the CDM and WDM3 models. We can interpret this as the network learning a unique mean “high-density” value for saturated regions and the whole dataset. The way the model predicts those mean densities based on the training dataset is, again, far from being

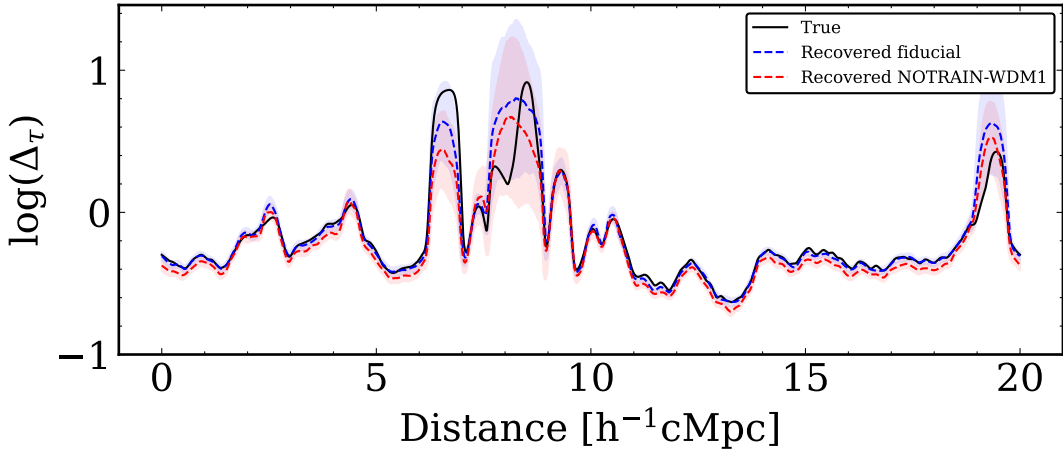


Figure 3.21: The **NOTRAIN-WDM1** model predicting on a WDM1 skewer, compared to the fiducial model trained on the whole **SHERWOOD** dataset.

trivial. However, it is clear that the training data contains all the information leading to any possible bias/characteristic in the deep learning model predictions. An important effect regarding the available data is *covariate shift*. Covariate shift occurs when the training and validation data are sampled from different distributions. Covariate shifts can be difficult to detect and can lead to biased predictions. In this work, we try to test the generalisation capabilities of our model by adding random noise and validation on unseen data from multiple hydrodynamical codes with different specifications, to make sure the model is learning the relevant physics. This is a pragmatic approach to address covariate shifts since more formal techniques are out of the scope of this work. Nonetheless, we are aware that an insufficient dataset can significantly degrade performance. As an illustration of the undesirable effects of covariate shift, we retrain the fiducial architectures on a subset of the **SHERWOOD** dataset where we iteratively eliminate each one of the WDM models. We call this set of models **NOTRAIN**. For instance, **NOTRAIN-WDM1** has not been trained on the WDM1 data. In Figure 3.21 and Figure 3.22 we show the models **NOTRAIN-WDM1** and **NOTRAIN-WDM4** predicting, respectively, on WDM1 and WDM4 skewers from the **SHERWOOD** dataset.

Note the clear covariate shift effect in Figure 3.21, where **NOTRAIN-WDM1** has a systematic bias towards lower densities. In comparison, in Figure 3.22 the model **NOTRAIN-WDM1** shows no clear indication of any bias and is almost indistinguishable from the fiducial model. In the former case, the model has to extrapolate on data generated from an unseen model, which gives clearly an incorrect prediction. In the latter case, the model has been trained on CDM and WDM3, so predicting on WDM4 is an interpolation task.

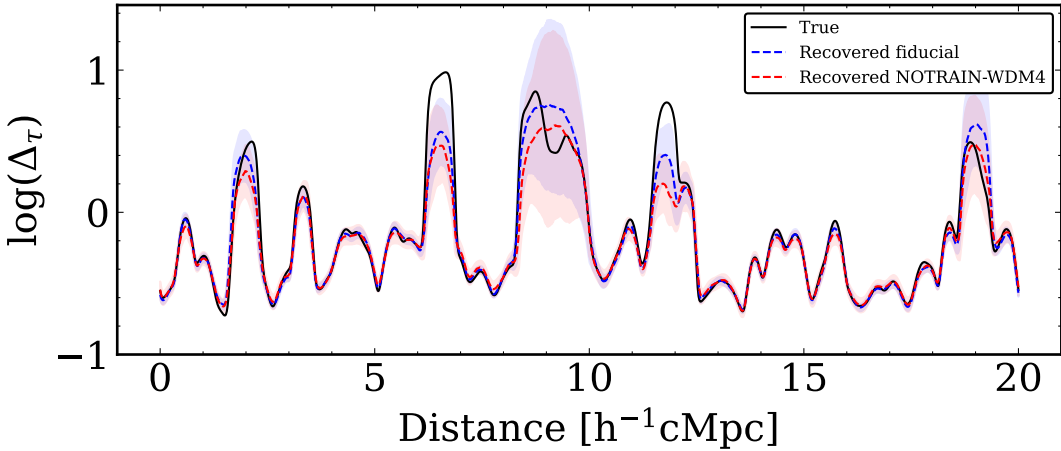


Figure 3.22: The NOTRAIN-WDM4 model predicting on a WDM4 skewer, compared to the fiducial model trained on the whole SHERWOOD dataset.

### 3.5.3 Extreme covariate shift and malicious data

In regression tasks related to computer vision, it is customary to mask certain parts of the input to explore how the model reacts to specific features. Following this idea, we have designed a set of malicious Lyman- $\alpha$  skewers that include artefacts and unnatural features that are not present in the training dataset. Therefore, this can be considered an extreme case of covariate shift. In Figure 3.23 we show the fiducial model predictions for two such skewers. In the first case, we consider a fully saturated skewer with zero flux and only a small amount of noise. Observe how the model makes an educated guess and predicts the mean density for the whole skewer. However, the model is very confident in the predictions and produces minimal uncertainties. This is not correct from the physical standpoint, since any density higher than the truth can produce a saturated flux. In the second skewer, we have complete transmission except for a saturated absorption feature. The predictions for the pixels with complete transmissions are below the mean density, and on the saturated pixels it is above the mean density with a higher uncertainty. This is closer to a “real” absorption feature with a more accurate prediction.

### 3.5.4 Model pruning

Pruning refers to the idea of eliminating certain components of a deep neural network, or equivalently, considering a sub-network. The motivation to prune a network is generally to reduce the number of parameters, which can improve interpretability, and allow users to better trace the flow of information through the network. Since most deep networks

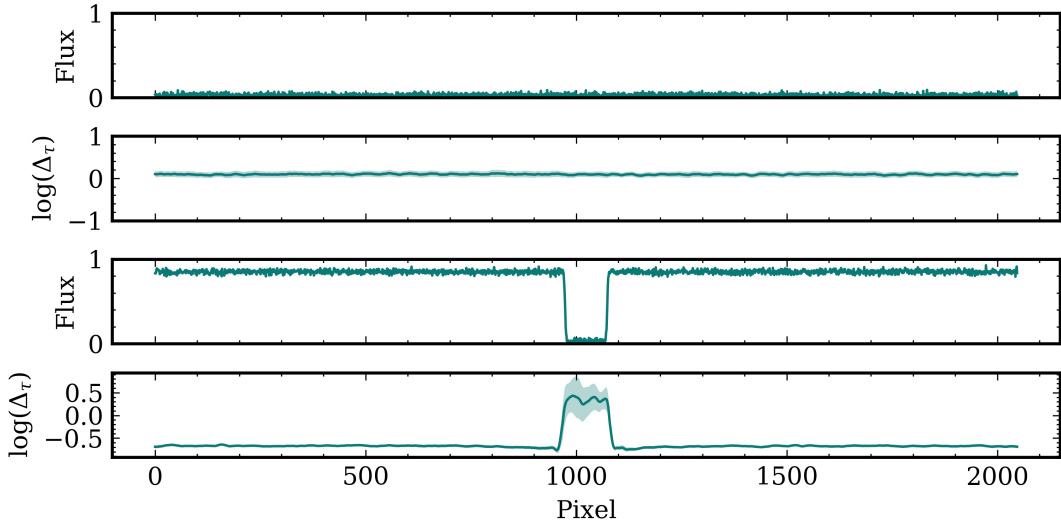


Figure 3.23: Two examples of user-defined input fluxed for our fiducial neural network, featuring examples of extreme covariate shift.

are over-parametrised, pruning can improve training while maintaining a very similar performance to the original architecture. Pruning is an active area of research, and efforts are being made to use domain-specific expertise to prune networks and make informed choices about their topology [79]. In this work, we have used `OPTUNA` in section 3.2.4 to tune the hyperparameters of the model on the sole basis of a performance metric function. This naturally over-parametrises the network, with connections and filters that might be redundant. This means that there is potential room for improvement when it comes to finding more interpretable networks with fewer parameters and more stable training.

To illustrate how pruning can affect the performance of our model, we briefly focus on the first convolutional layer of the architecture in Figure 3.11. In Figure 3.24 we show the activation of the first 4 convolutional filters for a trained network with architecture  $[2, 2]$ ,  $[4, 16]$  for a randomly selected skewer, following the notation in Table 3.1. Note that out of the four filters, the blue and green ones are scaled versions of each other, and similarly, the red and orange filters are also scaled versions of one another. To test if this redundancy affects the network, we prune half of the filters in this first layer to an architecture  $[2, 2]$ ,  $[2, 16]$ . Figure 3.25 shows the training NLL curve for both architectures. As can be seen, they reach a similar performance in terms of the NLL, but the pruned architecture has a more stable learning curve and converges in a smoother way.

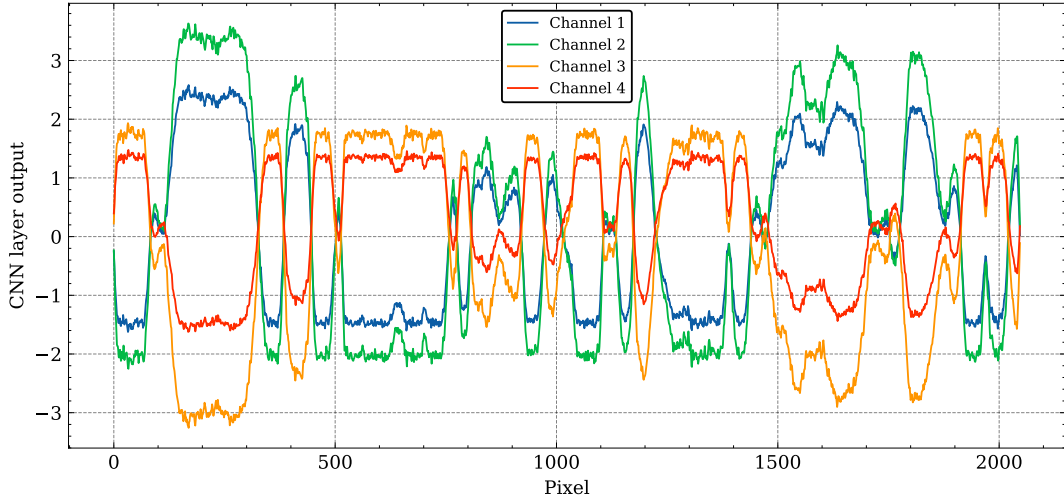


Figure 3.24: First layer activation of the convolutional filters for a trained network with architecture  $[2, 2], [4, 16]$  for a randomly selected CDM skewer from SHERWOOD.

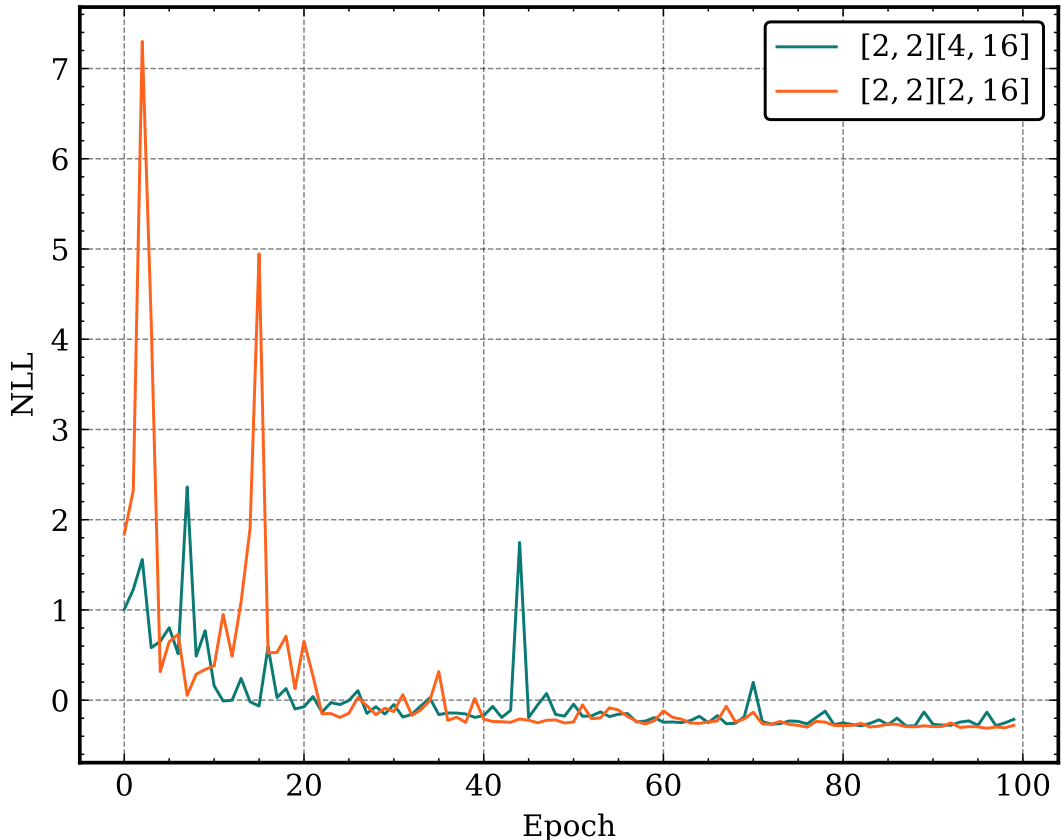


Figure 3.25: Training curves for the NLL comparing the model  $[2, 2], [4, 16]$  and the pruned architecture  $[2, 2], [2, 16]$  with half of the convolutional filters in the first layer.

# 4 Constraining warm dark matter at the density level

## 4.1 Inference pipeline: from Lyman-alpha skewers to WDM constraints

In Section 3 we have given a detailed analysis of our Bayesian deep-learning algorithm to recover IGM densities from a Lyman- $\alpha$  skewer. The baryonic density of the IGM is sensitive to the WDM mass through a clear physical mechanism related to gravitational clustering. In this section, we use the recovered IGM density fields to constrain WDM candidates. Note that the natural observable quantity related to the Lyman- $\alpha$  forest is the flux. As a consequence, an almost omnipresent choice in the literature has been to work directly with summary quantities on the flux, which is a proxy of the underlying density. Such summaries include the power spectrum (PS) [23], the curvature [80], the probability distribution function (PDF), etc. The deep-learning approach introduced in Section 3 allows us to directly recover the baryonic density field along a line of sight, thus having full access to the field-level IGM properties. In this section, we use the recovered  $\Delta_\tau$  fields by our neural network to constraint WDM directly at the density field level. Recall Figure 1.3 and Figure 2.7 showing how different WDM models affect the density field. We strive to capture that difference in the WDM models to constrain which free-streaming lengths are compatible with QSO observations. Note that for a given line of sight, the precise value of the density field not only depends on the WDM masses (and other possible physical parameters), but most crucially it depends on the random density fluctuations that have seeded the gravitational collapse process. Equivalently, in a simulation setting, the obtained densities would depend on the seed used to initiate each simulation. This makes it infeasible to compare a given Lyman- $\alpha$  skewer to a simulated one and means that we must use aggregated summaries over multiple skewers that capture the global properties of the field. In this work, we perform the inference

using the density PDF as the summary statistic of choice. This is a well-tested and robust statistic [73]. In Section 4.6.4 we give an additional argument, based on Information Maximising Neural Networks, to support this choice of summary statistic.

The basic working principle of the inference pipeline is to fit the observed  $\Delta_\tau$  PDF, with its associated uncertainties, to the corresponding  $\Delta_\tau$  PDF produced by each WDM model. To compare similar quantities, we always work with the recovered field by our neural network from Section 3. Note that in the **SHERWOOD** suite only a finite number of DM models are available, due to the computational cost of running this simulation. In more detail, we only have access to the models CDM, and WDM1,2,3,4,8,12. We smoothly and linearly interpolate the PDF by interpolating each PDF bin to generate a  $\Delta_\tau$  PDF in the range of WDM masses from 0 to 1 KeV. Note that, since we expect the real observations to fall close to the CDM model, and have multiple simulations close to CDM, we expect this interpolation not to limit the inference pipeline. See Figure 2.7 again and observe how similar are the PDFs for CDM and WDM3.

For each DM model of inverse mass  $m$ , we denote by  $\text{PDF}(m)$  the  $\Delta_\tau$  PDF computed over the recovered densities by our NN network over all available sightlines in the **SHERWOOD** or **SHERWOOD THERMAL** datasets. We refer to this as the model PDF. Let us denote by  $\widehat{\text{PDF}}$  the recovered PDF for a target set of (observed) skewers. Then, we fit  $\widehat{\text{PDF}}$  to the model PDFs using a simple  $\chi^2$  fit:

$$\chi^2(m) = \sum_i \frac{(\text{PDF}(m)_i - \widehat{\text{PDF}}_i)^2}{(\sigma_i)^2}, \quad (4.1)$$

where the index  $i$  refers to each PDF bin and  $\sigma_i$  are the uncertainties on the observed data. If the data is independently and normally distributed, the quantity in Equation 4.1 follows a  $\chi^2$  distribution [81]. The model that minimises the quantity is the best-fit model, on which we can compute uncertainties and obtain a confidence region of compatible models with the observed data. Since we are only fitting a single parameter model, the 1 and 2-sigma confidence regions on the WDM mass are given, respectively, by the boundaries of

$$\chi^2(m) - \chi^2_{\min} = 1, 4, \quad (4.2)$$

where  $\chi^2_{\min}$  is the best-fit  $\chi^2$  value. In the following, we will be interested in the  $2\sigma$  confidence regions. This region can be interpreted as the set of WDM models that guarantee to contain the “true” model with a 95% probability. In the current literature, WDM constraints are often reported as the  $2\sigma$  upper limit, where the lower limit typically corresponds to CDM. The current more stringent  $2\sigma$  WDM limit constraints are  $\sim 3$

KeV, see [23] and [26]. Note that this fitting procedure is non-Bayesian, in the sense that we don’t include any prior knowledge or use Bayes’ theorem. Again, this procedure is compared in Section 4.6.4 to an IMNN Bayesian fit, leading to similar results.

## 4.2 Inference testing on simulated Sherwood spectra under realistic observational conditions

In this first section, we run our inference pipeline from Section 4 using a set of toy observed skewers. More precisely, we use our neural network trained on different subsets of the **SHERWOOD** dataset and use validation **SHERWOOD** skewers as the “observed” skewers.

### 4.2.1 Untrained DM models

We begin by testing the robustness interpolation and extrapolation capabilities of the neural networks by considering the **NOTRAIN** models that are trained on data that iteratively excludes each one of the WDM models. For each one of those trained neural networks, for instance, **NOTRAINWDM4** (which was not trained on WDM4), we predict on the WDM4 sightlines, compute the recovered  $\Delta_\tau$  with its uncertainties according to Section 3.4 and run the inference pipeline. We also perform additional variations by running the pipeline only on the PDF bins whose value is greater than a fixed constant. This has the effect of only fitting the peak of the PDF and neglecting the low-information tails. Figure 4.1 summarises these inference tests. Each plot corresponds to a different fit combining predictions from each **NOTRAIN** model with each of the masks applied to the PDF when fitting. The light and dark blue regions correspond to the 1 and 2 sigma confidence regions. The red line corresponds to the true DM model mass and the black line to the best-fit model that minimises the  $\chi^2$ . The blue curve is the  $\chi^2$  metric. Note that we are using all 5000 sightlines on the inference step. This is not a realistic sample size, but rather a test of the inter(extra)polation performance of the pipeline.

Recall that on WDM2,3,4 the models are interpolating. Observe that as a consequence, the recovered mass is consistently recovered within the  $1\sigma$  region. In contrast, with the models CDM and WDM1, the neural networks have to extrapolate on unseen DM models. As expected, the recovered model mass might not even be included in the  $2\sigma$  regions, meaning that the pipeline fails to correctly recover the true mass if we interpolate models. This does not affect our prediction with real data, since, as we have already mentioned, current WDM constraints favour a lower mass limit of  $\sim 3$

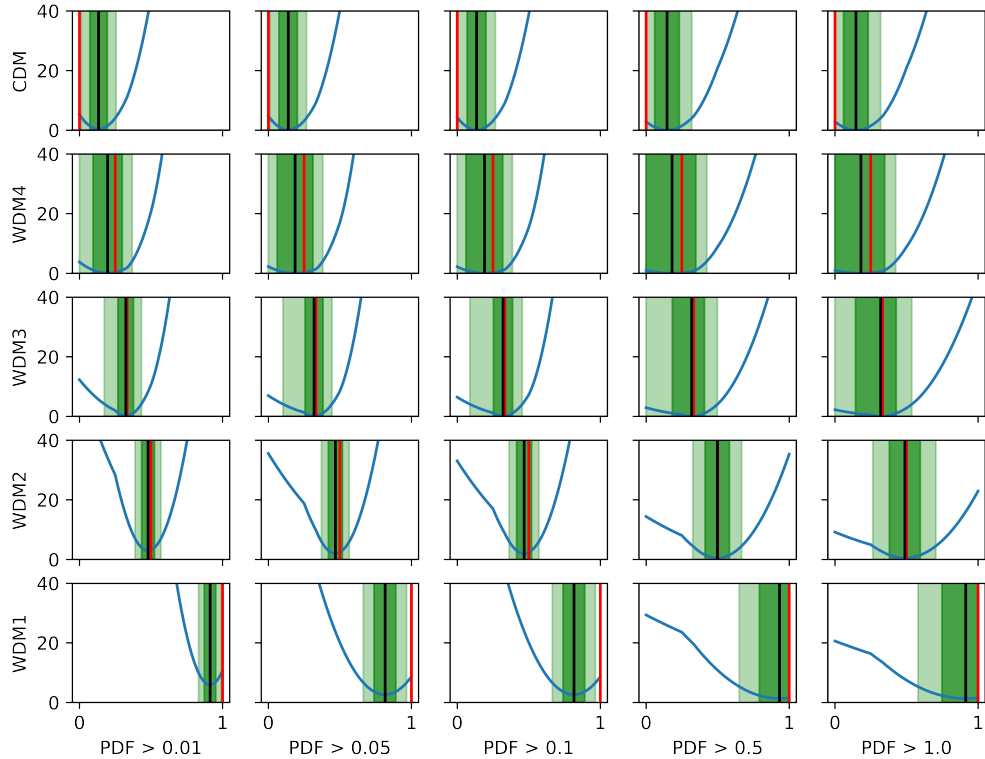


Figure 4.1: Inference results on the NOTRAIN neural networks. Each plot corresponds to a different fit combining predictions from each NOTRAIN model with each of the masks applied to the PDF when fitting. The light and dark blue regions correspond to the 1 and 2 sigma confidence regions. The red line corresponds to the true DM model mass and the black line to the best-fit model that minimises the  $\chi^2$ . The blue curve is the  $\chi^2$  metric. Note that we are using all 5000 sightlines on the inference step.

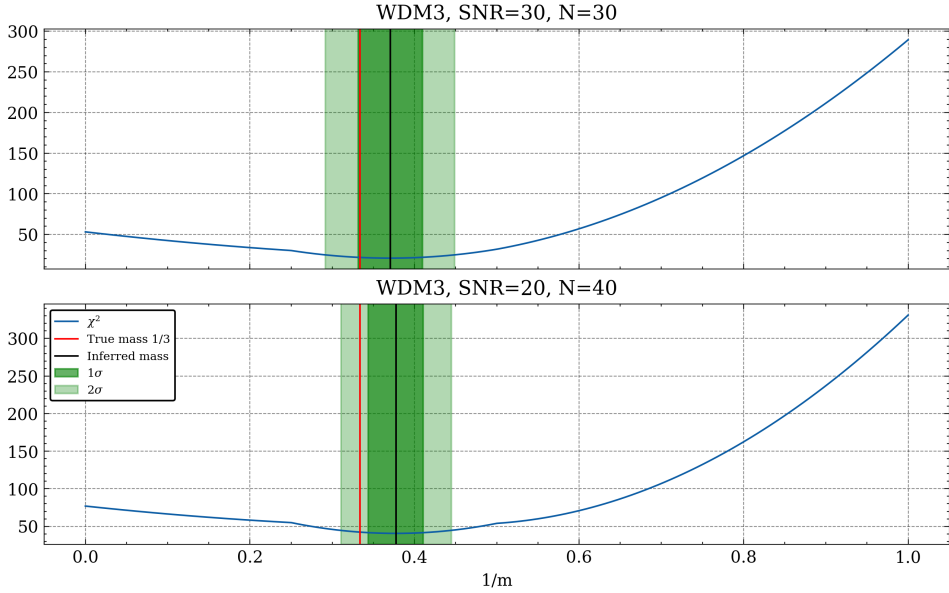


Figure 4.2: Inference predictions on WDM3 for different combinations of SNR and number of targets N.

KeV. Lastly, observe in Figure 4.1 that the mask applied on the horizontal axis does not significantly affect the recovered masses.

### 4.2.2 Realistic observational conditions

In this section, we explore the effect of realistic observational conditions, such as the number of observed quasars, the signal-to-noise ratio (SNR), or the instrumental resolution, in the inferred DM constraints. For that purpose, we use typical parameters for the Ultraviolet and Visual Echelle Spectrograph (UVES) on the European Southern Observatory’s Very Large Telescope [82]. We consider a spectral resolution of 6 km/s per pixel, variable SNR in the range 20 – 30 and a variable number of targets in the range 30 – 40. Note that the skewers in the **SHERWOOD** dataset are  $20h^{-1}c\text{Mpc}$  in length, while the spectral range in the UVES instrument expands multiple times that range. In particular, since measurements can extend up to redshift differences  $\Delta z \sim 1$ , we assume that each observed spectrum can be decomposed into  $\sim 15$  of our **SHERWOOD** skewers.

A common compromise in an observational program with a fixed observational time is between the number of targets and exposure time per target, which determines the SNR. In Figure 4.2 we show how prioritising SNR or the number of targets affects the inferred WDM masses on the WDM3 model. In general, we find that increasing the target number leads to slightly tighter confidence regions while increasing the SNR

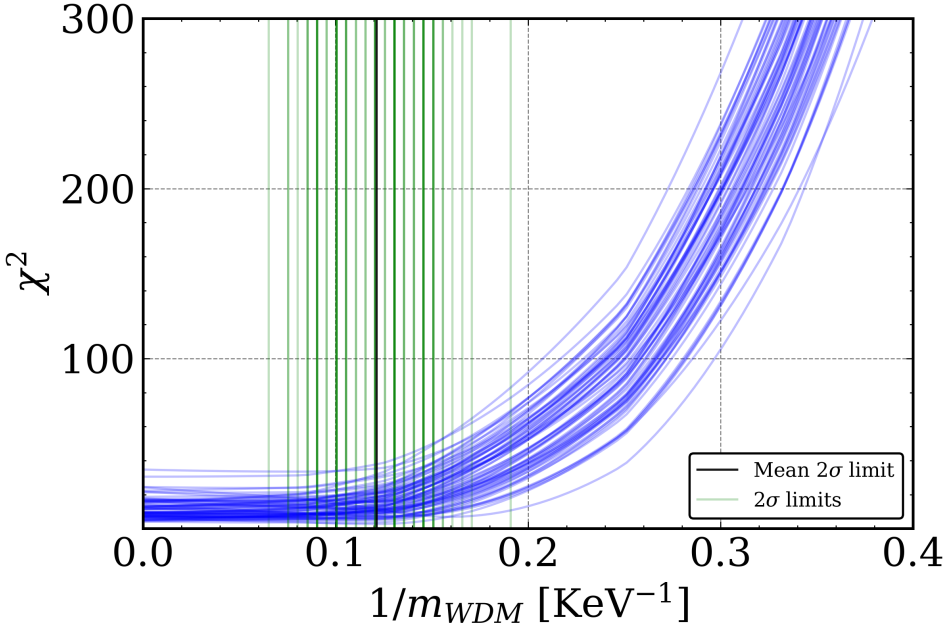


Figure 4.3: The figure shows 100 different  $\chi^2$  fits on 450 SHERWOOD CDM skerwers and the  $2\sigma$  constraints distribution as we vary the exact obsserved draw.

leads to more accurate constraints. Most crucially, observe how the true model mass is, in both cases, recovered within  $2\sigma$ .

We now evaluate the constraining power of the approach developed in this work. To that end, we assume CDM to be the true DM model and use our fiducial neural network trained on SHERWOOD. We then draw 450 simulated SHERWOOD CDM skewers, corresponding to 30 observed UVES spectra, post-process them with a resolution of 6 km/s, add random Gaussian noise with SNR = 30 and use them to run our inference pipeline from Section 4. Since the fit depends on the exact draw of “observed” skewers, we repeat this process 100 times with a random draw each time to obtain the  $2\sigma$  limit distribution.

Figure 4.3 shows the distribution of  $2\sigma$  limits and the mean  $2\sigma$  constraint produced by this process. The mean  $2\sigma$  constraint that we report for the inverse mass is  $\sim 0.12$  KeV $^{-1}$ , or  $\sim 8.3$  KeV for the WDM model mass. Again, recall that in this section we are using simulated data.

To confirm that the fitting process works as expected, we plot in Figure 4.4 the best fit PDF, which corresponds to the CDM model according to Figure 4.3 and an example recovered PDF from a set of 450 observed skewers. Recall that the uncertainties in the recovered PDF include the sample scatter using bootstrapping as well as the machine learning uncertainties, as we have discussed in Section 3.4. As expected, the observed

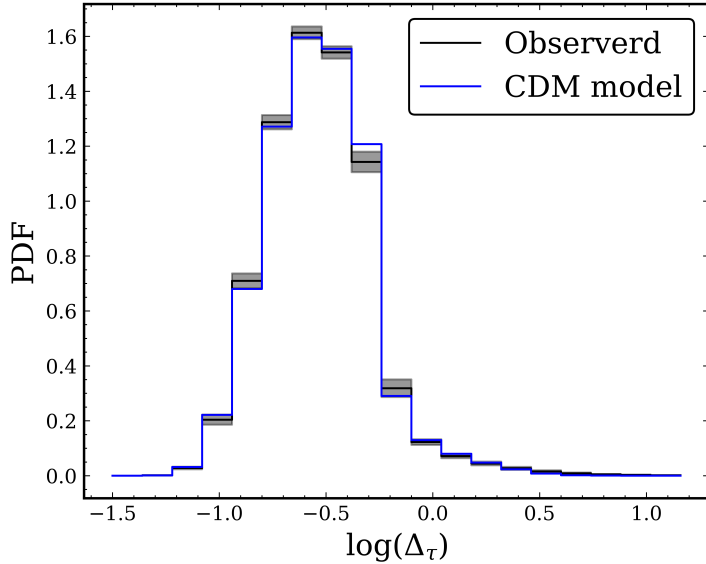


Figure 4.4: An example observed  $\Delta_\tau$  PDF recovered using 450 simulated CDM skewers and its uncertainties in black, plotted against the model CDM PDF, which is the best-fit model in the  $\chi^2$  test.

PDF is within a  $2\sigma$  distance of the model CDM PDF.

In Figure 4.5 we summarise in black the current  $2\sigma$  state-of-the-art constraint in the literature, using a non-ML approach. In orange, we compare the forecasted constraints from the non-machine learning approach in [26] to our approach in an equivalent dataset to the one used in Section 4.2.2. Compared to current limits, our forecasted constraint is a twofold improvement, from  $\sim 4$  to  $\sim 8$  KeV. On the same dataset, we forecast our machine learning technique to match the approach in [26]. As a significant caveat, note that the work in [26] is a joint analysis not only on WDM but also on thermal parameters of the IGM, cosmological parameters, etc. The aforementioned paper encompasses a larger number of parameters with a more complex and refined approach than this work.

### 4.3 Inference on alternative hydrodynamical codes

In this section, we test our inference pipeline on Nyx, a different hydrodynamical code. We start by describing broadly the differences between the Nyx run used and the Sherwood simulations, and then we use our fiducial neural network trained on the **SHERWOOD THERMAL** suite to recover the Nyx densities and obtain the corresponding constraints.

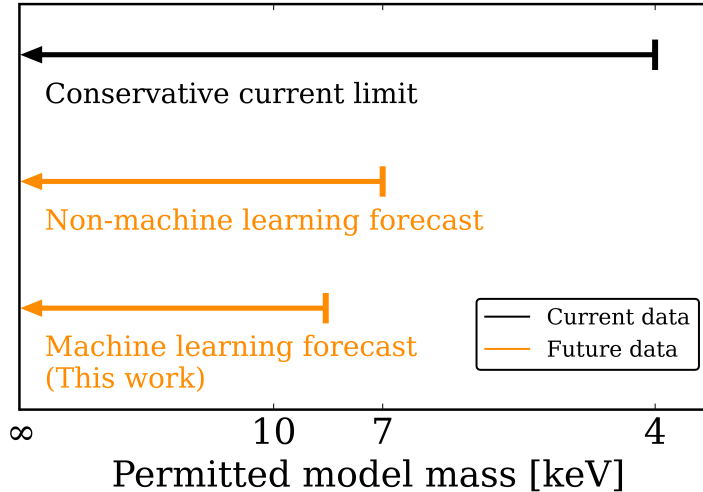


Figure 4.5: Summary  $2\sigma$  relic WDM constraints based on [26] compared to the forecast obtained in this work. Recall that this forecast has been obtained using simulated data from the **SHERWOOD** CDM run, as explained in Section 4.2.2.

### 4.3.1 The Nyx code

Nyx [83] is an N-body and gas dynamics code for large-scale cosmological simulations. Nyx uses Adaptive Mesh refinement (AMR) in time and space based on the Eulerian formulation of hydrodynamics, as opposed to the Lagrangian formulation used in the GADGET code employed by the Sherwood simulations. We expect Sherwood and Nyx runs to intrinsically show these non-physical differences related to the different hydrodynamical solvers.

In the Nyx code, dark matter is modelled as discrete Lagrangian particles, allowing the code to follow their evolution under gravity effectively. The evolution of its phase space distribution  $f$  is given by the collisionless Boltzmann equation

$$\frac{\partial f}{\partial t} + \frac{1}{ma^2} \mathbf{p} \cdot \nabla f - m \nabla \phi \cdot \frac{\partial f}{\partial \mathbf{p}} = 0 \quad (4.3)$$

where  $m$  and  $\mathbf{p}$  are mass and momentum and  $\phi$  is the gravitational potential.  $a$  is the scale factor, obtained by using a second-order Runge-Kutta solver. Nyx solves this phase space evolution of  $f$  by sampling its distribution and evolving the particles as an N-body system. The gravitational potential is obtained by solving the Poisson equation

$$\nabla^2 \phi(\mathbf{x}, t) = \frac{4\pi G}{a} (\rho_b + \rho_{dm} - \rho_0) \quad (4.4)$$

where  $\rho_0$  is the mean density,  $\rho_b$  the baryonic density and  $\rho_{dm}$  the dark matter density.

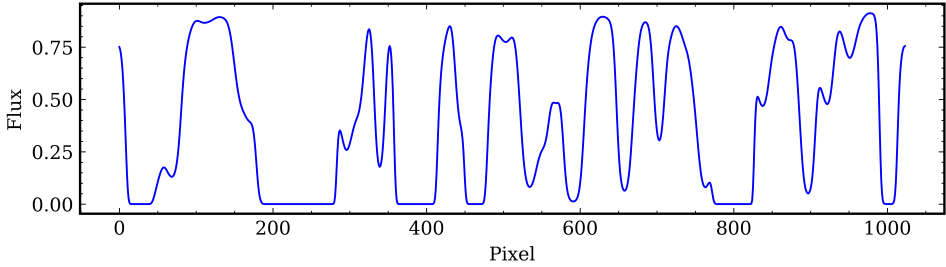


Figure 4.6: A typical Lyman- $\alpha$  skewer obtained from the Nyx runs with  $z_{\text{re}} = 6$  at  $z = 4.4$ .

Dark matter particles are gravitationally coupled to a baryonic fluid, which is treated as an inviscid ideal gas. The gas is described by a state vector  $\mathbf{U} = (\rho_b, a\rho_b U, a^2 \rho_b E, a^2 \rho_b e)$  where  $U$  is the peculiar proper baryonic velocity,  $e$  the internal energy, and  $E$  the total energy. The hydrodynamical equations are approximated by a Riemann solver and can be written in the form

$$\frac{\partial \mathbf{U}}{\partial t} = -\nabla \cdot \mathbf{F} + S_e + S_g + S_{HC}, \quad (4.5)$$

where  $F$  is the flux vector,  $S_g$  the gravity source term,  $S_{HC}$  the heating and cooling term, and  $S_e$  the internal energy flux.

In the rest of this section, we consider 3 Nyx runs at  $z = 4.4$  using CDM and  $20\text{h}^{-1}\text{cMpc}$  boxes. The 3 runs are different in the different reionisation history and are labelled by the end of reionisation redshifts of  $z_{\text{re}} = 6, 7, 8$ . Each skewer has 1024 pixels. Figure 4.6 shows an example Lyman- $\alpha$  skewer for the Nyx run with  $z_{\text{re}} = 6$ .

Since we want to test our inference pipeline, in this test we want to be as agnostic as possible about the nature of our ‘‘observed’’ Nyx spectra. If real data is observed, we would, *a priori*, have no information on the exact thermal history that has led to the observed field. A similar situation occurs with the Nyx runs. Our **SHERWOOD THERMAL** dataset constrains thermal models, but we have *a priori* no guarantee that they match the Nyx runs that we are analysing. In fact, we know that this is not the case. To visually explore the difference between the Nyx and **SHERWOOD THERMAL** runs, we plot the 2D distribution of pixels in the temperature-density plane. We show the result in Figure 4.7, comparing the Nyx CDM run  $z_{\text{re}} = 6$  to the **SHERWOOD THERMAL** CDM runs. The top panel shows the 95% contours in red and black colours. The bottom panel shows the temperature distribution at the mean density value. As can be observed, the Nyx does not fit any of the runs in our training dataset.

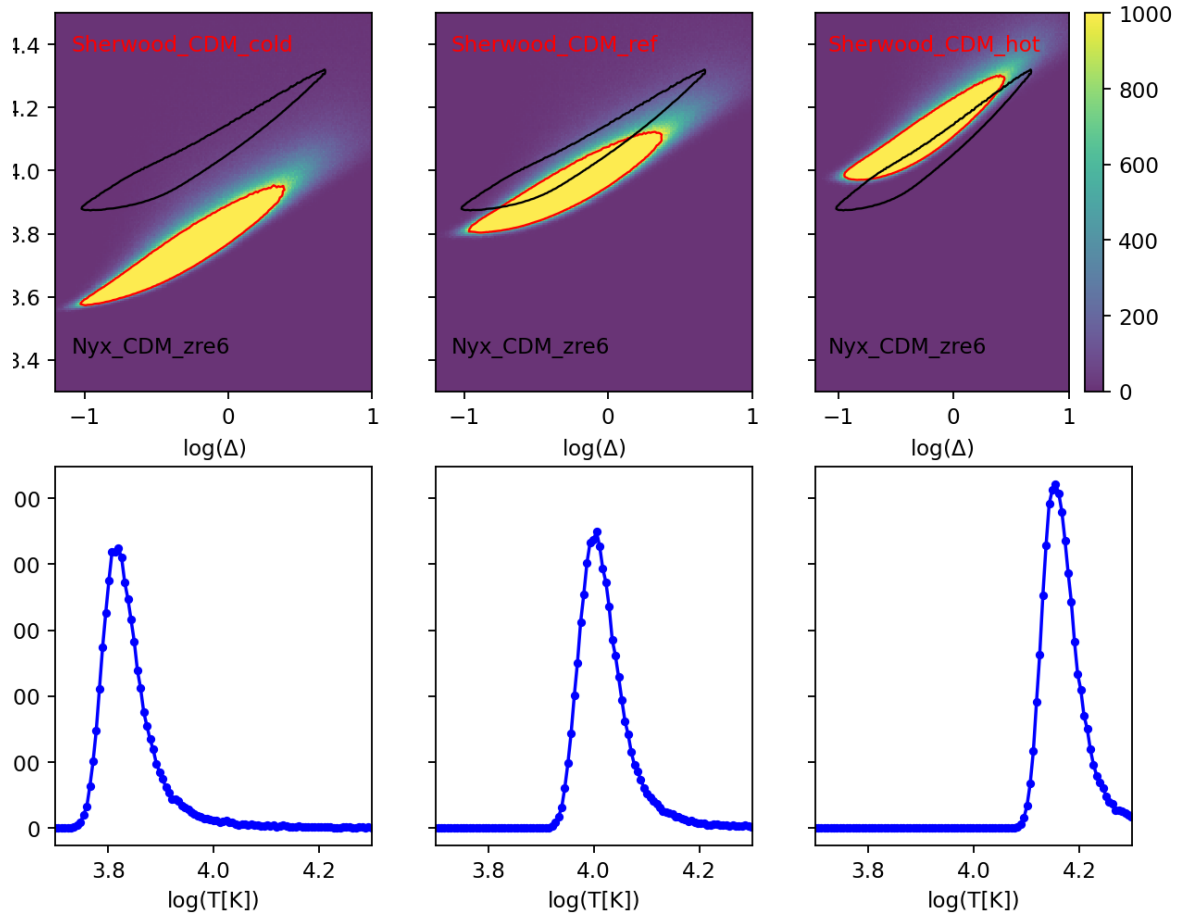


Figure 4.7: The 2D distribution of pixels in the temperature-density plane comparing the Nyx CDM run  $z_{\text{re}} = 6$  to the SHERWOOD THERMAL CDM runs. The top panel shows the 95% contours in red and black colours. The bottom panel shows the temperature distribution at the mean density value. As can be observed, the Nyx does not fit any of the runs in our training dataset.

### 4.3.2 Inference test on Nyx Lyman-alpha skewers

We begin by evaluating the performance of our fiducial neural network with frozen weights trained on **SHERWOOD THERMAL** when predicting on skewers generated by the **Nyx** code. In Figure 4.8 we show a violin plot with the  $1\sigma$  residues distribution as defined in Equation 3.23. Values in the range  $[-1, 1]$  correspond to pixels that have been successfully recovered within a  $1\sigma$  accuracy. Observer how the models with earlier reionization ( $z_{\text{re}} = 7$  and  $z_{\text{re}} = 8$ ), which have lower temperatures, have a higher recovery rate. This is likely because our training data set contains more WDM models close to CDM, and we know that high WDM masses and low temperate have a degenerate effect on the Lyman- $\alpha$  forest. In general, we note that the  $\geq 75\%$  of the pixels are correctly recovered. Even if the performance is slightly degraded compared to the **SHERWOOD THERMAL** validation, as expected, this is a strong indication that the neural network has learnt the relevant physical relations and not potential simulation-specific correlations.

We then run the same inference pipeline for the  $z_{\text{re}} = 6$  model as we did in Section 4.2.2 with a single major difference. Since we know that the **Nyx** runs do not fit any of our thermal models (and the same circumstance will occur when using real observations), we need to utilise the fiducial neural network trained on multiple thermal modes, **SHERWOOD THERMAL**. Additionally, when fitting the recovered  $\Delta_\tau$  PDF to each model PDF, we will have 3 different  $\chi^2$  curves for each one of the thermal models {ref, hot, cold}. To avoid a joint optimization problem and constraining the thermal history on top of the WDM mass (which is out of the scoop of this work, and also unrealistic since we are not using a fine thermal model grid), we will select the thermal model that minimises the  $\chi^2$  value, that is

$$\min_{t,m} \chi^2(t,m), \quad (4.6)$$

where  $t \in \{\text{ref, hot, cold}\}$  and  $m$  labels the continuously interpolatted inverse warm dark matter mass. We compute  $\chi^2(t, m)$  and find that the ref and hot model produce similar  $\chi^2$  values, while the cold model has  $\chi^2 \sim 1000$ , as expected from Figure 4.7. Both the ref and hot models produce a similar  $2\sigma$  lower bound on the WDM mass:  $m_{\text{WDM}} \gtrsim 10$  KeV. Compared to Section 4.2.2, the results are fairly similar, showcasing the robustness of our approach.

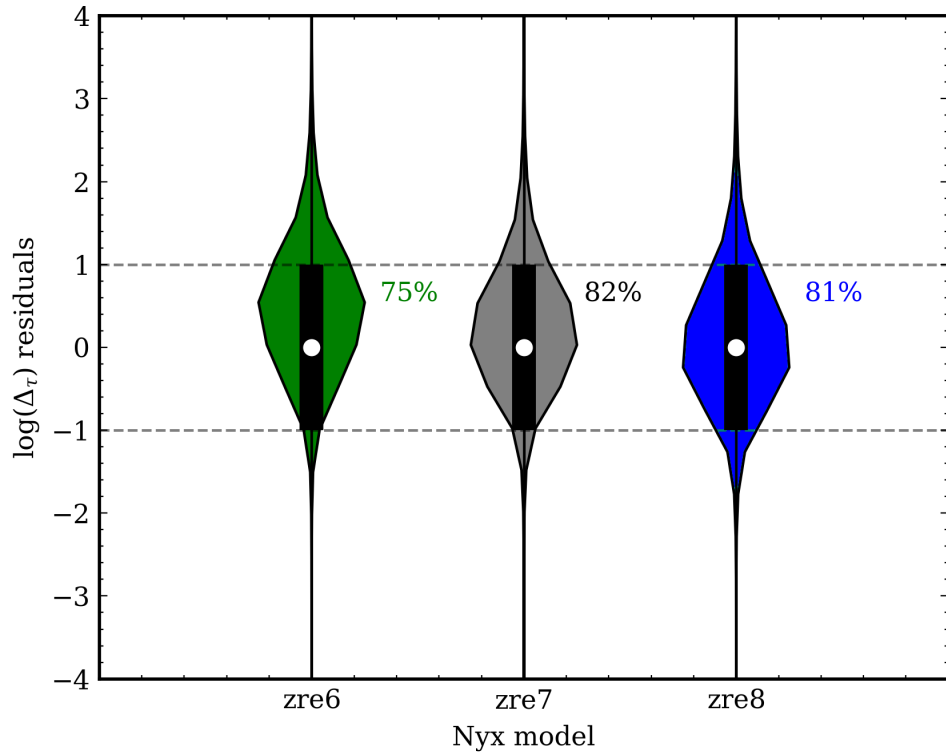


Figure 4.8: Violin plot with the  $1\sigma$  residues distribution as defined in Equation 3.23. Values in the range  $[-1, 1]$  correspond to pixels that have been successfully recovered within a  $1\sigma$  accuracy. Observe how the models with earlier reionization ( $z_{\text{re}} = 7$  and  $z_{\text{re}} = 8$ ), which have lower temperatures, have a higher recovery rate. This is likely because our training data set contains more WDM models close to CDM, and we know that high WDM masses and low temperate have a degenerate effect on the Lyman- $\alpha$  forest. In general, we note that the  $\geq 75\%$  of the pixels are correctly recovered.

Table 4.1: List of the SQUAD DR1 sightlines used, see [82] for the reduction details, together with their emission redshift and the average continuum SNR. All sightlines are  $20\text{h}^{-1}\text{cMpc}$  and centered at  $z = 4.4$ .

SQUAD DR1 name	$z_{\text{em.}}$	SNR
J004054	4.976	33
J021043	4.65	25
J025019	4.77	12
J030722	4.728	50
J033829	5.032	14
J145147	4.763	100

## 4.4 WDM constraints from SQUAD DR1 observational data

We begin applying our density recovery and WDM mass inference pipeline to a set of 6 observed quasar sightlines from the SQUAD DR1 survey [82]. Since we are working with observational data, we will always train the model with the complete **SHERWOOD THERMA L** dataset that includes varied thermal histories and WDM masses. Note that since we are not trying to constrain the thermal history (or other parameters that can affect the Lyman- $\alpha$  forest), we should ideally use a training set that includes as much variation as possible to make sure the neural network can perform in a scenario where we ignore the true thermal history.

Our SQUAD DR1 data consists of 6 Lyman- $\alpha$  sightlines of size  $20\text{h}^{-1}\text{cMpc}$  with varied SNR (see Table 4.1), observed with the Ultraviolet and Visual Echelle Spectrograph (UVES) on the European Southern Observatory’s Very Large Telescope, which has an average resolution of  $\text{FWHM} \approx 6\text{km s}^{-1}$ . We consider sightlines centred at  $z = 4.4$  for this specific application. Since each quasar has its own noise level, we retrain the same fiducial architecture with the corresponding noise level before the prediction step.

We are then set to predict the recovered density fields for each sightline. Figure 4.9 shows all our SQUAD DR1 skewers together with the recovered  $\Delta_\tau$  field.

We now compute the  $\chi^2(t, m)$  for all 3 thermal models, which are minimised for the respective CDM run as expected, and find that the thermal model producing a minimal  $\chi^2$  is the cold. In Figure 4.10 we show, in the left panel, all 3  $\chi^2$  curves as a function of the WDM mass. The right panel shows the recovered  $\Delta_\tau$  PDF from the SQUAD DR1 sample together with the best-fit model, corresponding to the CDM cold **SHERWOOD**

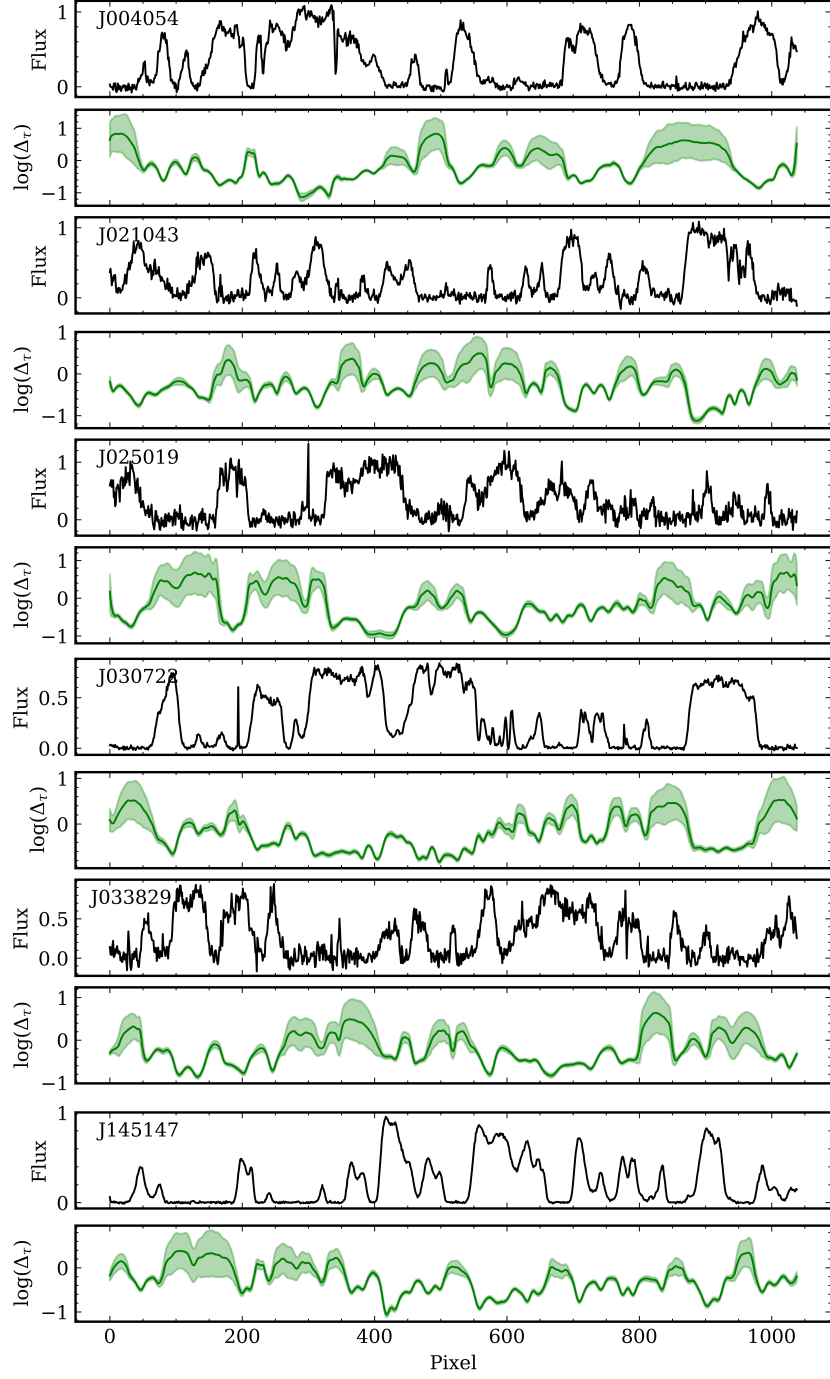


Figure 4.9: All 6 sightlines from the SQUAD DR1 sample in Table 4.1. As can be seen, the noise levels vary, depending on the exposure time to the target. All sightlines are  $20\text{h}^{-1}\text{cMpc}$  and centered at  $z = 4.4$ . We show the recovered density field by our fiducial architecture trained on **SHERWOOD THERMAL** and retrained with the noise specifications of each target.

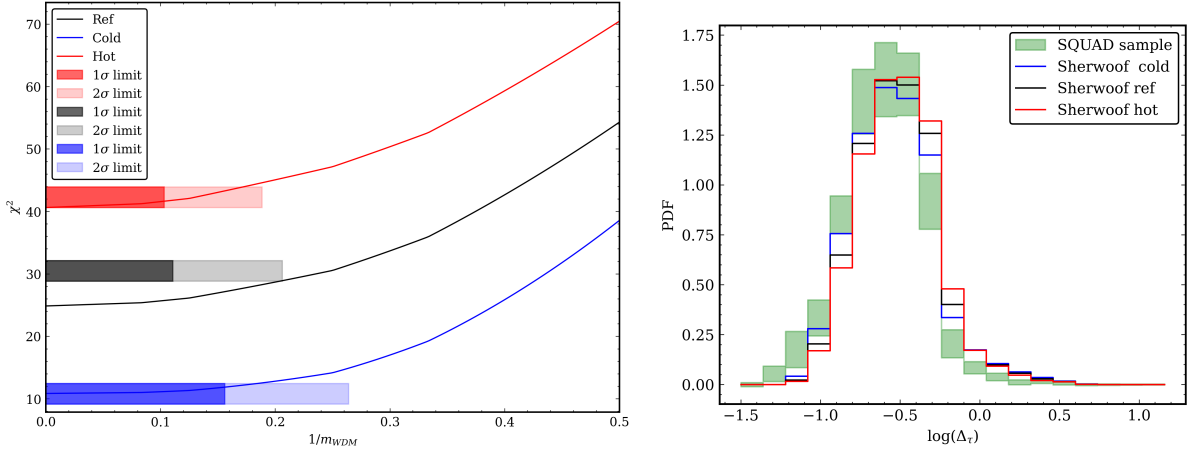


Figure 4.10: In the left panel, we show all 3  $\chi^2$  curves as a function of the WDM mass, together with the  $1, 2\sigma$  confidence regions. The right panel shows the recovered  $\Delta_\tau$  PDF from the SQUAD DR1 sample with the symmetric uncertainty envelop, together with the best-fit model, corresponding to the CDM cold SHERWOOD THERMAL model.

THERMAL model. Using the best-fit thermal model, we find a lower bound on the WDM mass of  $m_{WDM} \gtrsim 3.8$  KeV.

## 4.5 WDM constraints from GHOST observed spectrum

We now consider a Lyman- $\alpha$  skewer obtained from the GHOST instrument, which corresponds to the ultra-luminous quasar J0306+1853 [84] with emission redshift  $z = 5.363$ , see Figure 4.11. For this spectrum, we have a continuum reconstruction in the range  $[971, 1210]$  Å in the emission rest frame, with a resolution of  $\text{FWHM} \sim 10$  km/s. For this target, we use the Lyman- $\alpha$  forest in the range  $4.5 \leq z \leq 4.9$ . In the case of lower redshifts, the Lyman- $\beta$  forest would be visible, while for higher redshifts, a Damped Lyman- $\alpha$  system (DLA) at  $\sim 1150$  Å occurs. We extract skewers of length  $20\text{h}^{-1}\text{cMpc}$  and consider them independent to run the neural network predictions. In total, we obtained 10 such sightlines that now have a variable number of pixels in the range 567–603. We normalise the flux to the continuum emission obtained with a PCA technique based on the spectrum to the right side of the Lyman- $\alpha$  line. We then follow [30] and apply a continuum correction factor  $C_{\text{corr}} \approx 0.8$  to match the continuum normalisation used in the SHERWOOD suite. Note that this step was not needed when working with the SQUAD

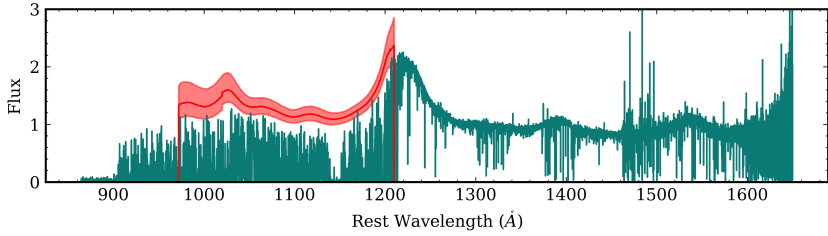


Figure 4.11: The GHOST spectrum for J0306+1853 [84]. The red curve shows the reconstructed continuum together with  $1\sigma$  uncertainties, obtained with a PCA technique based on the spectrum to the right side of the Lyman- $\alpha$  line. Observe the DLA at  $\sim 1150$  Å, which we mask when analysing the Lyman- $\alpha$  forest.

DR1 data, since there the flux was normalised to the peaks.

To recover the  $\Delta_\tau$  field from such skewers, we retrain our Bayesian neural network with the specifications of each skewer. We use the closest redshift snapshot available from the **SHERWOOD** suite, which are [4.5, 4.6, 4.7, 4.8, 4.9], a resolution of FWHM= 10 km/s and SNR= 50. Figure 4.12 shows all 10  $20h^{-1}\text{cMpc}$  portions of the spectrum together with the recovered density field. We split the original spectrum into 10 such skewers of the same length as the ones of the **Sherwood** dataset, and consider them independent. Note that the skewers have a different number of pixels.

We apply our WDM inference pipeline to the 10 segments of the J0306+1853 spectrum. We would like to now combine the reconstructed  $\Delta_\tau$  fields at different redshifts. Since the properties of the fields change with redshift, at each redshift we compute the  $\chi^2$  metric between the reconstructed  $\Delta_\tau$  fields and the **SHERWOOD** model PDFs. Then, we compute the mean  $\chi^2$  across redshifts and use it as the final  $\chi^2$  on which to obtain the WDM particle mass constraints.

Figure 4.13 shows the mean  $\chi^2$  across all redshifts [4.5, 4.6, 4.7, 4.8, 4.9] for all three thermal models, as a function of the WDM particle mass. As expected, the  $\chi^2$  is minimised for the CDM model within each thermal history, and the best-fit thermal model is the **SHERWOOD** CDM reference run. The corresponding  $2\sigma$  constraint, displayed in blue, on the WDM mass is  $m_{\text{WDM}} \gtrsim 3.9$  KeV at  $2\sigma$  confidence.

For reference and completeness, in Figure 4.14 we show the GHOST reconstructed  $\Delta_\tau$  PDF at  $z = 4.9$  obtained from two  $20h^{-1}\text{cMpc}$  skewers compared to the best fit **SHERWOOD** ref CDM at  $z = 4.9$ . We find a good agreement between the model and observed PDF, even when only two skewers are used at each redshift.

In Table 4.2 we list the current state-of-the-art  $2\sigma$  lower bounds on  $m_{\text{WDM}}$  thermal

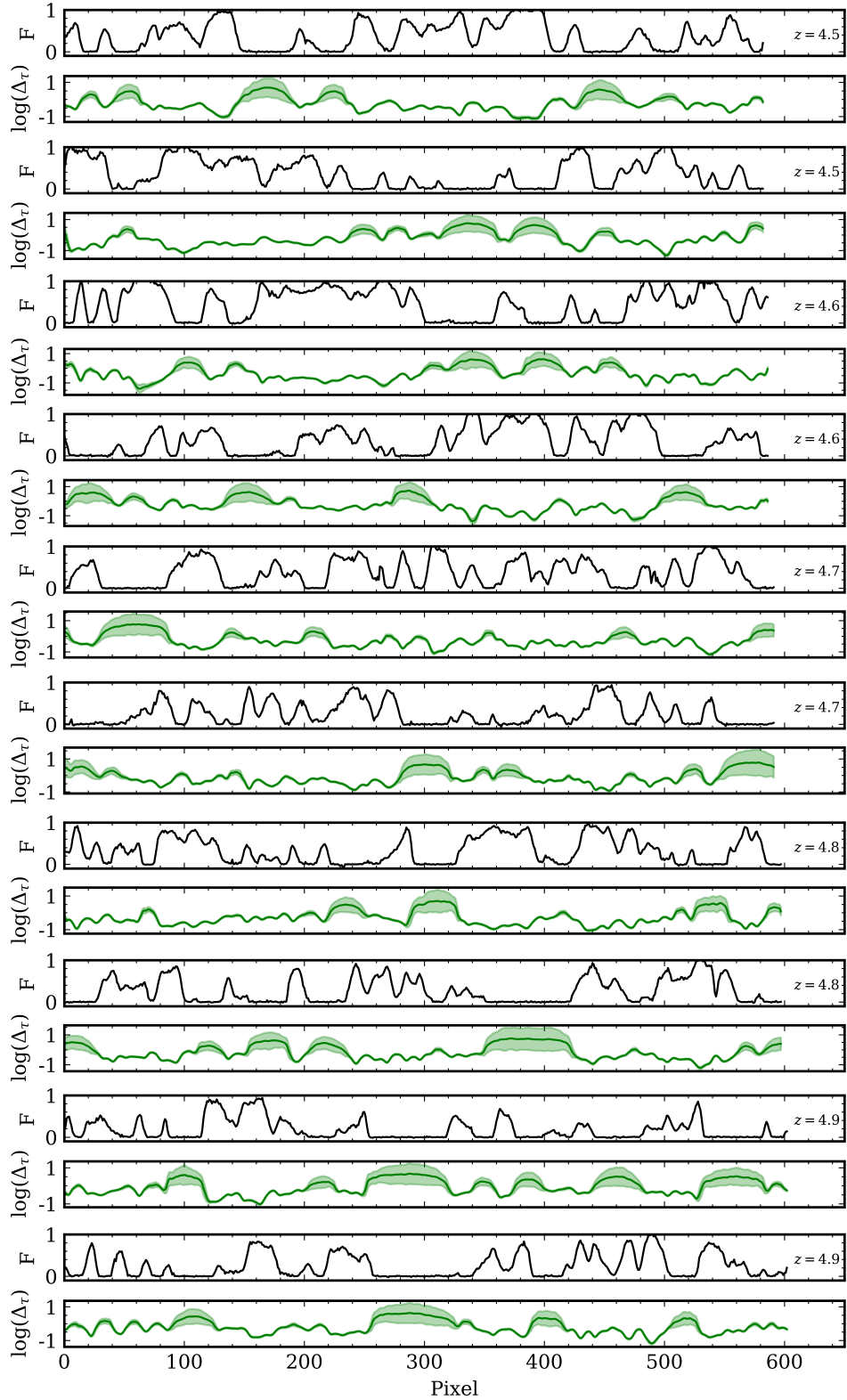


Figure 4.12: All  $20\text{h}^{-1}\text{cMpc}$  portions of the J0306+1853 spectrum together with the recovered density field. We split the original spectrum into 10 such skewers of the same length as the ones of the **SHERWOOD THERMAL** dataset, and consider them independent. For each skewer, we show the closest redshift available in the **SHERWOOD** suite on which the neural network has been trained to obtain the predictions.

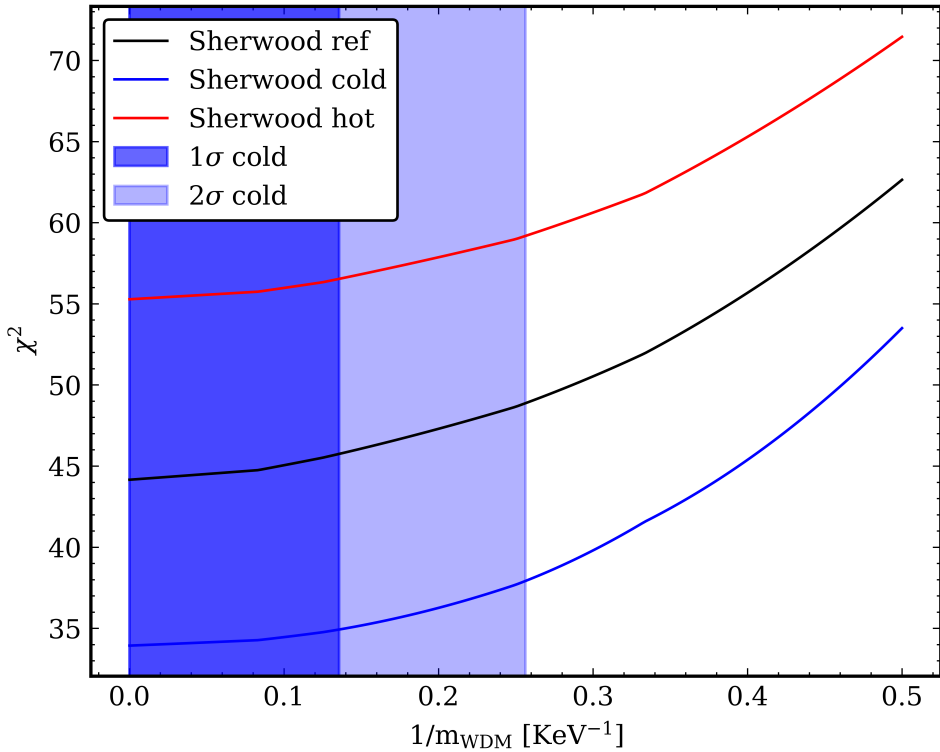


Figure 4.13: The final  $\chi^2$  metric for our GHOST sample, consisting of 10 skewers in the redshifts  $[4.5, 4.6, 4.7, 4.8, 4.9]$ . The  $\chi^2$  shown is the mean across the  $\chi^2$  for each redshift.

relics constraints in the literature obtained from the Lyman- $\alpha$  power spectrum. The previous efforts are based on a Bayesian inference framework to compare the observed power spectrum with the one obtained from simulated data. In contrast, in our work, we do the inference directly on the non-observable density field level. The resulting bounds produced in our work are comparable to previous efforts but with the advantage of requiring substantially less observational data. For reference, in [26], the constraints are obtained from 15 spectra measured along  $327 h^{-1} \text{cMpc}$ , while our GHOST data consists of 10  $20 h^{-1} \text{cMpc}$  skewers, corresponding to 24 times less observed data needed. The tightening of the constraint from the SQUAD DR1 sample to the GHOST sample is also expected since the latter is a larger sample.

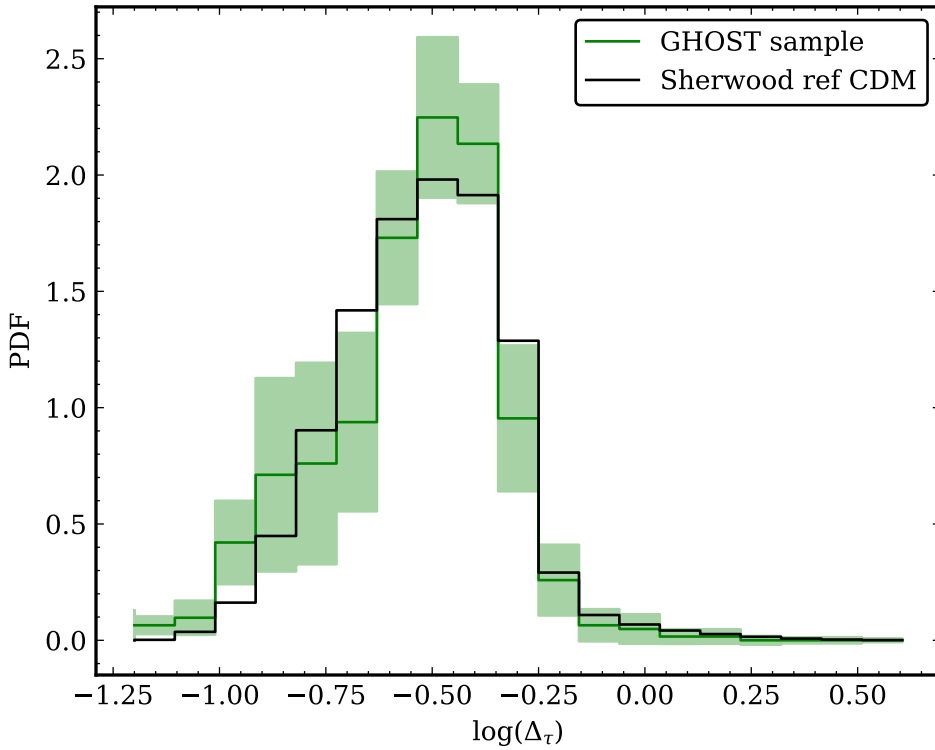


Figure 4.14: The GHOST reconstructed  $\Delta_\tau$  PDF at  $z = 4.9$  obtained from two  $20\text{h}^{-1}\text{cMpc}$  skewers compared to the best fit SHERWOOD ref CDM at  $z = 4.9$ . We find a good agreement between the model and observed PDF, even when only two skewers are used at each redshift.

Table 4.2: List of current state-of-the-art  $2\sigma$  lower bounds on  $m_{\text{WDM}}$  thermal relics constraints in the literature obtained from the Lyman- $\alpha$  power spectrum. We compare them to the results of this work, obtained doing inference directly at the density field level recovered by our Bayesian neural network.

Source	$2\sigma m_{\text{WDM}}$ lower bound [KeV]
Iršič et al. (2024) [26]	4.1
Villasenor et al. (2023) [23]	3.1
This work (SQUAD DR1 sample)	3.8
This work (GHOST spectrum)	3.9

## 4.6 Comparison of the inference pipeline against Information Maximising Neural Networks

The inference pipeline presented so far in this section is based on a simple  $\chi^2$  fit of the  $\Delta_\tau$  recovered PDFs from our fiducial NN model. This pipeline relies on a series of contingent choices, most notably the use of the density PDFs as the summary statistics of the fields. In this section, we explore, in an agnostic way, the possibility of using other summaries different from the  $\Delta_\tau$  PDFs to perform the inference (note that other summaries such as the density power spectrum, curvature, etc., could potentially be used). More concretely, we will introduce Information Maximising Neural Networks (IMNNs) and use them to perform the inference within a Bayesian framework. We then compare the results of this procedure with the inference pipeline discussed in Section 4.

### 4.6.1 Information Maximising Neural Networks

Information Maximising Neural Networks aim at obtaining optimal summaries of data [85]. Neural networks are used to parametrise these summaries in an agnostic way by maximising the information of the summaries concerning the model parameters of interest.

Consider a data-generating procedure depending on some model parameters  $\theta$ , generating data realisations  $d_i(\theta)$  where  $i$  labels a realisation or initial seed of the simulation. We want to obtain a function  $f: d \mapsto x$  that maps each simulation to a summary vector of the same size as  $\theta$ . This is, essentially, a compression algorithm. IMNNs work by transforming the original likelihood of the data, which is a priori not known, into the Gaussian form

$$-2 \ln \mathcal{L}(x|\theta) = (x - \mu(\theta))^T C^{-1} (x - \mu(\theta)), \quad (4.7)$$

where  $C$  is the covariance matrix of the calculated summaries with a set of  $n_s$  simulations, and  $\mu$  is the summary mean depending on the model parameters. The information of the observed summaries with respect to  $\theta$  is then the Fisher information matrix [86]:

$$F_{\alpha\beta} = -\mathbb{E} \left[ \frac{\partial^2}{\partial \theta_\alpha \partial \theta_\beta} \log \mathcal{L}(x; \theta) \middle| \theta \right] = \frac{\partial \mu}{\partial \theta_\alpha} C^{-1} \frac{\partial \mu}{\partial \theta_\beta}, \quad (4.8)$$

whose determinant we note as  $|F|$ . The goal is to obtain summaries that maximise the Fisher information while maintaining a minimum covariance condition to generate

independent summaries. The summaries produced by the network can then be used to perform inference on them. Since the Fisher information is a quantity that depends on the model parameters  $\theta$ , the quantity in Equation 4.8 needs to be evaluated at some fiducial model parameters in order to obtain a numerical result.

IMNNs have been successfully leveraged by the IGM community. Recent papers have explored the possibility of using them to perform IGM thermal parameter inference from Lyman- $\alpha$  skewers, see [87] for instance, where authors find IMNNs to yield tighter and more robust constraints than classical Markov Chain Monte Carlo approaches. Despite these promising results, many challenges arise when using IMNNs on real data, primarily related to the correct identification and interpretation of model parameters.

### 4.6.2 IMNN training and non-linear summaries

In this section, we consider a simple MLP architecture with linear layers followed by PReLU( $\alpha$ ) activation functions and a dropout layer that randomly (with probability  $p$ ) sets to 0 any layer weight during each epoch to prevent over-fitting. The network takes as input a simulated data vector  $d$  and produces a summary vector  $x$  of the same size and the parameter vector  $\theta$ . We use the Adam optimiser to maximise  $|F|$  by minimising the following loss function

$$\mathcal{L}_{IMNN} = -\log(|F|) + \lambda \frac{\mathcal{N}}{\mathcal{N} + \exp(-\mathcal{N})} \mathcal{N}, \quad (4.9)$$

where  $\mathcal{N} = \|C - I\| + \|C^{-1} - I\|$  measure the deviation from independent summaries and  $\lambda$  is a coupling constant. In Equation 4.9, the second term sets a scale for the Fisher information by producing summaries whose covariance approaches the identity matrix. Once this is achieved, the term containing the exponential factor vanishes and the network will maximise  $|F|$ . Note that there is not a unique set of potential optimal summaries. In fact, any bijective function of a sufficient statistic for a certain likelihood is also a sufficient statistic.

For each parameter update in the training procedure, we generate a batch of data at the fiducial parameters  $\theta_f$ . The derivatives in Equation 4.8 are numerically approximated with finite differences by running simulations at parameters  $\theta_f \pm \Delta\theta_\alpha$ , where  $\Delta\theta_\alpha$  is a small parameter variation, and then calculating

$$\frac{\partial x}{\partial \theta_\alpha} = \frac{x(d(\theta_f + \Delta\theta_\alpha)) - x(d(\theta_f - \Delta\theta_\alpha))}{2\Delta\theta_\alpha}. \quad (4.10)$$

We then calculate  $C$ , the covariance of the summaries at fiducial parameters, and use it to compute the Fisher information in Equation 4.8 and the loss function in Equation 4.9. Note that, since the covariance matrix and the derivative in the Fisher information matrix are computed at the data summaries, they implicitly depend on the NN parameters.

### 4.6.3 Summarising a Gaussian signal

We implement IMNNs using Pytorch<sup>1</sup>, a deep-learning Python framework. We test the implementation first by exploring its behaviour on a toy model, where we generate random samples from a Gaussian distribution  $\mathcal{N}(\mu, \sigma)$ . The sufficient statistic for the model parameters  $\theta = (\mu, \sigma)$  are, in this case, the sample mean and standard deviation:

$$\hat{\mu} = \frac{1}{n_d} \sum d_i \quad \hat{\sigma}^2 = \frac{1}{n_d - 1} \sum (d_i - \hat{\mu})^2. \quad (4.11)$$

Note that the statistic for  $\sigma$  is non-linear. For this example, we select fiducial parameters  $\theta_f = (\mu = 0, \sigma = 1)$  and  $\Delta\theta = (0.1, 0.1)$  and generate random fields with 100 pixels. In total, 5000 fields are generated for each parameter set, including a validation dataset. Note that testing the network performance in the validation dataset is crucial in performing early stopping during the training process. Indeed, since the training dataset is limited, it will contain spurious correlations that the network will use to infer a higher information than expected. By stopping the training when the network information on the validation set saturates, we can avoid this problem. We use a simple architecture, with layers [128, 128, 128, 2], learning rate of 0.001, dropout rate of  $p = 0.5$ , and batch size of 500. Observe the training evolution in Figure 4.15, where we show  $|F|$  and  $\|C - I\| + \|C + I\|$  as a function of the epoch for the training and validation sets. As can be seen, the validation information quickly saturates in  $\sim 100$  epochs, and then slowly decreases as the network over-fits.

To better interpret the network output and to understand its behaviour, we generate samples of the same size with the zero mean, but a standard deviation randomly sampled from  $(0, 12)$ . We then compute the exact statistic (the sample standard deviation) and plot it against the second IMNN summary output. The result is Figure 4.16. Observe that the exact statistic in the  $x$ -axis is highly correlated to the network summary in the  $y$ -axis. Since the relation between the two quantities is clearly bijective, the model has successfully learnt to extract all the possible information for the field covariance. The

---

<sup>1</sup><https://pytorch.org>

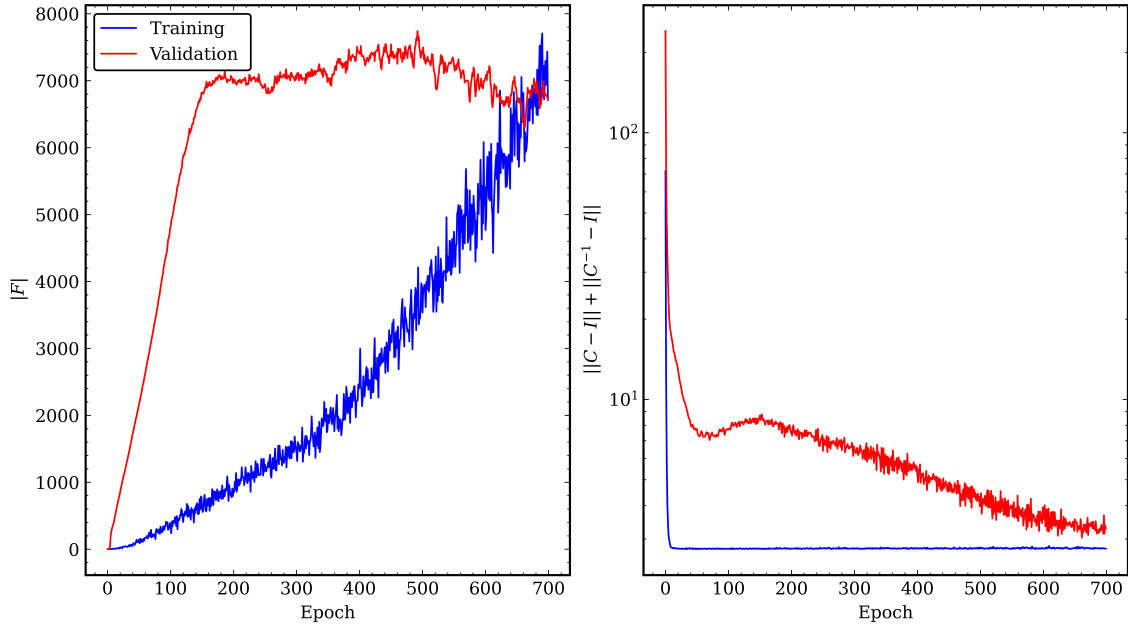


Figure 4.15:  $|F|$  and  $\|C - I\| + \|C^{-1} - I\|$  as a function of the epoch for the training and validation sets during the training of the IMNN on a normal field. The goal is to find summaries to optimally extract information about the mean and variance of the field.

natural scatter is due to having a simple NN model.

Note that the network has not seen any normal field with such variances  $\sigma \in (0, 12)$  during training, yet it can extract the correct summary. This is of crucial importance since it means that we could use the IMNN summaries to do inference on a field with parameter values slightly different from the fiducial ones used during training.

To conclude the exploration of this toy model, we use the network to perform Bayesian inference. We implement a simple Approximate Bayesian Computation (ABC) [88] algorithm that obtains approximate posterior samples from a given set of prior samples and observed data. As the observed data, we take 50 Gaussian fields simulated at fiducial parameter ( $\mu = 0, \sigma = 1$ ) values. As priors, we take 5000 samples from a non-informative uniform distribution in  $(-5, 5)$  for  $\mu$  and  $(0, 10)$  for  $\sigma$ . The ABC rejection algorithm is described in Algorithm 3.

In Figure 4.17 we show the posterior samples and Gaussian Kernel Density Estimation (KDE) for the distributions of  $\mu$  and  $\sigma$ . The dashed vertical lines show the true parameter values. As expected, and even with a non-informative prior, the IMNN summary contains sufficient information to produce a tight posterior around the true model parameters. Note that the posterior scatter on the non-linear summary  $\sigma$  is larger than

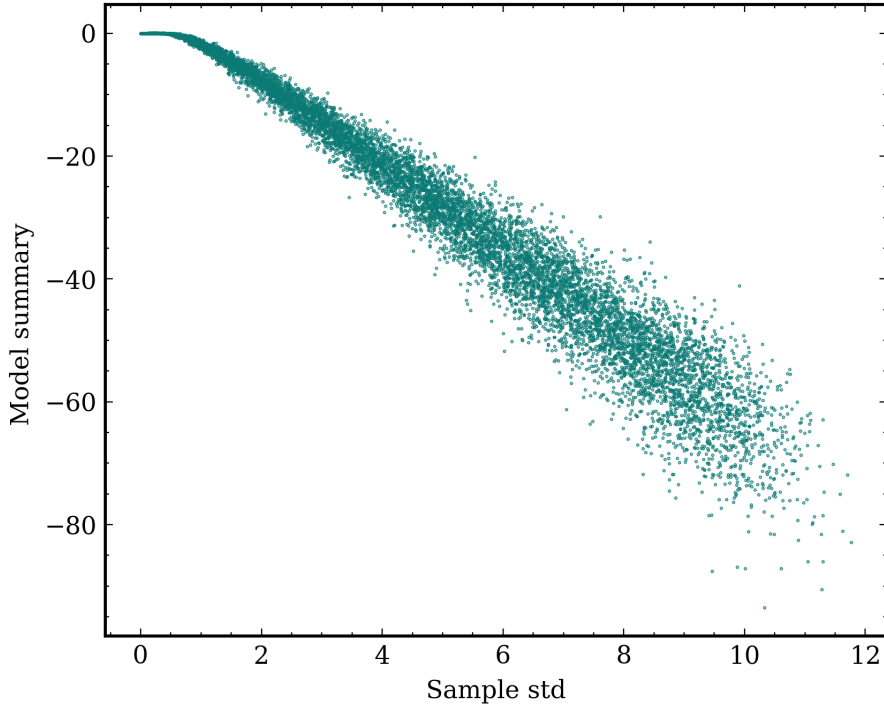


Figure 4.16: The IMNN summary plotted against the exact sufficient statistic for the standard deviation using multiple samples with  $\sigma \in (0, 12)$ .

---

**Algorithm 3** Approximate Bayesian Computation Rejection Algorithm

---

```

1: Input: Observed data  $\mathbf{y}$ , threshold  $\epsilon$ , number of simulations  $N$ , prior distribution
 $\pi(\theta)$ 
2: Output: Accepted parameter values  $\{\theta_i\}_{i=1}^M$ 
3: Initialize  $M \leftarrow 0$ 
4: for  $i = 1$  to  $N$  do
5:   Sample  $\theta^*$  from the prior distribution  $\pi(\theta)$ 
6:   Simulate data  $\mathbf{y}^*$  from the model using  $\theta^*$ 
7:   if  $d(\mathbf{y}, \mathbf{y}^*) \leq \epsilon$  then
8:     Accept  $\theta^*$ :  $\theta_{M+1} \leftarrow \theta^*$ 
9:     Increment  $M \leftarrow M + 1$ 
10:  end if
11: end for
12: return  $\{\theta_i\}_{i=1}^M$ 

```

---

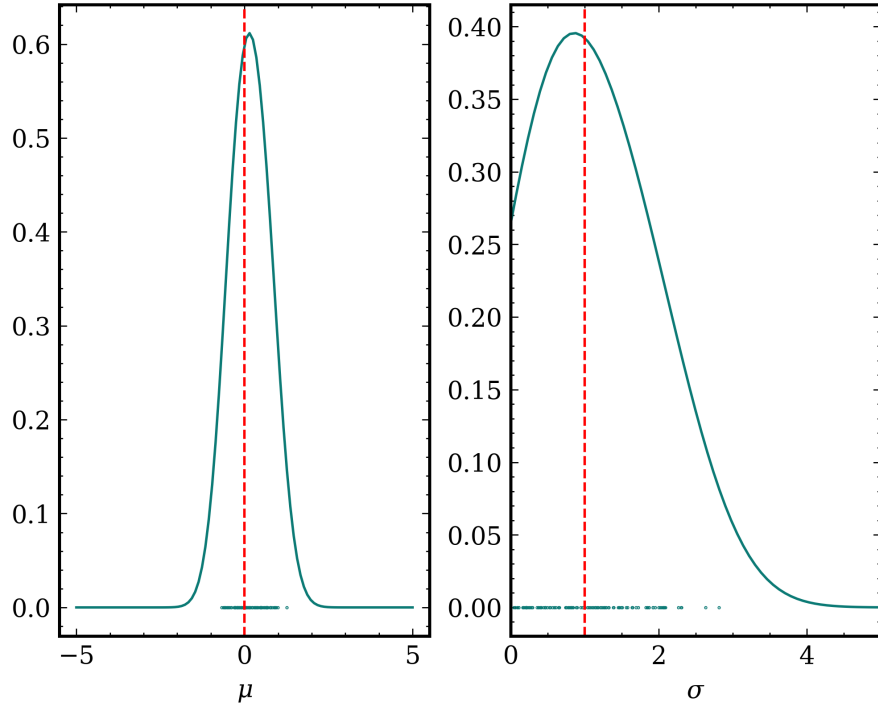


Figure 4.17: Posterior samples and KDE for the ABC rejection algorithm applied to the normal toy model, where we infer the mean and variance of a Gaussian field with flat priors and the summaries output of an IMNN. The dashed vertical lines show the true parameter values.

on the linear summary  $\mu$ .

#### 4.6.4 IMNN inference results on WDM masses

We can now deploy a simple IMNN as an alternative way of constraining WDM models. We follow Section 4.6.3 and consider a similar architecture but now with 4 dense layers of size [512, 512, 256, 2]. As input to the NN, we consider Lyman- $\alpha$  flux skewers. Since in flux space, the skewers have many simulation-specific and prominent features that can be picked up by a NN, we work in Fourier space. More precisely, the input to the network is

$$\sqrt{k}|\delta_F(k)|, \quad (4.12)$$

where  $\delta_F$  is the flux contrast of the skewer. We use the **SHERWOOD** simulation suite with varied WDM mass to train the IMNN. Note that this means that we are assuming that WDM is the only model parameter affecting the Lyman- $\alpha$  forest property. We ignore thermal parameter variations for this demonstration. We train our model on the fiducial

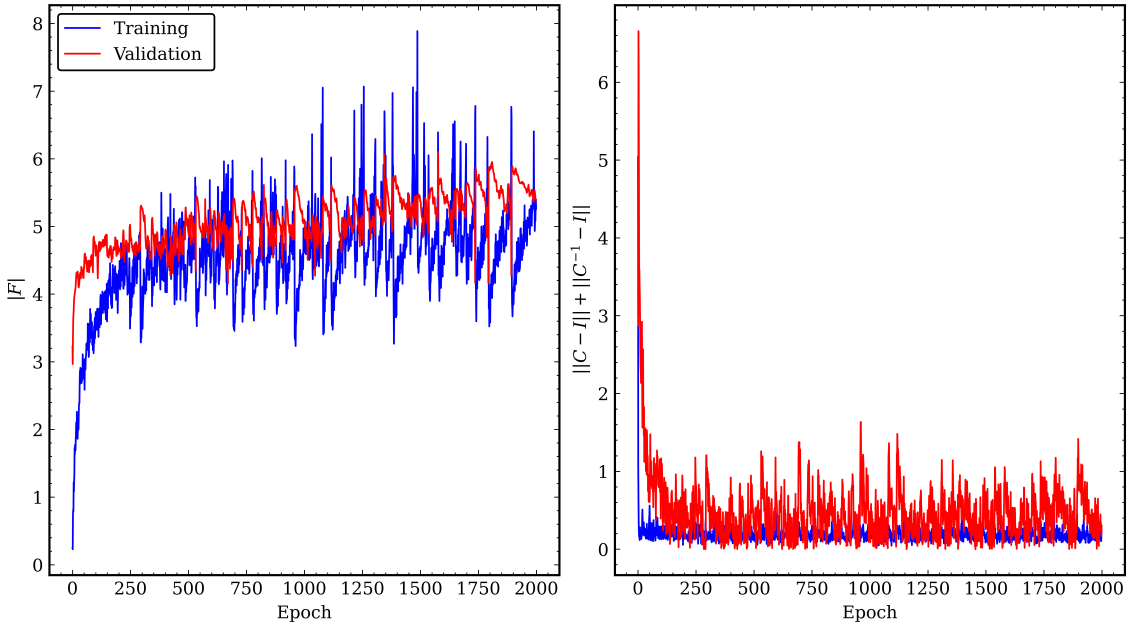


Figure 4.18:  $|F|$  and  $\|C - I\| + \|C^{-1} - I\|$  as a function of the epoch for the training and validation sets during the training of the IMNN on the **SHERWOOD** dataset Lyman- $\alpha$  skewers.

CDM mass corresponding to 0 KeV $^{-1}$  and use the WDM3 model corresponding to 1/3 KeV $^{-1}$  to calculate the summary derivatives. The choice of WDM3 is due to the flux skewers showing sufficient variation concerning CDM.

In Figure 4.18 we show the training progress of the IMNN as a function of the epoch. The information extracted on the validation split quickly saturates at  $\sim 250$  epochs. The network can learn a map from Lyman- $\alpha$  skewers in Fourier space into a one-dimensional parameter space. Since the **SHERWOOD** suite has a fixed number of simulations, interpreting the network output summaries is a challenging task.

In Figure 4.19a) we show the summaries of the trained IMNN for all the available **SHERWOOD** Lyman- $\alpha$  skewers in Fourier space. Observe how the summaries show a large scatter for every model, corresponding to the large simulation variability within each skewer. However, the mean summaries show a clear bijective trend, manifesting that the IMNN has learnt an informative summary. Note that this can be interpreted as the necessity of a large number of observed samples when constraining WDM models. We use the IMNN summaries to perform an inference test and obtain a Bayesian posterior as follows. First, we select 50 CDM skewers from the validation dataset and obtain their corresponding summaries by passing them through the IMNN. We now use all validation skewers from the **SHERWOOD** suite and obtain their summaries. We use the ABC rejection

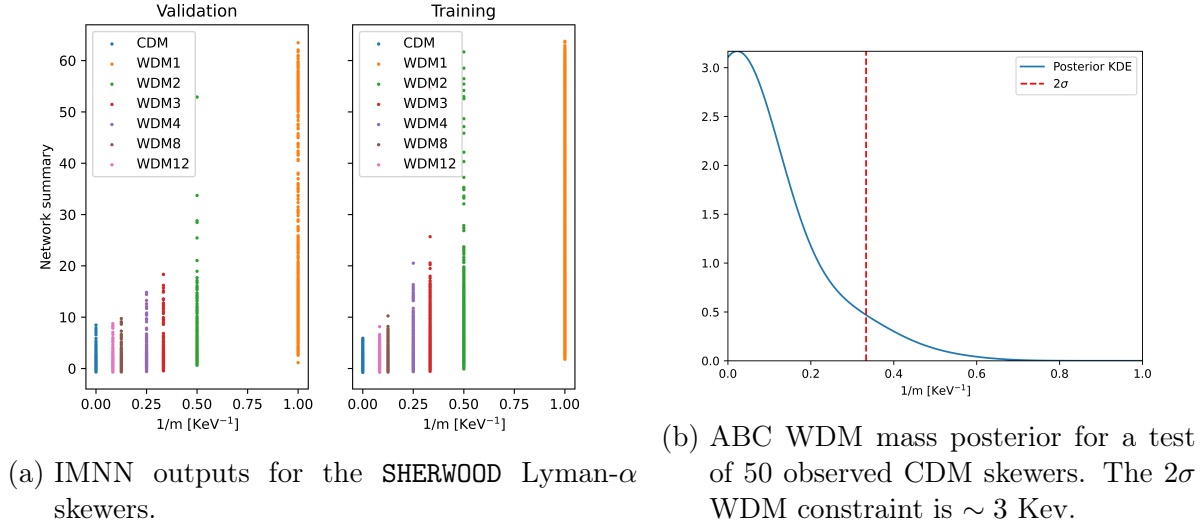


Figure 4.19

Algorithm 3 to generate to posterior distribution in Figure 4.19b). The  $2\sigma$  limit for the WDM mass is  $\sim 3$  KeV. Recall that this is a comparable constraint to the one obtained in Section 4.4. We interpret this not only as a robustness sign of our original pipeline involving a  $\chi^2$  fit the  $\Delta_\tau$  PDFs, but most notably as a sign that it optimally extracts the majority of the information of the Lyman- $\alpha$  skewers with respect to the WDM mass parameter.

## 5 Conclusions

In this work, we have explored the potential of novel machine learning techniques to constrain warm dark matter in the cosmological context. We began in Section 1 with the basics of the current cosmological paradigm. We highlighted the importance of the intergalactic medium in the formation and evolution of structures. Then, we elaborated on how the Lyman- $\alpha$  forest observed on the spectra of quasars can serve as an efficient probe of the state of the IGM, allowing for the extraction of valuable information. We noted the relevance of dark matter in the  $\Lambda$ CDM model and discussed the key concepts related to it, such as the free-streaming length. We then understood the motivation behind considering alternative models to CDM, such as warm dark matter. Since WDM affects the matter distribution in the IGM, the Lyman- $\alpha$  forest can provide information on its nature. To understand the impact of WDM on the Lyman- $\alpha$  forest, we turned our attention in Section 2 to cosmological simulations. We introduced the key points on how such hydrodynamical simulations are performed and introduced the **SHERWOOD** simulation suite, which is at the core of this work. Afterwards, we used the **SHERWOOD** raw data to compute simulated Lyman- $\alpha$  skewers and explored the impact of peculiar velocities and warm dark matter on its structure. For the latter, we introduced two statistics, the power spectrum and the probability distribution function, to understand the flux and density field from a statistical point of view.

Armed with these preliminaries, we were set to start the task of detecting the signatures of WDM in the IGM density field in Section 3. This involves transforming the Lyman- $\alpha$  information into density information. For this highly non-trivial task, we resorted to neural networks. We motivated their growing use in astronomy and introduced their basic working principles. Then, we focused on how to build a robust Bayesian neural network to recover the optical depth-weighted density from the Lyman- $\alpha$  forest flux. Bayesian networks naturally allow for a quantification of the prediction uncertainty, which is especially relevant when the real data is contaminated by observational effects, such as noise. We discussed the training procedure, based on the **SHERWOOD** suite, and the hyper-parameter optimisation of the neural network. We then evaluated the accu-

---

racy of the trained neural network on the validation data, which is as high 79% ( $1\sigma$ ), and explored the accuracy of the recovered statistics on the density field and their respective uncertainties. Lastly, we discussed some aspects of the model’s interpretability, illustrated by saliency maps and pruning. All in all, in Section 3 we find that it is viable to recover the  $\Delta_\tau$  density field from Lyman- $\alpha$  skewers for different WDM models and IGM temperatures, showing that the thermal history and WDM models are not completely degenerate.

In Section 4 we leverage our machine learning-recovered density fields to constrain WDM. We build an efficient statistical inference pipeline that fits the recovered  $\Delta_\tau$  PDF to the PDF for each WDM model in the **SHERWOOD** suite and generates constraints on the allowed WDM particle mass. We extensively test the robustness of this pipeline using a set of CDM cosmological simulations obtained from **Nyx**, an alternative hydro-dynamical code based on the Lagrangian framework. For a set of 450 **SHERWOOD** CDM simulated skewers with  $SNR = 30$  and a resolution of 6 km/s per pixel, we find a lower bound on the WDM particle mass of  $\sim 10$  KeV at  $2\sigma$  confidence. Once successfully tested on simulated data, we apply our inference pipeline to real observational from the UltraViolet-Visual Echelle Spectrograph at the Very Large Telescope and the Gemini High-resolution Optical SpecTrograph at the Gemini South Telescope. The two independent datasets consist of 6 quasar SQUAD DR1 Lyman- $\alpha$  forests at  $z = 4.4$ , and a single target quasar with a forest spanning the redshift range  $\sim 4.5 - 4.9$ , respectively. We obtain  $2\sigma$  constraints of 3.8 and 3.9 KeV for both of those datasets. Our findings are comparable to state-of-the-art techniques, but require significantly less observed data, highlighting the efficiency of machine learning techniques in extracting information from complex data. We conclude our work by testing a statistic-independent alternative approach using Information Maximising Neural Networks to test whether our constraints can be tightened, but find no significant improvement.

Our work aligns with the ground-breaking introduction of machine learning methods in astronomy and astrophysics in recent years and highlights how such approaches can be used to efficiently extract information from the Lyman- $\alpha$  forest. Future efforts based on this approach can be targeted at jointly constraining multiple physical parameters of interest besides WDM, such as the thermal parameters of the IGM, using a finner grid of simulations. Significant improvement can also be made in designing a fully Bayesian inference method.

# Bibliography

- [1] Sean M. Carroll. *Spacetime and Geometry: An Introduction to General Relativity*. Cambridge University Press, 2019.
- [2] Planck Collaboration, P. A. R. Ade, N. Aghanim, C. Armitage-Caplan, M. Arnaud, et al. “Planck 2013 results. XVI. Cosmological parameters”. In: *APP* 571, A16 (Nov. 2014), A16. DOI: 10.1051/0004-6361/201321591. arXiv: 1303.5076 [astro-ph.CO].
- [3] Houjun Mo, Frank van den Bosch, and Simon White. *Galaxy Formation and Evolution*. Cambridge University Press, May 2010. ISBN: 9780511807244. DOI: 10.1017/cbo9780511807244. URL: <http://dx.doi.org/10.1017/CBO9780511807244>.
- [4] Robert H. Becker, Xiaohui Fan, Richard L. White, Michael A. Strauss, Vijay K. Narayanan, et al. “Evidence for Reionization at  $z \sim 6$ : Detection of a Gunn-Peterson Trough in a  $z = 6.28$  Quasar”. In: *The Astronomical Journal* 122.6 (Dec. 2001), pp. 2850–2857. ISSN: 0004-6256. DOI: 10.1086/324231. URL: <http://dx.doi.org/10.1086/324231>.
- [5] Ian D. McGreer, Andrei Mesinger, and Valentina D’Odorico. “Model-independent evidence in favour of an end to reionization by  $z \approx 6$ ”. In: *MNRAS* 447.1 (Feb. 2015), pp. 499–505. DOI: 10.1093/mnras/stu2449. arXiv: 1411.5375 [astro-ph.CO].
- [6] James E. Gunn and Bruce A. Peterson. “On the Density of Neutral Hydrogen in Intergalactic Space.” In: *APJ* 142 (Nov. 1965), pp. 1633–1636. DOI: 10.1086/148444.
- [7] T. Roy Choudhury, R. Srianand, and T. Padmanabhan. “Semianalytic Approach to Understanding the Distribution of Neutral Hydrogen in the Universe: Comparison of Simulations with Observations”. In: *The Astrophysical Journal* 559.1 (Sept. 2001), pp. 29–40. ISSN: 1538-4357. DOI: 10.1086/322327. URL: <http://dx.doi.org/10.1086/322327>.

- [8] Michael Rauch. "THE LYMAN ALPHA FOREST IN THE SPECTRA OF QUASISTELLAR OBJECTS". In: *Annual Review of Astronomy and Astrophysics* 36.1 (Sept. 1998), pp. 267–316. ISSN: 1545-4282. DOI: 10.1146/annurev.astro.36.1.267. URL: <http://dx.doi.org/10.1146/annurev.astro.36.1.267>.
- [9] Pablo Villanueva-Domingo, Olga Mena, and Sergio Palomares-Ruiz. "A Brief Review on Primordial Black Holes as Dark Matter". In: *Frontiers in Astronomy and Space Sciences* 8 (May 2021). ISSN: 2296-987X. DOI: 10.3389/fspas.2021.681084. URL: <http://dx.doi.org/10.3389/fspas.2021.681084>.
- [10] Julio F. Navarro, Carlos S. Frenk, and Simon D. M. White. "The Structure of Cold Dark Matter Halos". In: *The Astrophysical Journal* 462 (May 1996), p. 563. ISSN: 1538-4357. DOI: 10.1086/177173. URL: <http://dx.doi.org/10.1086/177173>.
- [11] W. J. G. de Blok, F. Walter, E. Brinks, C. Trachternach, S-H. Oh, and R. C. Kennicutt. "HIGH-RESOLUTION ROTATION CURVES AND GALAXY MASS MODELS FROM THINGS". In: *The Astronomical Journal* 136.6 (Nov. 2008), pp. 2648–2719. ISSN: 1538-3881. DOI: 10.1088/0004-6256/136/6/2648. URL: <http://dx.doi.org/10.1088/0004-6256/136/6/2648>.
- [12] N. Dalal and C. S. Kochanek. "Direct Detection of Cold Dark Matter Substructure". In: *The Astrophysical Journal* 572.1 (June 2002), pp. 25–33. ISSN: 1538-4357. DOI: 10.1086/340303. URL: <http://dx.doi.org/10.1086/340303>.
- [13] L. Van Waerbeke, Y. Mellier, and H. Hoekstra. "Dealing with systematics in cosmic shear studies: New results from the VIRMOS-Descart survey". In: *Astronomy and Astrophysics* 429.1 (Dec. 2004), pp. 75–84. ISSN: 1432-0746. DOI: 10.1051/0004-6361:20041513. URL: <http://dx.doi.org/10.1051/0004-6361:20041513>.
- [14] Daniel J. Eisenstein, Idit Zehavi, David W. Hogg, Roman Scoccimarro, Michael R. Blanton, et al. "Detection of the Baryon Acoustic Peak in the Large-Scale Correlation Function of SDSS Luminous Red Galaxies". In: *The Astrophysical Journal* 633.2 (Nov. 2005), pp. 560–574. ISSN: 1538-4357. DOI: 10.1086/466512. URL: <http://dx.doi.org/10.1086/466512>.
- [15] Ben Moore. "Evidence against dissipation-less dark matter from observations of galaxy haloes". In: *Nature* 370.6491 (Aug. 1994), pp. 629–631. ISSN: 1476-4687. DOI: 10.1038/370629a0. URL: <http://dx.doi.org/10.1038/370629a0>.

## Bibliography

---

- [16] Michael Boylan-Kolchin, James S. Bullock, and Manoj Kaplinghat. “Too big to fail? The puzzling darkness of massive Milky Way subhaloes”. In: *Monthly Notices of the Royal Astronomical Society: Letters* 415.1 (July 2011), pp. L40–L44. ISSN: 1745-3925. DOI: 10.1111/j.1745-3933.2011.01074.x. URL: <http://dx.doi.org/10.1111/j.1745-3933.2011.01074.x>.
- [17] David H. Weinberg, James S. Bullock, Fabio Governato, Rachel Kuzio de Naray, and Annika H. G. Peter. “Cold dark matter: Controversies on small scales”. In: *Proceedings of the National Academy of Sciences* 112.40 (Feb. 2015), pp. 12249–12255. ISSN: 1091-6490. DOI: 10.1073/pnas.1308716112. URL: <http://dx.doi.org/10.1073/pnas.1308716112>.
- [18] M. Vogelsberger, S. Genel, V. Springel, P. Torrey, D. Sijacki, D. Xu, G. Snyder, S. Bird, D. Nelson, and L. Hernquist. “Properties of galaxies reproduced by a hydrodynamic simulation”. In: *Nature* 509.7499 (May 2014), pp. 177–182. ISSN: 1476-4687. DOI: 10.1038/nature13316. URL: <http://dx.doi.org/10.1038/nature13316>.
- [19] David N. Spergel and Paul J. Steinhardt. “Observational Evidence for Self-Interacting Cold Dark Matter”. In: *Physical Review Letters* 84.17 (Apr. 2000), pp. 3760–3763. ISSN: 1079-7114. DOI: 10.1103/physrevlett.84.3760. URL: <http://dx.doi.org/10.1103/PhysRevLett.84.3760>.
- [20] Wayne Hu, Rennan Barkana, and Andrei Gruzinov. “Fuzzy Cold Dark Matter: The Wave Properties of Ultralight Particles”. In: *Physical Review Letters* 85.6 (Aug. 2000), pp. 1158–1161. ISSN: 1079-7114. DOI: 10.1103/physrevlett.85.1158. URL: <http://dx.doi.org/10.1103/PhysRevLett.85.1158>.
- [21] Steen Hannestad and Georg Raffelt. “Cosmological mass limits on neutrinos, axions, and other light particles”. In: *Journal of Cosmology and Astroparticle Physics* 2004.04 (Apr. 2004), pp. 008–008. ISSN: 1475-7516. DOI: 10.1088/1475-7516/2004/04/008. URL: <http://dx.doi.org/10.1088/1475-7516/2004/04/008>.
- [22] Matteo Viel, Julien Lesgourgues, Martin G. Haehnelt, Sabino Matarrese, and Antonio Riotto. “Constraining warm dark matter candidates including sterile neutrinos and light gravitinos with WMAP and the Lyman-alpha forest”. In: *Physical Review D* 71.6 (Mar. 2005). ISSN: 1550-2368. DOI: 10.1103/physrevd.71.063534. URL: <http://dx.doi.org/10.1103/PhysRevD.71.063534>.

- 
- [23] Bruno Villasenor, Brant Robertson, Piero Madau, and Evan Schneider. “New constraints on warm dark matter from the Lyman-alpha forest power spectrum”. In: *Physical Review D* 108.2 (July 2023). ISSN: 2470-0029. DOI: 10.1103/physrevd.108.023502. URL: <http://dx.doi.org/10.1103/PhysRevD.108.023502>.
  - [24] Richard Massey, Thomas Kitching, and Johan Richard. “The dark matter of gravitational lensing”. In: *Reports on Progress in Physics* 73.8 (July 2010), p. 086901. ISSN: 1361-6633. DOI: 10.1088/0034-4885/73/8/086901. URL: <http://dx.doi.org/10.1088/0034-4885/73/8/086901>.
  - [25] Francesca Calore, Pasquale Dario Serpico, and Bryan Zaldívar. “Dark matter constraints from dwarf galaxies: a data-driven analysis”. In: *Journal of Cosmology and Astroparticle Physics* 2018.10 (Oct. 2018), pp. 029–029. ISSN: 1475-7516. DOI: 10.1088/1475-7516/2018/10/029. URL: <http://dx.doi.org/10.1088/1475-7516/2018/10/029>.
  - [26] Vid Iršič, Matteo Viel, Martin G. Haehnelt, James S. Bolton, Margherita Molaro, et al. “Unveiling dark matter free streaming at the smallest scales with the high redshift Lyman-alpha forest”. In: *PRD* 109.4, 043511 (Feb. 2024), p. 043511. DOI: 10.1103/PhysRevD.109.043511. arXiv: 2309.04533 [astro-ph.CO].
  - [27] Fahad Nasir, Prakash Gaikwad, Frederick B. Davies, James S. Bolton, Ewald Puchwein, and Sarah E. I. Bosman. *Deep Learning the Intergalactic Medium using Lyman-alpha Forest at  $4 \leq z \leq 5$* . 2024. arXiv: 2404.05794 [astro-ph.CO].
  - [28] Sarah E I Bosman, Frederick B Davies, George D Becker, Laura C Keating, Rebecca L Davies, et al. “Hydrogen reionization ends by  $z = 5.3$ : Lyman-alpha optical depth measured by the XQR-30 sample”. In: *Monthly Notices of the Royal Astronomical Society* 514.1 (June 2022), pp. 55–76. ISSN: 1365-2966. DOI: 10.1093/mnras/stac1046. URL: <http://dx.doi.org/10.1093/mnras/stac1046>.
  - [29] Lars Hernquist, Neal Katz, David H. Weinberg, and Jordi Miralda-Escudé. “The Lyman-Alpha Forest in the Cold Dark Matter Model”. In: *The Astrophysical Journal* 457.2 (Feb. 1996). ISSN: 0004-637X. DOI: 10.1086/309899. URL: <http://dx.doi.org/10.1086/309899>.
  - [30] James S. Bolton, Ewald Puchwein, Debora Sijacki, Martin G. Haehnelt, Tae-Sun Kim, Avery Meiksin, John A. Regan, and Matteo Viel. “The Sherwood simulation suite: overview and data comparisons with the Lyman-alpha forest at redshifts  $2 < z < 5$ ”. In: *Monthly Notices of the Royal Astronomical Society* 464.1 (Sept.

- 2016), pp. 897–914. ISSN: 1365-2966. DOI: 10.1093/mnras/stw2397. URL: <http://dx.doi.org/10.1093/mnras/stw2397>.
- [31] Volker Springel. “The cosmological simulation code gadget-2”. In: *Monthly Notices of the Royal Astronomical Society* 364.4 (Dec. 2005), pp. 1105–1134. ISSN: 1365-2966. DOI: 10.1111/j.1365-2966.2005.09655.x. URL: <http://dx.doi.org/10.1111/j.1365-2966.2005.09655.x>.
- [32] Francesco Haardt and Piero Madau. “RADIATIVE TRANSFER IN A CLUMPY UNIVERSE. IV. NEW SYNTHESIS MODELS OF THE COSMIC UV/X-RAY BACKGROUND”. In: *The Astrophysical Journal* 746.2 (Feb. 2012), p. 125. ISSN: 1538-4357. DOI: 10.1088/0004-637X/746/2/125. URL: <http://dx.doi.org/10.1088/0004-637X/746/2/125>.
- [33] Zarija Lukić, Casey W. Stark, Peter Nugent, Martin White, Avery A. Meiksin, and Ann Almgren. “The Lyman-alpha forest in optically thin hydrodynamical simulations”. In: *Monthly Notices of the Royal Astronomical Society* 446.4 (Dec. 2014), pp. 3697–3724. ISSN: 0035-8711. DOI: 10.1093/mnras/stu2377. URL: <http://dx.doi.org/10.1093/mnras/stu2377>.
- [34] Thorsten Tepper García. “Voigt profile fitting to quasar absorption lines: an analytic approximation to the Voigt-Hjerting function: A new method to compute Voigt profiles”. In: *Monthly Notices of the Royal Astronomical Society* 369.4 (June 2006), pp. 2025–2035. ISSN: 0035-8711. DOI: 10.1111/j.1365-2966.2006.10450.x. URL: <http://dx.doi.org/10.1111/j.1365-2966.2006.10450.x>.
- [35] Tomáš Šoltinskí, James S Bolton, Nina Hatch, Martin G Haehnelt, Laura C Keating, Girish Kulkarni, Ewald Puchwein, Jonathan Chardin, and Dominique Aubert. “The detectability of strong 21 centimetre forest absorbers from the diffuse intergalactic medium in late reionisation models”. In: *Monthly Notices of the Royal Astronomical Society* (July 2021). ISSN: 1365-2966. DOI: 10.1093/mnras/stab1830. URL: <http://dx.doi.org/10.1093/mnras/stab1830>.
- [36] J. Schaye, T. Theuns, A. Leonard, and G. Efstathiou. “Measuring the equation of state of the intergalactic medium”. In: *Monthly Notices of the Royal Astronomical Society* 310.1 (Nov. 1999), pp. 57–70. ISSN: 1365-2966. DOI: 10.1046/j.1365-8711.1999.02956.x. URL: <http://dx.doi.org/10.1046/j.1365-8711.1999.02956.x>.

- 
- [37] David Freedman and Persi Diaconis. “On the histogram as a density estimator:L 2 theory”. In: *Zeitschrift für Wahrscheinlichkeitstheorie und Verwandte Gebiete* 57.4 (Dec. 1981), pp. 453–476. ISSN: 1432-2064. DOI: 10.1007/bf01025868. URL: <http://dx.doi.org/10.1007/BF01025868>.
  - [38] Patrick McDonald, Uroš Seljak, Scott Burles, David J. Schlegel, David H. Weinberg, et al. “The Ly-alpha Forest Power Spectrum from the Sloan Digital Sky Survey”. In: *The Astrophysical Journal Supplement Series* 163.1 (Mar. 2006), pp. 80–109. ISSN: 1538-4365. DOI: 10.1086/444361. URL: <http://dx.doi.org/10.1086/444361>.
  - [39] Corentin Ravoux, Marie Lynn Abdul Karim, Eric Armengaud, Michael Walther, Naim Göksel Karaçaylı, et al. “The Dark Energy Spectroscopic Instrument: one-dimensional power spectrum from first Ly-alpha forest samples with Fast Fourier Transform”. In: *Monthly Notices of the Royal Astronomical Society* 526.4 (Oct. 2023), pp. 5118–5140. ISSN: 1365-2966. DOI: 10.1093/mnras/stad3008. URL: <http://dx.doi.org/10.1093/mnras/stad3008>.
  - [40] Elisa Boera, George D. Becker, James S. Bolton, and Fahad Nasir. “Revealing Reionization with the Thermal History of the Intergalactic Medium: New Constraints from the Ly-alpha Flux Power Spectrum”. In: *The Astrophysical Journal* 872.1 (Feb. 2019), p. 101. ISSN: 1538-4357. DOI: 10.3847/1538-4357/aafee4. URL: <http://dx.doi.org/10.3847/1538-4357/aafee4>.
  - [41] George D. Becker, Paul C. Hewett, Gábor Worseck, and J. Xavier Prochaska. “A refined measurement of the mean transmitted flux in the Ly-alpha forest over  $2 < z < 5$  using composite quasar spectra”. In: *Monthly Notices of the Royal Astronomical Society* 430.3 (Feb. 2013), pp. 2067–2081. ISSN: 1365-2966. DOI: 10.1093/mnras/stt031. URL: <http://dx.doi.org/10.1093/mnras/stt031>.
  - [42] Yann LeCun, Yoshua Bengio, and Geoffrey Hinton. “Deep learning”. In: *Nature* 521.7553 (May 2015), pp. 436–444. ISSN: 1476-4687. DOI: 10.1038/nature14539. URL: <http://dx.doi.org/10.1038/nature14539>.
  - [43] Xia Zhao, Limin Wang, Yufei Zhang, Xuming Han, Muhammet Deveci, and Milan Parmar. “A review of convolutional neural networks in computer vision”. In: *Artificial Intelligence Review* 57.4 (Mar. 2024). ISSN: 1573-7462. DOI: 10.1007/s10462-024-10721-6. URL: <http://dx.doi.org/10.1007/s10462-024-10721-6>.

## Bibliography

---

- [44] Greg Van Houdt, Carlos Mosquera, and Gonzalo Nápoles. “A review on the long short-term memory model”. In: *Artificial Intelligence Review* 53.8 (May 2020), pp. 5929–5955. ISSN: 1573-7462. DOI: 10.1007/s10462-020-09838-1. URL: <http://dx.doi.org/10.1007/s10462-020-09838-1>.
- [45] Sejun Park, Chulhee Yun, Jaeho Lee, and Jinwoo Shin. “Minimum Width for Universal Approximation”. In: *International Conference on Learning Representations*. 2021. URL: <https://openreview.net/forum?id=0-XJwyolF-k>.
- [46] R.R. Schaller. “Moore’s law: past, present and future”. In: *IEEE Spectrum* 34.6 (1997), pp. 52–59. DOI: 10.1109/6.591665.
- [47] Hugo Touvron, Thibaut Lavril, Gautier Izacard, Xavier Martinet, Marie-Anne Lachaux, et al. *LLaMA: Open and Efficient Foundation Language Models*. 2023. arXiv: 2302.13971 [cs.CL].
- [48] Yu Emma Wang, Gu-Yeon Wei, and David Brooks. *Benchmarking TPU, GPU, and CPU Platforms for Deep Learning*. 2019. arXiv: 1907.10701 [cs.LG].
- [49] David E. Rumelhart, Geoffrey E. Hinton, and Ronald J. Williams. “Learning representations by back-propagating errors”. In: *Nature* 323.6088 (Oct. 1986), pp. 533–536. ISSN: 1476-4687. DOI: 10.1038/323533a0. URL: <http://dx.doi.org/10.1038/323533a0>.
- [50] Diederik P. Kingma and Jimmy Ba. *Adam: A Method for Stochastic Optimization*. 2017. arXiv: 1412.6980 [cs.LG].
- [51] A. Vallenari, A. G. A. Brown, T. Prusti, J. H. J. de Bruijne, F. Arenou, et al. “GaiaData Release 3: Summary of the content and survey properties”. In: *Astronomy and Astrophysics* 674 (June 2023), A1. ISSN: 1432-0746. DOI: 10.1051/0004-6361/202243940. URL: <http://dx.doi.org/10.1051/0004-6361/202243940>.
- [52] Dean Richardson, Robert L. Jenkins III, John Wright, and Larry Maddox. “ABSOLUTE-MAGNITUDE DISTRIBUTIONS OF SUPERNOVAE”. In: *The Astronomical Journal* 147.5 (Apr. 2014), p. 118. ISSN: 1538-3881. DOI: 10.1088/0004-6256/147/5/118. URL: <http://dx.doi.org/10.1088/0004-6256/147/5/118>.
- [53] Romina Ahumada, Carlos Allende Prieto, Andrés Almeida, Friedrich Anders, Scott F. Anderson, et al. “The 16th Data Release of the Sloan Digital Sky Surveys: First Release from the APOGEE-2 Southern Survey and Full Release of eBOSS Spectra”.

- In: *APJS* 249.1, 3 (July 2020), p. 3. DOI: 10.3847/1538-4365/ab929e. arXiv: 1912.02905 [astro-ph.GA].
- [54] Jordi Miralda-Escude. “Reionization of the Intergalactic Medium and the Damping Wing of the Gunn-Peterson Trough”. In: *The Astrophysical Journal* 501.1 (July 1998), pp. 15–22. ISSN: 1538-4357. DOI: 10.1086/305799. URL: <http://dx.doi.org/10.1086/305799>.
- [55] Bradley Greig, Sarah E. I. Bosman, Frederick B. Davies, Dominika Ďurovčíková, Hassan Fathivavsari, et al. *Blind QSO reconstruction challenge: Exploring methods to reconstruct the Ly $\alpha$  emission line of QSOs*. 2024. arXiv: 2404.01556 [astro-ph.CO].
- [56] Sarah E I Bosman, Dominika Ďurovčíková, Frederick B Davies, and Anna-Christina Eilers. “A comparison of quasar emission reconstruction techniques for  $z > 5.0$  Lyman-alpha and Lyman-beta transmission”. In: *Monthly Notices of the Royal Astronomical Society* 503.2 (Feb. 2021), pp. 2077–2096. ISSN: 1365-2966. DOI: 10.1093/mnras/stab572. URL: <http://dx.doi.org/10.1093/mnras/stab572>.
- [57] Bin Liu and Rongmon Bordoloi. “A deep learning approach to quasar continuum prediction”. In: *Monthly Notices of the Royal Astronomical Society* 502.3 (Jan. 2021), pp. 3510–3532. ISSN: 1365-2966. DOI: 10.1093/mnras/stab177. URL: <http://dx.doi.org/10.1093/mnras/stab177>.
- [58] Jonah C. Rose, Paul Torrey, Francisco Villaescusa-Navarro, Mark Vogelsberger, Stephanie O’Neil, Mikhail V. Medvedev, Ryan Low, Rakshak Adhikari, and Daniel Angles-Alcazar. *Inferring Warm Dark Matter Masses with Deep Learning*. 2023. arXiv: 2304.14432 [astro-ph.CO].
- [59] Parth Nayak, Michael Walther, Daniel Gruen, and Sreyas Adiraju. *Ly $\alpha$ NN: A Deep Learning Field-level Inference Machine for the Lyman- $\alpha$  Forest*. 2023. arXiv: 2311.02167 [astro-ph.CO].
- [60] Gareth James, Daniela Witten, Trevor Hastie, and Robert Tibshirani. *An Introduction to Statistical Learning: with Applications in R*. Springer US, 2021. ISBN: 9781071614181. DOI: 10.1007/978-1-0716-1418-1. URL: <http://dx.doi.org/10.1007/978-1-0716-1418-1>.
- [61] Shaeke Salman and Xiuwen Liu. *Overfitting Mechanism and Avoidance in Deep Neural Networks*. 2019. arXiv: 1901.06566 [cs.LG].

## Bibliography

---

- [62] V. Roshan Joseph and Akhil Vakayil. “SPLit: An Optimal Method for Data Splitting”. In: *Technometrics* 64.2 (June 2021), pp. 166–176. ISSN: 1537-2723. DOI: 10.1080/00401706.2021.1921037. URL: <http://dx.doi.org/10.1080/00401706.2021.1921037>.
- [63] Michael W Browne. “Cross-Validation Methods”. In: *Journal of Mathematical Psychology* 44.1 (Mar. 2000), pp. 108–132. ISSN: 0022-2496. DOI: 10.1006/jmps.1999.1279. URL: <http://dx.doi.org/10.1006/jmps.1999.1279>.
- [64] Connor Shorten and Taghi M. Khoshgoftaar. “A survey on Image Data Augmentation for Deep Learning”. In: *Journal of Big Data* 6.1 (July 2019). ISSN: 2196-1115. DOI: 10.1186/s40537-019-0197-0. URL: <http://dx.doi.org/10.1186/s40537-019-0197-0>.
- [65] Kaiming He, Xiangyu Zhang, Shaoqing Ren, and Jian Sun. *Deep Residual Learning for Image Recognition*. 2015. arXiv: 1512.03385 [cs.CV].
- [66] Sergey Ioffe and Christian Szegedy. *Batch Normalization: Accelerating Deep Network Training by Reducing Internal Covariate Shift*. 2015. arXiv: 1502.03167 [cs.LG].
- [67] Udo von Toussaint. “Bayesian inference in physics”. In: *Rev. Mod. Phys.* 83 (3 2011), pp. 943–999. DOI: 10.1103/RevModPhys.83.943. URL: <https://link.aps.org/doi/10.1103/RevModPhys.83.943>.
- [68] Laurent Valentin Jospin, Hamid Laga, Farid Boussaid, Wray Buntine, and Mohammed Bennamoun. “Hands-On Bayesian Neural Networks—A Tutorial for Deep Learning Users”. In: *IEEE Computational Intelligence Magazine* 17.2 (May 2022), pp. 29–48. ISSN: 1556-6048. DOI: 10.1109/mci.2022.3155327. URL: <http://dx.doi.org/10.1109/MCI.2022.3155327>.
- [69] Thomas G. Dietterich. “Ensemble Methods in Machine Learning”. In: *Lecture Notes in Computer Science*. Springer Berlin Heidelberg, 2000, pp. 1–15. ISBN: 9783540450146. DOI: 10.1007/3-540-45014-9\_1. URL: [http://dx.doi.org/10.1007/3-540-45014-9\\_1](http://dx.doi.org/10.1007/3-540-45014-9_1).
- [70] Takuya Akiba, Shotaro Sano, Toshihiko Yanase, Takeru Ohta, and Masanori Koyama. “Optuna: A Next-generation Hyperparameter Optimization Framework”. In: *Proceedings of the 25th ACM SIGKDD International Conference on Knowledge Discovery and Data Mining*. 2019.

- 
- [71] James Bergstra, Rémi Bardenet, Yoshua Bengio, and Balázs Kégl. “Algorithms for hyper-parameter optimization”. In: *Proceedings of the 24th International Conference on Neural Information Processing Systems*. NIPS’11. Granada, Spain: Curran Associates Inc., 2011, pp. 2546–2554. ISBN: 9781618395993.
  - [72] Sandro D’Odorico, Stefano Cristiani, Hans Dekker, Vanessa Hill, Andreas Kaufer, Taesun Kim, and Francesca Primas. “Performance of UVES, the echelle spectrograph for the ESO VLT and highlights of the first observations of stars and quasars”. In: *Discoveries and Research Prospects from 8- to 10-Meter-Class Telescopes*. Ed. by Jacqueline Bergeron. Vol. 4005. Society of Photo-Optical Instrumentation Engineers (SPIE) Conference Series. June 2000, pp. 121–130. DOI: 10.1117/12.390133.
  - [73] Prakash Gaikwad, Raghunathan Srianand, Martin G Haehnelt, and Tirthankar Roy Choudhury. “A consistent and robust measurement of the thermal state of the IGM at  $2 < z < 4$  from a large sample of Ly-alpha forest spectra: evidence for late and rapid HeIIreionization”. In: *Monthly Notices of the Royal Astronomical Society* 506.3 (July 2021), pp. 4389–4412. ISSN: 1365-2966. DOI: 10.1093/mnras/stab2017. URL: <http://dx.doi.org/10.1093/mnras/stab2017>.
  - [74] Molly Wolfson, Joseph F. Hennawi, Frederick B. Davies, Zarija Lukić, and Jose Oñorbe. *Forecasting constraints on the high-z IGM thermal state from the Lyman- $\alpha$  forest flux auto-correlation function*. 2023. arXiv: 2309.05647 [astro-ph.CO]. URL: <https://arxiv.org/abs/2309.05647>.
  - [75] Jens-Peter Kreiss and Efstathios Paparoditis. “Bootstrap methods for dependent data: A review”. In: *Journal of the Korean Statistical Society* 40.4 (Dec. 2011), pp. 357–378. ISSN: 1226-3192. DOI: 10.1016/j.jkss.2011.08.009. URL: <http://dx.doi.org/10.1016/j.jkss.2011.08.009>.
  - [76] Ravid Shwartz-Ziv and Naftali Tishby. *Opening the Black Box of Deep Neural Networks via Information*. 2017. arXiv: 1703.00810 [cs.LG].
  - [77] Vanessa Buhrmester, David Münch, and Michael Arens. *Analysis of Explainers of Black Box Deep Neural Networks for Computer Vision: A Survey*. 2019. arXiv: 1911.12116 [cs.AI].
  - [78] Jonas Fischer, Anna Olah, and Jilles Vreeken. “What’s in the Box? Exploring the Inner Life of Neural Networks with Robust Rules”. In: *Proceedings of the 38th International Conference on Machine Learning*. Ed. by Marina Meila and

- Tong Zhang. Vol. 139. Proceedings of Machine Learning Research. PMLR, 2021, pp. 3352–3362. URL: <https://proceedings.mlr.press/v139/fischer21b.html>.
- [79] Intekhab Hossain, Jonas Fischer, Rebekka Burkholz, and John Quackenbush. *Not all tickets are equal and we know it: Guiding pruning with domain-specific knowledge*. 2024. arXiv: 2403.04805 [cs.LG]. URL: <https://arxiv.org/abs/2403.04805>.
- [80] George D. Becker, James S. Bolton, Martin G. Haehnelt, and Wallace L. W. Sargent. “Detection of extended HeII reionization in the temperature evolution of the intergalactic medium: IGM temperatures over  $2 < z < 5$ ”. In: *Monthly Notices of the Royal Astronomical Society* 410.2 (Nov. 2010), pp. 1096–1112. ISSN: 0035-8711. DOI: 10.1111/j.1365-2966.2010.17507.x. URL: <http://dx.doi.org/10.1111/j.1365-2966.2010.17507.x>.
- [81] William H. Press, Brian P Flannery, Saul A Teukolsky, and William T Vetterling. *Numerical Recipes in C book set: Numerical Recipes in C: The Art of Scientific Computing*. 2nd ed. Cambridge, England: Cambridge University Press, Oct. 1992.
- [82] Michael T Murphy, Glenn G Kacprzak, Giulia A D Savorgnan, and Robert F Carswell. “The UVES Spectral Quasar Absorption Database (SQUAD) data release 1: the first 10 million seconds”. In: *Monthly Notices of the Royal Astronomical Society* 482.3 (Oct. 2018), pp. 3458–3479. ISSN: 1365-2966. DOI: 10.1093/mnras/sty2834. URL: <http://dx.doi.org/10.1093/mnras/sty2834>.
- [83] Ann S. Almgren, John B. Bell, Mike J. Lijewski, Zarija Lukić, and Ethan Van Andel. “Nyx: A MASSIVELY PARALLEL AMR CODE FOR COMPUTATIONAL COSMOLOGY”. In: *The Astrophysical Journal* 765.1 (Feb. 2013), p. 39. ISSN: 1538-4357. DOI: 10.1088/0004-637X/765/1/39. URL: <http://dx.doi.org/10.1088/0004-637X/765/1/39>.
- [84] Feige Wang, Xue-Bing Wu, Xiaohui Fan, Jinyi Yang, Zheng Cai, et al. “AN ULTRA-LUMINOUS QUASAR AT  $z = 5.363$  WITH A TEN BILLION SOLAR MASS BLACK HOLE”. In: *The Astrophysical Journal* 807.1 (June 2015), p. L9. ISSN: 2041-8213. DOI: 10.1088/2041-8205/807/1/19. URL: <http://dx.doi.org/10.1088/2041-8205/807/1/L9>.
- [85] Tom Charnock, Guilhem Lavau, and Benjamin D. Wandelt. “Automatic physical inference with information maximizing neural networks”. In: *Physical Review D* 97.8 (Apr. 2018). ISSN: 2470-0029. DOI: 10.1103/physrevd.97.083004. URL: <http://dx.doi.org/10.1103/PhysRevD.97.083004>.

- [86] Alexander Ly, Maarten Marsman, Josine Verhagen, Raoul Grasman, and Eric-Jan Wagenmakers. *A Tutorial on Fisher Information*. 2017. arXiv: 1705.01064 [math.ST]. URL: <https://arxiv.org/abs/1705.01064>.
- [87] Soumik Maitra, Stefano Cristiani, Matteo Viel, Roberto Trotta, and Guido Capani. *Parameter estimation from Ly $\alpha$  forest in Fourier space using Information Maximising Neural Network*. 2024. arXiv: 2404.04327 [astro-ph.CO]. URL: <https://arxiv.org/abs/2404.04327>.
- [88] Clara Grazian and Yanan Fan. *A review of Approximate Bayesian Computation methods via density estimation: inference for simulator-models*. 2019. arXiv: 1909.02736 [stat.CO]. URL: <https://arxiv.org/abs/1909.02736>.